

# **Luminescence studies of strontium sulphide based phosphors for display applications**

Thesis submitted to  
**COCHIN UNIVERSITY OF SCIENCE AND TECHNOLOGY**  
in partial fulfillment of the requirements  
for the award of the degree of  
**DOCTOR OF PHILOSOPHY**

**Anila E.I**

**Department of Physics  
Cochin University of Science and Technology  
Cochin – 682 022, Kerala, India**

**March 2008**

Luminescence studies of strontium sulphide based phosphors for display applications

*Ph.D thesis in the field of material science*

*Author:*

Anila.E.I  
Optoelectronic Devices Laboratory  
Department of Physics  
Cochin University of Science and Technology  
Cochin – 682 022, Kerala, India  
email: anila\_ei@yahoo.com

*Supervisor:*

Dr. M.K. Jayaraj  
Reader  
Optoelectronics Device Laboratory  
Department of Physics  
Cochin University of Science and Technology  
Cochin – 682 022, Kerala, India  
email: mkj@cusat.ac.in

March 2008

**Dr. M.K. Jayaraj**

Reader

Department of Physics

Cochin University of Science and Technology

Cochin – 682 022

---

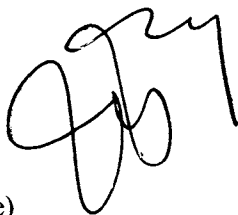
12<sup>th</sup> March 2008

## Certificate

Certified that the work presented in this thesis entitled “*Luminescence studies of strontium sulphide based phosphors for display applications*” is based on the authentic record of research done by Ms. Anila.E.I under my guidance in the Department of Physics, Cochin University of Science and Technology, Cochin – 682 022 and has not been included in any other thesis submitted for the award of any degree.

Dr. M.K. Jayaraj

(Supervising Guide)



---

Phone : +91 484 2577404 extn 33 Fax: 91 484 2577595 email: [mkj@cusat.ac.in](mailto:mkj@cusat.ac.in)

## Declaration

Certified that the work presented in this thesis entitled “*Luminescence studies of strontium sulphide based phosphors for display applications*” is based on the original research work done by me under the supervision and guidance of Dr. M.K. Jayaraj, Reader, Department of Physics, Cochin University of Science and Technology, Cochin-682022 and has not been included in any other thesis submitted previously for the award of any degree.

Cochin – 22  
12<sup>th</sup> March 2008

A handwritten signature in black ink, appearing to read 'Anila.E.I.', with a horizontal line underneath.

Anila.E.I

## **Acknowledgements**

*The accomplishment of this research work was made possible by a number of individuals who had either already observed certain facts in this field or been progressing in different paths towards their goals.*

*For an experimental research work of this stature demanding modern infrastructure and supportive intervention, the academic nurturing bestowed by Dr. M K Jayaraj is highly praiseworthy and it was his expertise and knowledge that led me to move boldly towards this goal. I take this opportunity to extend my sincere gratitude to him for his patience and constructive support.*

*I would like to express my sincere thanks to the Head Prof. Godfrey Louis and the former Heads of the Department of Physics who played pivotal roles in the initiation and progress of this project. I owe very much to Dr. K. P. Vijayakumar, Dr. Sudha Kartha and Mr. Jayakrishnam for their timely support. I am very much thankful to Dr. S Jayalekshmy and her research team for providing their facilities in the laboratory to develop my work. I greatly acknowledge the help and guidance of all the faculty members of the Department of Physics. \_*

*I am thankful to all the office, library and technical staff of the Department of Physics for their help and cooperation.*

*For extending a helping hand at the beginning as well as through out my work the role played by Mr. Anoop was tremendous and deserves my sincere thanks.*

*I am extremely grateful to Mr. Sanjay and Mr. Arun for their timely support.*

*I must thank the former group members, Mr. Aldrin Antony, Mr. Manoj, Ms. Nisha M and Ms. Asha A S for sparing their valuable expertise and time in developing this thesis. I must extend significant gratitude to Mr. N V Joshy, Ms. Vanaja, Mr. Ajimsha, Mr. Saji, Ms. Reshmi, Ms. Mini, Ms. Rehana, Mr. Aneesh, Mr. Ratheesh, Ms Sreeja, Ms. Ragitha and Mr. Krishnaprasad Mr. James for their academic and emotional support through out the work.*

*I should state my thanks to Arun V and Subha for their supportive gestures in this effort.*

*This would be the right moment to recollect the encouragement given by Dr. Manzoor.*

*I remember with cheer and pleasure, my association with Mr.Prince, Ms.Vinitha, Mr.Sasankan and Mr.Sajeev during my research period in CUSAT.*

*This work was made possible by the timely decision and support by my parent institution UC College, Aluva and by the faculty improvement programme of UGC. I thankfully record my indebtedness to these bodies.*

*I am very much touched by the selfless support, motivation and encouragement given by my teachers and colleagues in the Department of Physics, U C College, Aluva for the smooth advancement of this work.*

*I would like to record my love and affection to my parents, dear husband and sweet sons who are my strength in all my endeavors.*

*I feel highly blessed by the Almighty in making my dream come true.*

*Anila.E.I*

-

# CONTENTS

## Preface

## CHAPTER ONE

### Literature Review

1.1 Luminescence Process	1
1.2 Photoluminescence	2
1.2.1 Intrinsic luminescence	2
a) Band - to - band luminescence	3
b) Exciton luminescence	3
c) Cross luminescence	3
1.2.2 Extrinsic luminescence	4
a) Unlocalised type	4
b) Localised type	5
1.3 Electroluminescence	6
1.4 ACTFEL device structure	8
1.5 ACTFEL operation	11
1.6 ACTFEL materials	17
1.6.1 The phosphor layer	17
1.6.2 Insulators	22
1.6.3 Transparent contacts	24
1.6.4 Opaque contacts	25
1.6.5 Substrates	26
1.7 Properties of ACTFEL phosphor host materials	27
1.7.1 Band structure	27
1.7.2 Dielectric permittivity	28
1.7.3 Melting temperature	29
1.7.4 Ionicity	31
1.7.5 Thermodynamic stability	33
1.7.6 Moisture sensitivity	33



1.8 Activators	34
1.8.1 Ionic radius	34
1.8.2 Valency	35
1.9 Stokes shift	35
1.10 Coactivators	36
1.11 Killer centers	38
1.12 Sulphide phosphors	39
1.13 References	42

## **CHAPTER TWO**

### **Experimental techniques and characterisation tools**

2.1 Introduction	47
2.2 Thin film deposition techniques	47
2.2.1 Thermal evaporation by resistive heating	48
2.2.2 Electron beam evaporation method	49
2.3 Characterisation tools	55
2.3.1 Thin film thickness	55
2.3.2 X-ray diffraction studies	56
2.3.3 Atomic Force microscopy (AFM)	58
2.3.4 Transmission spectroscopy	59
2.3.5 Diffuse reflectance spectroscopy	61
2.3.6 Photoluminescence measurements	62
2.3.7 CIE colour coordinates	64
2.3.8 Thermogravimetric analysis (TGA)	68
2.3.9 Inductively coupled plasma- Atomic emission spectroscopy (ICP-AES)	69
2.3.10 Electron paramagnetic resonance spectroscopy (EPR)	70
2.3.11 Transmission electron microscopy (TEM)	73
2.3.12 Resistivity by two probe method	75
2.3.13 Luminance- Voltage characterisation	75
2.4 References	81

## **CHAPTER THREE**

### **Colour control in SrS:Cu,Cl powder phosphor**

3.1 Abstract	83
3.2 Introduction	83

3.3 Experimental	84
3.4 Results and discussion	85
3.5 Conclusion	95
3.6 References	97

## **CHAPTER FOUR**

### **Effect of NH<sub>4</sub>Cl flux on the structural and luminescence properties of SrS:Cu,F phosphor**

4.1 Abstract	99
4.2 Introduction	99
4.3 Experimental	100
4.4 Results and discussion	101
4.5 Conclusion	104
4.6 References	105

## **CHAPTER FIVE**

### **Luminescence properties of SrS:Dy,Cl phosphor**

5.1 Abstract	107
5.2 Introduction	108
5.3 Experimental	109
5.4 Results and discussion	109
5.4.1 EPR measurements	109
5.4.2 Photoluminescence spectra	111
5.4.3 Yellow to blue intensity ratio	113
5.4.4 Photoluminescence excitation spectra	115
5.4.5 Diffuse reflectance and conductivity Measurements	117
5.5 Conclusion	119
5.6 References	121

## **CHAPTER SIX**

### **Sensitised luminescence of SrS:Dy,Cu,Cl phosphor**

6.1 Abstract	123
6.2 Introduction	123

6.3 Experimental	124
6.4 Results and discussion	125
6.5 Conclusion	133
6.6 References	134

## **CHAPTER SEVEN**

### **Low temperature fabrication of SrS:Cu,F ACTFEL device by electron beam evaporation**

7.1 Abstract	135
7.2 Introduction	135
7.3 Experimental	136
7.4 Results and discussion	137
7.5 Conclusion	147
7.6 References	148

## **CHAPTER EIGHT**

### **PART A**

#### **Introduction to nanotechnologies and nanomaterials**

8.1 Introduction	151
8.2 Exciton Bohr radius	154
8.3 Quantum confinement	154
8.4 Nanophosphors	158

### **PART B**

#### **Synthesis and characterization of SrS:Cu nanophosphor**

8.5 Abstract	159
8.6 Introduction	159
8.7 Experimental	160
8.8 Results and discussion	162
8.8.1 SrS:Cu nano and bulk phosphor	162
8.8.2 Effect of firing temperature on the properties of SrS:Cu nanophosphor	169
8.9 Conclusion	173
8.10 References	174

## **CHAPTER NINE**

**Summary**

177

**References**

179

# Preface

Cathode-ray tube (CRT) technology, has dominated the display industry in the past decades because of their excellent chromaticity, contrast, and resolution at an affordable price. It has some intrinsic drawbacks making it unsuitable for many new applications. In spite of the flat nature of the two dimensional image, CRTs are inherently bulky devices since it is difficult to achieve a wide electron deflection angle. The wide electron deflection angle, however makes it difficult to achieve flatness of the CRT screen without significant distortion of the image. Large energy consumption, fragile nature, flickering of the screen and emission of electromagnetic radiation are other drawbacks of CRT. There has been intense drive towards portability for many display-utilizing products necessitating displays that are physically smaller, more rugged and less power-hungry than CRT.

Most of the research involving non-CRT display technologies is focused upon developing a thin display, known as the flat panel display (FPD), that has the quality of a CRT display, but is rugged and much less power hungry than a CRT display of comparable viewing area. The front-runner in this effort is the liquid-crystal-display (LCD) which is found in virtually every laptop computer manufactured today. Other less well known display technologies showing promise are the plasma display panel (PDP), the field-emission display (FED), and the thin film electroluminescent (TFEL) display. All these FPD technologies possess unique properties which are desirable for some applications, but unsuitable for others. The ability to manufacture 12-20 inch full-colour liquid crystal displays has led to the domination of LCDs in the portable computer market. High luminance, high contrast, and a modest resolution make plasma display panels (PDP) most

suitable for large area information screens and high-definition television applications. Due to the mature cathodoluminescent technology, field emission displays are expected to replace CRTs in the near future. High spatial resolution, which is very difficult to achieve with other technologies, makes electroluminescent (EL) displays an attractive choice for medical or industrial instruments, military equipment, and virtual reality systems, where compactness is vital. Other advantages of EL displays are their emissive nature resulting in wide viewing angle, high luminance and high contrast. The central focus of the thesis is the luminescent studies of strontium sulphide based powder, thin film and nano phosphors for display applications. An SrS:Cu,F ACTFEL device was also fabricated. The thesis consists of nine chapters.

*Chapter 1* is the review of the pertinent literature covering the basics of EL phosphors and ACTFEL device operation. It includes an introduction to luminescence, properties of luminescent materials, operation of ACTFEL device, brief description and a short review of the materials studied in the present investigation.

*Chapter 2* describes the experimental techniques for preparation and characterization of the samples, applied in this research. Bulk phosphors were prepared by solid state reaction, thin film samples by EB/thermal evaporation and the nanophosphor was prepared by chemical method. A brief description of electron beam evaporation is included in this chapter. The phosphor samples were characterized by various analytical techniques. They include thickness measurement of deposited films by Veeco Stylus profilometer, diffuse reflectance and transmission measurements of powder and film samples by Jasco-V-570 uv-vis-nir spectrophotometer, studies of crystallographic properties of powder and film samples by x-ray diffraction

and transmission electron microscopy, photoluminescence measurements by Jobin Yvon Fluoromax-3 Fluorimeter, Electron paramagnetic resonance studies by Varian E-112 E-line Century series X-band EPR spectrometer, Surface analysis by atomic force microscopy etc .

*Chapter 3* includes structural and optical characterization of SrS:Cu,Cl powder phosphor. By varying the Cu concentration in the sample, emission colour can be tailored from blue to green. Red shift in PL excitation peak at 315nm was observed with increasing doping concentration. The lattice parameter decreases at lower concentrations and increases at high concentrations depending upon whether Cu<sup>+</sup> ion is in the substitutional site (along with another Cu<sup>+</sup> ion in lattice site) or off-centered site. Decrease in band gap was observed with doping concentration which is due to band tailing effect.

*Chapter 4* investigates the influence of NH<sub>4</sub>Cl on the optical and structural properties of SrS:Cu,F powder phosphor. NH<sub>4</sub>Cl acted as a flux by achieving crystallinity of the phosphor at low temperature, enhancing the luminescence. Red shift in absorption peak of host lattice was observed which may be due to band tailing effect. Both PL and PLE intensities enhanced to six times due to the addition of flux .Red shift in photoluminescence emission may be due to more efficient incorporation of Cu<sup>+</sup> ions to Sr<sup>2+</sup> site.

*Chapter 5* presents the optical and electrical characterization of SrS:Dy,Cl powder phosphor. EPR spectrum consisted of signals of Dy<sup>3+</sup> and F<sup>+</sup> centre. Blue shift of the band gap energy and red shift of the PLE spectrum were observed with increasing doping concentration which are due to Burstein Moss effect and band tailing effect respectively. Yellow to blue intensity

ratio of  $\text{Dy}^{3+}$  emission varied with doping concentration since it is nonisovalent with  $\text{Sr}^{2+}$ .

**Chapter 6** investigates the structural and optical properties of  $\text{SrS: Dy,Cu,Cl}$  two component phosphor. Resonance radiationless mechanism of energy transfer from  $\text{Cu}^+$  to  $\text{Dy}^{3+}$  was observed. A model is proposed demonstrating the sensitizing behaviour of  $\text{Cu}^+$  ion in  $\text{SrS:Dy,Cu,Cl}$  phosphor. Energy is transferred from  $^3\text{E}_g$  of  $\text{Cu}^+$  to  $^4\text{F}_{9/2}$  of  $\text{Dy}^{3+}$ . Resultant emission colour from the samples vary with the variation in doping concentration of Cu.

**Chapter 7** deals with low temperature deposition of  $\text{SrS:Cu,F}$  thin film by concomitant evaporation of host and dopant by electron beam evaporation and thermal evaporatin methods. Deposition was done on glass substrate without post annealing and sulphur coevaporation. From the AFM images, the samples were observed to contain a continuous network of flat areas with a root mean square (rms) surface roughness  $< 10\text{nm}$ , having heights exceeding  $100\text{nm}$  in many places. Green emission at  $535\text{nm}$  was observed at an excitation wavelength of  $320\text{nm}$ .  $\text{SrS:Cu,F}$  ACTFEL device was also fabricated with ZnS as buffer layer. Device PL consisted of two peaks at  $380\text{nm}$  and  $434\text{nm}$  whereas EL consisted of an additional peak at  $535\text{nm}$ .

**Chapter 8** consists of two parts. Part one gives Introduction to nanotechnology, followed by description of basic nanostructures such as quantum dot, nano rod and quantum well. Part two describes the synthesis of  $\text{SrS:Cu}$  nano particles ( $7\text{nm}$ ) by wet chemical method; and it's structural and optical characterizations. Variation in band gap, intensity and line width of photoluminescence emission and excitation of the samples were found to be in agreement with size effects. Finally **chapter 9** provides conclusions and scope for future work.



## Papers presented in National/International conferences

1. Effect of Post-annealing on structural and photoluminescence properties of SrS:Dy,Cl Thin Film, **E I Anila**, M K Jayaraj, *Proc. of ASID conference, Delhi, India, 2005*
2. Red Shift in the photoluminescence emission of SrS:Cu,Cl phosphor, **E.I Anila**, G Anoop, K. Minikrishna, I.P Sanjaykumar and M.K Jayaraj, *Proc. of the Eight International Conference on Optoelectronics, FiberOptics and, Photonics, Hyderabad, India, 2006*
3. Preparation and characterization of SrS:Cu,Cl nanophosphor, **E.I.Anila**, Arun.Aravind and M.K.Jayaraj, *Proc. of the international conference on Materials For the Millennium, Kochi, India, 2007*
4. Synthesis and optical characterisation of Copper doped SrS nanophosphor, **E.I.Anila**, Arun.Aravind and M.K.Jayaraj, *National conference on smart electroceramics, Thrissur, India, 2007*
5. Copper doped strontium sulphide nanoparticles for display applications, Arun Aravind, **E.I.Anila** and M.K.Jayaraj, *Third Marie Curie Summer School on "Partial Melt and Amorphous Solids, Estremoz, Portugal, 2007*

## Journal papers

1. Photoluminescence of SrS:Cu nanophosphor, **E.I.Anila**, Arun Aravind and M.K.Jayaraj, *Nanotechnology* **19** (2008)145604

2. Dysprosium concentration dependence on the optical properties of SrS:Dy,Cl phosphor, **E.I.Anila** and M.K.Jayaraj, Materials Research Bulletin (communicated)
3. Colour control in SrS: Cu, Cl powder phosphor, **E.I.Anila**, I.P. Sanjaykumar and M.K.Jayaraj, Journal of Alloys and Compounds (communicated)
4. Low temperature deposition of SrS:Cu,F ACTFEL device by electron beam evaporation, **E.I. Anila** and M.K. Jayaraj, Journal of physicsD: Applied physics (communicated)
5. Sensitized luminescence from SrS:Dy,Cu,Cl phosphor, **E.I.Anila** and M.K.Jayaraj (to be communicated)

# CHAPTER ONE

## Literature Review

A review of currently available literature pertaining to ACTFEL materials and devices is presented in this chapter. The structure and operation of an ACTFEL device is discussed. Material issues in ACTFEL fabrication are also considered.

### 1.1 Luminescence Process

The luminescence process is commonly considered in terms of configuration coordinate diagram. Two potential wells are plotted with energy ( $E$ ) on the ordinate and interatomic distance ( $R$ ) on the abscissa. The lower and upper parabolas represent the ground and excited states respectively of the luminescent center (Figure 1.1).

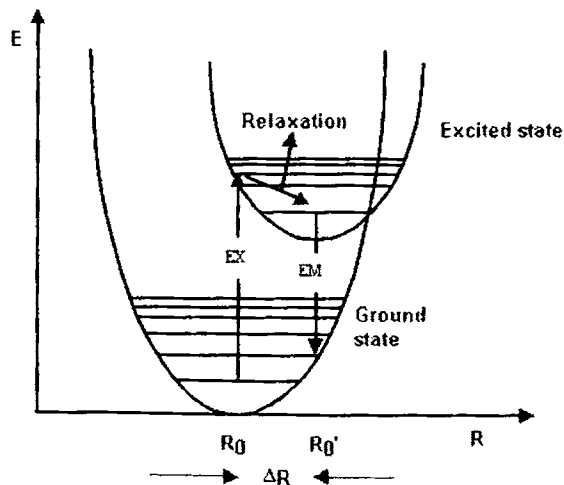


Figure 1.1. Configuration coordinate diagram illustrating luminescence process

A photon is absorbed by the luminescent center, giving rise to an electronic transition from the lowest vibrational level of the ground state to a higher vibrational level of the excited state (EX). The excited state, being unstable, the electron relaxes giving away the excess energy to the surroundings. Because of the redistribution of electron density in the excited state, configuration coordinate changes by  $\Delta R$ ; this process being called the relaxation. The system can return to a high vibrational level of the ground state by the emission of radiation (EM) and here also relaxation occurs to the lowest vibrational level. Because of this process, the emission occurs at a lower energy than that of absorption. If the temperature is high or  $\Delta R$  is large, the electron can return to ground state through the crossing point of the two parabolas. At this point; an electron is in the excited vibrational level of the ground state and subsequently decay non radiatively to the ground vibrational level.

## **1.2 Photoluminescence**

Luminescence in solids is the phenomenon in which electronic states of solids are excited by some energy from an external source and on deexcitation, energy is released as light. When energy comes from short-wavelength light, usually UV, the phenomenon is called photoluminescence (PL) [1]. PL is divided into two major types: Intrinsic and extrinsic depending on the nature of electronic transition producing it.

### **1.2.1 Intrinsic luminescence:**

There are three kinds of intrinsic luminescence: 1) band-to-band luminescence 2) exciton luminescence 3) cross-luminescence.

### **a) Band –to –band luminescence:**

Luminescence owing to the band-to-band transition, ie to the recombination of an electron in the conduction band with a hole in the valence band, can be seen in pure crystal at relatively high temperature. This has been observed in Si,Ge and IIIb-Vb compounds such as GaAs.

### **b) Exciton luminescence:**

An exciton is a composite particle of an excited electron and a hole interacting with one another. It moves in a crystal conveying energy and produces luminescence owing to the recombination of the electron and the hole. There are two kinds of excitons: Wannier exciton and Frenkel exciton.

The Wannier exciton model express an exciton composed of an electron in the conduction band and a hole in the valence band bound together by coulomb interaction. The expanse of the wavefunction of the electron and hole in Wannier exciton is much larger than the lattice constant. The excitons in IIIb-Vb and IIb-VIb compounds are examples for Wannier exciton. The Frenkel exciton model is used in cases where expanse of electron and hole wave function is smaller than lattice constant. The excitons in organic molecular crystals are examples of Frenkel exciton.

### **c) Cross luminescence**

Cross luminescence is produced by the recombination of an electron in the valence band with a hole created in the outer most core band. This is observed in number of alkali and alkaline-earth halides and double halides.

This takes place only when the energy difference between the top of valence band and that of conduction band is smaller than the bandgap energy. This type of luminescence was first observed in  $\text{BaF}_2$ .

### **1.2.2 Extrinsic luminescence:**

Luminescence caused by intentionally incorporated impurities, mostly metallic impurities or defects is classified as extrinsic luminescence. Most of the observed type of luminescence of practical application belongs to this category. Intentionally incorporated impurities are activators and materials made luminescent in this way are called phosphors.

Extrinsic luminescence in ionic crystals and semiconductors is classified into two types: unlocalized and localized. In the unlocalized type, the electrons and holes of the host lattice participate in the luminescence process, while in localized type the luminescence excitation and emission process are confined in a localized luminescence center.

#### **a) Unlocalised type:**

In semiconductors donors and accepters act as luminescence activators. There are two types of luminescence transitions i.e. the transition of a free carrier to a bound carrier and the transition of a bound electron at a donor to a bound hole at an acceptor. These kinds of luminescence lines and bands are usually observed in compound semiconductors such as IIIb-Vb and IIb-VIb compounds.

## b) Localised type:

Various kinds of metallic impurities intentionally incorporated in ionic crystals and semiconductors create efficient localized luminescence centers. Localized type centers are classified into: 1) allowed transition type b) forbidden transition type in terms of electric dipole transitions.

The electric dipole transition can take place between energy levels with different parities. The selection rule for this transition in atoms is  $\Delta l = \pm 1$ . When atoms and ions are incorporated in crystals, the forbidden character of the dipole transition is altered by the perturbation of the crystal electric field, so that the forbidden transition becomes allowed to some degree.

Many phosphors that are important from a practical viewpoint are synthesized by incorporating following activators.

a) Allowed transition type:

(i)  $s \leftrightarrow p$  transition –F center  $\leftrightarrow$  ( an electron trapped at an anion vacancy)

(ii)  $s^2 \leftrightarrow sp$  transition  $Tl^+$ ,  $Sn^{2+}$ ,  $Pb^{2+}$ ,  $Sb^{3+}$ ,  $Bi^{3+}$

(iii)  $f \leftrightarrow d$  transition  $Eu^{2+}$ ,  $Ce^{3+}$

b) Forbidden transition type:

(i)  $d \leftrightarrow d$  transition  $Ti^{3+}$ ,  $Cr^{3+}$ ,  $Cr^{2+}$ ,  $Mn^{4+}$ ,  $Mn^{2+}$

(ii)  $f \leftrightarrow f$  transition -  $Pr^{3+}$ ,  $Nd^{3+}$ ,  $Sm^{3+}$ ,  $Eu^{3+}$ ,  $Tb^{3+}$ , T (and other trivalent rare earth ions)

Iron group ions show luminescence owing to the  $3d^n \leftrightarrow 3d^n$  ( $n=2-8$ ) transition in the visible to infrared region. Among them,  $Cr^{3+}$  and  $Mn^{4+}$  ions with the  $3d^3$  configuration and the  $Mn^{2+}$  ion with the  $3d^5$  configuration are

important for phosphor application. The luminescence spectra of  $Mn^{2+}$  are always bands, which vary over a wide visible range from blue to red [1].

### 1.3 Electroluminescence

Electroluminescence is the non-thermal generation of light resulting from the application of an electric field to a substance. Electroluminescence (EL) was first demonstrated by Destriau in 1936, [2] using copper doped zinc sulfide crystals dispersed in castor oil which produce light under an ac field. The applied voltage in Destriau cell was as high as 15 kV but the luminance was extremely poor. The early stage of EL development during the 50s and 60s was mainly concentrated on dc and ac powder cells. It ended without much success, however, owing to the poor performance and reliability of the devices. The situation of today's powder EL has not changed much though improvements have been made in efficiency and stability. A few applications based on powder EL, such as backlight for liquid crystal displays (LCD), have proved attractive.

The advent of thin film electroluminescence (TFEL) was marked by a paper by Inoguchi et al. in 1974 [3], reporting a TFEL device of ZnS:Mn sandwiched between two insulators which showed surprisingly high luminance and extremely long operating life under an ac electric field. During the past 25 years, ACTFEL technology has progressed from the commercialization of monochromic flat panel displays in the early 80s to the development of multi-color and full-color displays in the 90s. Current TFEL displays provide high brightness and contrast, wide viewing angle, fast response time, ruggedness to shock and vibration, wide temperature range,



and long operating life. These features meet the requirements for demanding applications such as industrial process control and instrumentation, medical equipment, civil and military avionics, and transportation. The rapid progress has turned the fiction of "*light source of the future*" into reality.

Ac drive	Ac thin film	<ul style="list-style-type: none"> <li>• High resolution, matrix drive</li> <li>• Long lifetime</li> <li>• Multicolor and full color capabilities.</li> </ul>
	Ac powder	<ul style="list-style-type: none"> <li>• Backlight for LCD</li> <li>• High luminous efficiency</li> <li>• Short lifetime.</li> </ul>
Dc drive	Dc thin film	<ul style="list-style-type: none"> <li>• Reliability problem</li> </ul>
	Dc powder	<ul style="list-style-type: none"> <li>• Low voltage matrix drive</li> <li>• Multicolor capability.</li> </ul>

Table1.1 Characteristics of four types of EL devices

Lack of true full-color TFEL materials, nevertheless, has prevented EL displays from penetrating further into an already highly competitive display market. There are two classes of electroluminescent devices, one due to recombination of electrons and holes called the injection EL and other due to impact excitation called high field EL. Based on impact excitation or high field electroluminescent phenomenon, four types of EL devices have been developed [4]. Their main characteristics are given in table1.1.

## 1.4 ACTFEL device Structure

An ACTFEL device consists of several constituent thin-film layers that are all important in terms of device operation. All ACTFEL devices consist of a phosphor layer, at least one insulating layer, an opaque conductor, a transparent conductor, and a substrate. However there are three different general structures comprising the aforementioned layers commonly employed for fabricating ACTFEL devices.

The first structure, the “standard structure” consists of a phosphor layer encapsulated by two insulating layers, with contact to the top insulator made by an opaque conductor and to the bottom insulator by a transparent conductor. The standard structure for ACTFEL device fabrication is deposited onto a transparent substrate and light reaches the viewer through the substrate as shown in figure 1.2(a). The second structure, the “inverted structure” also consists of a phosphor layer encapsulated by two insulating layers, but contact is made to the top insulator by a transparent electrode and to the bottom insulator by an opaque electrode. The inverted structure for ACTFEL device fabrication can be deposited onto either a transparent substrate or an opaque substrate, because the light reaches the viewer through the transparent top electrode, as shown in figure 1.2(b).

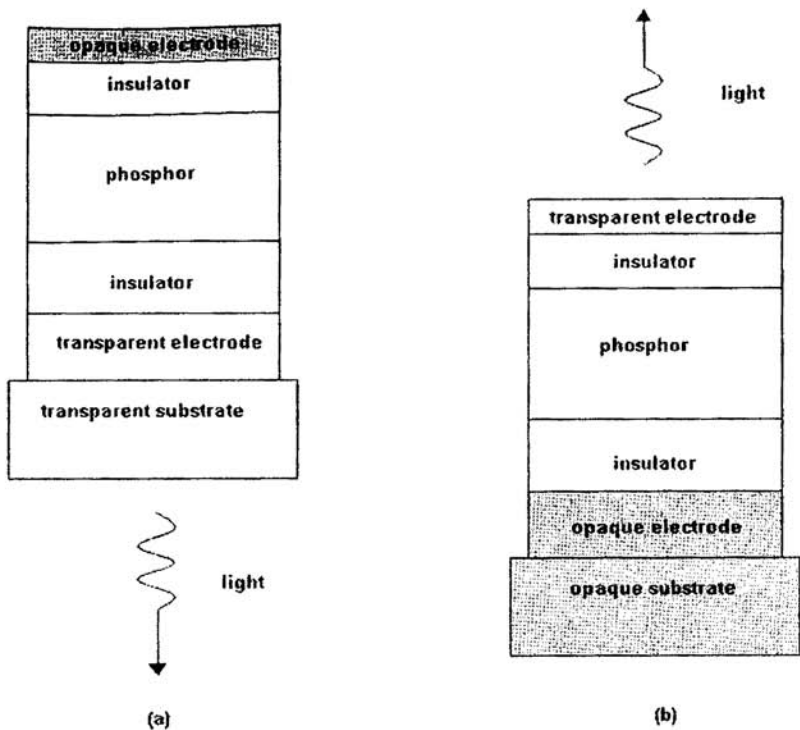


Figure 1.2 (a) The standard ACTFEL device structure. (b) The inverted ACTFEL device structure

The standard and inverted ACTFEL device structures are both used in commercial processes, and the choice of which structure to use is often dictated by process requirements, process limitations or intended device applications. The standard structure is the preferred structure for test devices and monochrome passive matrix displays because it requires a less complex process than the inverted structure. The most important advantage of the standard structure is that it exhibits self-healing breakdown when a suitable top electrode is deposited. The self-healing breakdown property prevents

small pinholes and defects from causing catastrophic device failure by effectively open-circuiting microscopic defective areas of the ACTFEL device [5]. Another advantage of the standard structure is inherent durability because the active device layers are shielded from the viewer by the glass substrate. However, the inverted structure possesses several distinct advantages over the standard structure, and is preferred for certain applications. When high temperature process steps are necessary, the standard structure is unusable because the glass substrates necessary for this structure begin melting around 600<sup>0</sup>C. Unlike the standard structure, there is the option of depositing on opaque substrates when the inverted structure is employed, allowing the use of high temperature tolerant ceramic or silicon substrates. Another case where the inverted structure is preferred over the standard structure is when colour filtering is required. When adding filter layers to a device it is advantageous to deposit these layers on top of a finished device because simple organic colour filters that are sensitive to process steps can be used. When the standard structure is employed, it is necessary to deposit the color filter layers first because light is viewed through the substrate [4].

The main disadvantage of the inverted structure is that self healing breakdown characteristics are not achievable with transparent top electrodes. This necessitates extremely low defect density ACTFEL devices for stable and reliable inverted structure ACTFEL device operation. This requirement greatly increases the processing complexity, and hence cost, because special processing techniques are required.

The third ACTFEL device structure that is sometimes used for testing purposes is the one insulator structure. The one insulator structure is essentially either the standard structure or the inverted structure minus either

of the insulator layers. This structure is used in ACTFEL testing because the elimination of an insulator deposition process step allows devices to reach the testing phase more rapidly. For certain applications, a one insulator structure is used with the phosphor layer deposited directly on a thick insulating ceramic sheet that serves the dual purpose of the substrate and an insulator layer. Although the one insulator structure has advantages in terms of ease of device fabrication, it is not used in commercial products because it exhibits lower luminance, affords less protection for the phosphor layer, and is not compatible with long-term device reliability [6].

## 1.5 ACTFEL operation

The operation of a two insulator ACTFEL device is discussed in this session. When an ACTFEL device is driven by AC voltages with amplitude below the threshold voltage of the device, the electrical characteristics are akin to a simple capacitor. The insulating layers and the wide bandgap semiconductor phosphor layer all have equivalent capacitances computed from the formula for the capacitance of parallel plates,

$$C_{\text{layer}} = \frac{\epsilon_r \epsilon_0}{t_{\text{layer}}} \quad (1.1)$$

Since an ACTFEL device consists of simple layers deposited one on top another, the device looks like a capacitor with a capacitance equal to the capacitances of the individual insulator ( $C_i$ ) and phosphor layers ( $C_p$ ) in series,

$$C_t = \frac{C_p C_{i,top} C_{i,bottom}}{C_p C_{i,top} + C_p C_{i,bottom} + C_{i,top} C_{i,bottom}} \quad (1.2)$$

Generally the insulator layers are lumped together and treated as a single capacitance where

$$C_i = \frac{C_{i,top} C_{i,bottom}}{C_{i,top} + C_{i,bottom}} \quad (1.3)$$

which leads to the total capacitance  $C_t$  being expressed as

$$C_t = \frac{C_i C_p}{C_i + C_p} \quad (1.4)$$

An important parameter in the operation of an ACTFEL device is the field across the phosphor layer. When a device is driven below the threshold voltage, the phosphor field  $f_p$  is given by

$$f_p = \frac{C_i}{C_i + C_p} \frac{V_{\text{applied}}}{t_p} \quad (1.5)$$

where  $t_p$  is the thickness of the phosphor layer. Then, when the amplitude of the AC driving voltage reaches the threshold voltage of the ACTFEL device, charge begins to flow through the phosphor, and this purely capacitive behavior is no longer witnessed.

Assuming that an ACTFEL device is being driven by an AC voltage with amplitude greater than its threshold voltage, the zero-order model of device operation proceeds in the following manner.

When the magnitude of the applied voltage is below the turn-on voltage of the ACTFEL device, it behaves as a simple capacitor [7-9] as described above. Then, when the magnitude of the applied voltage waveform reaches the turn-on voltage of the ACTFEL device, electrons are tunnel emitted from the phosphor-insulator interface on the cathodic side of the device, labeled as process 1 in the energy band diagram represented in figure1.3. The high electric field present in the phosphor layer of the ACTFEL device causes the emitted electrons to drift across the phosphor layer(process 2 in Fig1.3) [10]. On their way across the phosphor layer, electrons may collide with luminescent impurities that absorb some of the energy of impact and are subsequently promoted to an excited state (process 3 in figure1.3). The excited luminescent impurities relax to their ground states they may release the additional energy either through the emission of a photon of wavelength particular to the nature of the luminescent impurity (process 4 in figure1.3), or via phonon emission.

Obviously, for the sake of optical device efficiency, a large percentage of excited state to ground state transitions that release photons is preferred. The electrons that have slowed from the kinetic energy loss due to the collision quickly gain kinetic energy from the field and may excite additional luminescent impurities as they continue to traverse the remainder of the phosphor layer. Then, as the electrons reach the opposite, or anodic, phosphor-insulator interface, they are captured by one of the many electron traps present due to the disorder of the phosphor- insulator heterojunction (process 5 in figure1.3).

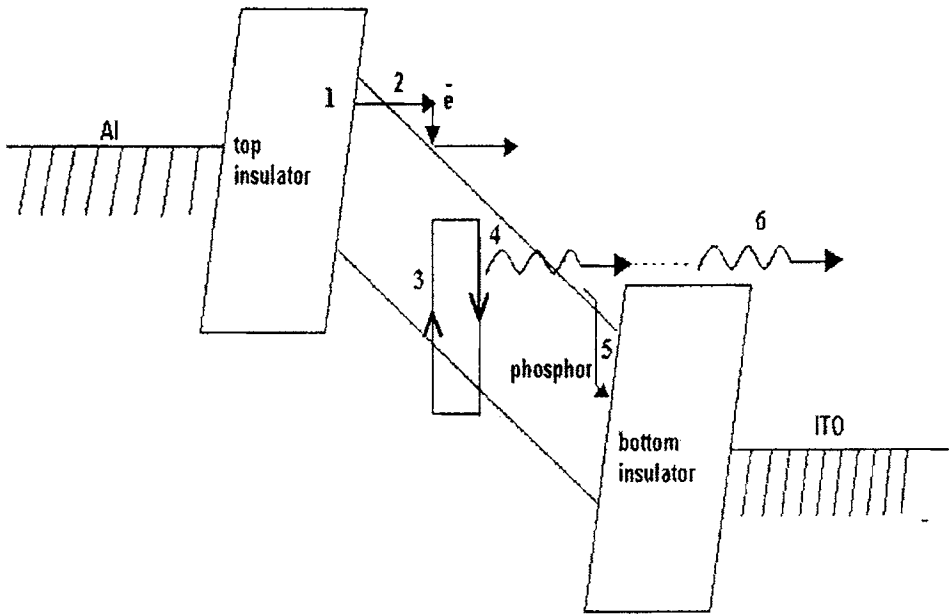


Figure 1.3 Zero-order model of ACTFEL operation. 1. Injection of electrons from the interface states by tunneling, 2. Transport of electrons, 3. Impact excitation, 4. Radiative recombination, 5. Trapping of electron and 6. Optical outcoupling.

Finally, the photons released by the luminescent impurities outcouple from the device to reach the viewer (process 6 in figure 1.3). When the AC waveform changes sign, this process repeats in the opposite direction. Much of the charge that has accumulated at the phosphor-insulator interface persists through interpulse intervals of low duty-cycle waveforms thereby altering the turn-on voltage of the following pulse of opposite polarity. This is the reason it is necessary to differentiate between the threshold and turn-on voltage of an ACTFEL device.



This simple model of ACTFEL device operation serves to aid in understanding many of the basics of device operation. There are several complications to this simple model that occur in real devices which often make ACTFEL device analysis difficult. The most important and well researched deviation from the zero-order ACTFEL device model is phosphor space charge. An operating ACTFEL phosphor is an environment especially prone to the creation of bulk space charge because of the high fields involved in device operation and the large number of defects present. Phosphor space charge has been attributed to three main causes in the literature: field emission from bulk traps[11-13], impact ionization of deep-level traps [13-17] and band-to-band impact ionization with subsequent hole trapping. Phosphor space charge has generally been assumed to be positive because all of the II-VI wide bandgap semiconductors that are generally used as ACTFEL phosphors are intrinsically n-type materials[18-22]. Additionally, most of the luminescent impurities that are added are donor impurities[11]. There has always been speculation that negative space charge may arise in certain circumstances [23], and no one has presented conclusive evidence to this end. The presence of space charge in the phosphor layer leads to a non-constant phosphor field profile. The major complication of this non-constant field profile is that it accentuates the field in certain regions of the phosphor while suppressing it in others. This leads to a non-uniform distribution of space charge throughout the phosphor layer. Since interface emission depends on the phosphor field at the emitting interface [24], phosphor space charge can have a profound effect on current due to interface emission.

Research has shown that space charge exists in almost all ACTFEL devices. Quantifying the amount and location of the space charge has proven more difficult. Several papers have been published that give estimates of the

average amount of space charge across the phosphor layer for both ZnS: Mn and SrS:Ce phosphors [25,26], but measurement of the space charge distribution across a phosphor layer has not been reported. Simulations of ZnS:Mn devices have been performed that yield a space charge distribution across the phosphor. Certain phosphor materials have a much greater predisposition to exhibiting space charge related effects, which leads to the belief that certain phosphor layers have much greater levels of space charge than others. These effects may have more to do with the amount of interaction between the conduction charge and the space charge than the physical amount of space charge in the phosphor.

Another area that is not well understood which may affect device performance is the role of holes in the operation of an ACTFEL device. Several authors have reported evidence for the existence of holes during the operation of ZnS based ACTFEL devices [27-32]. It is not known how much of the measured conduction charge is contributed by holes, whether they excite luminescent centers, and how efficiently they can be trapped in the phosphor layer. The II-VI wide-bandgap semiconductors normally employed as ACTFEL phosphors are materials that are known to trap holes because of the high density of native deep-donors, so this may contribute to space charge effects considerably. However, the trapping efficiency for carriers in SiO<sub>2</sub> is known to decrease exponentially with increasing field [33], implying that the trapping efficiency of the wide-band gap sulfide phosphors could also be very low at the high fields in ACTFEL device. It is still debatable what the role of holes might be in ACTFEL operation.

The third great mystery in ACTFEL device operation is the interface state density. Several authors have tried, rather unconvincingly, to measure the interface state density of an ACTFEL device [34-36]. This has generally led

to the conclusion that a high density of interface states exists at energies deeper than about 0.9eV below the conduction band in ZnS:Mn. However, a field profile change due to the presence of space charge in the phosphor layer invalidates most of these measurements. When band-to-band impact ionization occurs in the phosphor layer, it may appear that much more charge is being sourced from the emitting interface than is actually monitored in an external measuring circuit. These difficulties combine to leave little knowledge of the actual interface distribution in ACTFEL devices, although recent insights into the quantity of phosphor space charge present in an operating ACTFEL device suggest that the peak of the interface state distribution is much deeper than originally thought [37,38].

## **1.6 ACTFEL materials**

### **1.6.1 The phosphor layer**

The most important layer of an ACTFEL device in terms of determining its optical characteristics is certainly the phosphor layer because it is the phosphor layer that converts electrical energy into light energy. In addition, the electrical characteristics of an ACTFEL device are strongly dependent upon the nature of the phosphor layer. The phosphor layer of an ACTFEL device is composed of a phosphor host doped with substitutional luminescent impurities of the order of 0.1 molar percent.

The phosphor host is the material that provides a host lattice for substitutional luminescent impurities. Many different materials and families of materials have been investigated as phosphor host materials. The specific demands on ACTFEL phosphors relative to phosphors for other applications

render many phosphor hosts unusable in an ACTFEL device. The commercially viable ACTFEL phosphor hosts are, without exception sulphides, presumably because of superior charge injection properties. The substitutional luminescent impurities, or activators, that are doped into the phosphor host are the ions from which the light that is visible to the viewer is emitted. The colour spectrum of the light emitted from a phosphor is determined to a large extent by the nature of the luminescent impurity. The host lattice influences the colour spectrum emitted by a luminescent impurity because different phosphor hosts present different local crystal fields in terms of both field strength and field symmetry.

Depending upon the nature of the luminescent transition, the crystal field may be very important or merely a perturbation in determining the colour spectrum of the phosphor. For example, the  $4f \rightarrow 4f$  luminescent transitions characteristic of many of the rare-earth ions are relatively insensitive to the crystal field of the host lattice because the  $4f$  orbitals are not the chemically interacting orbitals. Such luminescent transitions are known as “shielded” transitions. On the other hand, the  $Mn^{2+}$  luminescent impurity is very sensitive to the crystal field presented by the host lattice because the luminescent transition originates from the outermost electronic shell. This type of luminescent transition is strongly dependent on the host lattice, allowing the possibility to alter the color spectrum by adjusting the crystal field. The crystal field is adjusted in practice by adding additional dopants which affect the lattice constant of a phosphor, thereby influencing its luminescent properties. Additional atoms that are added to a phosphor that influence its luminescent properties, whether they alter the colour spectrum or simply affect the luminance, are termed coactivators. As a result, almost all of the naturally occurring atoms in the periodic table have been employed as either luminescent impurities or coactivators in various phosphor hosts.

Bulk phosphor is prepared by solid state reaction. Required proportions of phosphor host and dopants (activator and coactivator) are mixed well in alcohol medium. The dried mixture is then fired at or above the crystallization temperature of the host material in a furnace.

There are several common deposition techniques for growing phosphor films; rf sputtering, thermal evaporation, electron-beam evaporation, and atomic layer epitaxy (ALE). Each of these deposition techniques has distinct advantages and disadvantages for ACTFEL phosphor deposition. A deposition technique that is optimal for a particular phosphor material may produce substandard quality thin-films for a different phosphor system. Even when a commercial quality ACTFEL phosphors can be deposited by all of the techniques mentioned above, there are often noticeable differences in phosphor characteristics depending on the method of preparation. Therefore, it is important to have the capability to deposit an ACTFEL phosphor by a variety of techniques to fully gauge its viability. For example, Tb-activated ZnS is a much brighter and more efficient ACTFEL phosphor when sputtered than when evaporated or deposited by ALE [4].

The performance of an ACTFEL phosphor is typically gauged by several important output parameters; luminance (brightness), efficiency, and color coordinates. The luminance or brightness, of an ACTFEL device is a measure of the amount of visible light emitted in a direction normal to its surface. The efficiency of an ACTFEL device is a measure of light output per unit electrical power input. The efficiency of an ACTFEL device is generally reported in lumens per Watt (lm/W), where a lumen is a measure of the light emitted in all possible emission directions from the surface of the ACTFEL device. The Commission Internationale de l'Eclairage (CIE)

colour coordinates are the x and y coordinates on a two-dimensional surface that represents the entire gamut of visible colours. Therefore, CIE coordinates are a method for quantifying the color of an ACTFEL device. It should be noted that while the luminance, efficiency, and CIE coordinates of an ACTFEL device are typically attributed to the phosphor layer, these values are influenced to some degree by the nature and quality of the other layers of the ACTFEL device.

Currently, Mn-activated ZnS and Ce-activated SrS are the only two ACTFEL phosphors with the luminance, efficiency and stability to be the basis of a commercial product. The most common and well researched ACTFEL phosphor is ZnS activated with  $Mn^{2+}$ , or ZnS:Mn. This phosphor material emits amber colored light and is the basis for most of the current commercially available ACTFEL-based products. The second most common ACTFEL phosphor is SrS:Ce. This phosphor material emits blue to green light depending on the codopants and processing conditions. The SrS:Ce phosphor is most often used commercially in conjunction with ZnS:Mn and colour filters to produce multicolor ACTFEL displays.

There are two approaches to produce a full-colour ACTFEL display, the colour-by-white approach and the patterned phosphor approach. The colour-by-white approach involves filtering a white ACTFEL phosphor to produce the three primary colours; red, green, and blue. The patterned phosphor approach to full color is based on the idea of patterning pixels of different phosphors that emit the three primary colours. Unfortunately, neither ZnS:Mn nor SrS:Ce is of a colour that is similar to white or any of the saturated primary colors. Therefore, these phosphors must either be used for monochrome displays or as components of multi-phosphor ACTFEL devices that try to achieve a white colour by mixing two or three phosphor layers in

the same device. Due to this lack of adequate chromaticity, there is ongoing research to produce phosphors of the three primary colours. Table 1.2 presents a list of the target luminancees, efficiencies and CIE coordinates for the three primary colors.

Table 1.2 Target luminance, efficiency and CIE coordinates (60Hz) for a high – luminance full- colour ACTFEL display

Colour	$L_{40}(\text{cd}/\text{m}^2)$	$\eta$ (lm/W)	CIE x	CIE y
Green	310	2.0-3.0	0.30	0.60
Red	155	1.0-1.5	0.65	0.35
Blue	52	0.3-0.5	0.15	0.10

The introduction of blue emitting SrS: Cu and SrS: Cu,Ag phosphors has sparked renewed optimism that competitive full-color ACTFEL displays may soon become a reality [39,40]. This optimism is fueled by the fact that the best blue phosphors prior to the introduction of SrS:Cu and SrS:Cu,Ag were the Ce activated alkaline earth thiogallates,  $(\text{Sr,Ca})\text{Ga}_2\text{S}_4:\text{Ce}$ , which had excellent chromaticity but insufficient luminance and efficiency. The high luminance of blue SrS:Cu and SrS:Cu,Ag phosphors means that corresponding strides in the luminance of the green and red emitting phosphors needs to be made. Fortunately, it was discovered that the SrS:Cu phosphor codoped with Eu results in impressive red ACTFEL devices. Therefore, of particular importance is the green phosphor because the best green phosphors known to date are insufficient for utilization in a practical display. The brightest known green emitting phosphor filtered ZnS:Mn exhibits chromaticity that is significantly different than saturated green and hence inadequate for full colour display applications. The only bright,

saturated green ACTFEL phosphor known to date ZnS:Tb has poor stability, and is hence unlikely to lead to a robust product. Furthermore, the eye is approximately 6 times more sensitive to green light than blue light and approximately twice sensitive to green light than red light, making green perhaps the most important of the three primary colour phosphors. Additionally, a bright and stable green phosphor would open up certain markets to ACTFEL based products, because green is the preferred color for monochrome display.

### **1.6.2 Insulators**

In traditional ACTFEL devices, the insulating layers sandwiching the phosphor layer have been quite important for proper device operation. The most important role of the insulator layers is to protect the phosphor layer from large currents that flow when the phosphor is driven to electrical breakdown. In addition, the insulating layers have some influence on the important phosphor-insulator interfaces that supply the electronic current leading to light generation in the phosphor. Furthermore, they must withstand annealing temperatures up to 800<sup>0</sup>C for the “standard structure”, and over 1000<sup>0</sup>C for the inverted structure without significant crystallization or defect formation. Finally, they should prevent ionic diffusion of foreign species into the phosphor layer. The generally accepted requirements of insulators for ACTFEL applications are as follows [4]:-

1. sufficient relative dielectric constant,  $\epsilon_r$
2. sufficient dielectric breakdown electric field,  $F_{BD}$
3. small number of pinholes and defects
4. good adhesion to the electrodes and phosphor layer
5. small loss tangent,  $\tan\delta$



The ratio of insulator capacitance and phosphor capacitance is very important in determining how efficiently the applied voltage is dropped across the phosphor layer. Since the capacitance of the insulator layers depends on the relative dielectric constant  $\epsilon_r$ , it is a crucial parameter in deciding on applicable insulators for a given phosphor. Ideally,  $C_i$  should be much greater than  $C_p$ , which implies that the relative dielectric constant of the insulator layer should be as large as possible, while the insulator thickness should be as small as possible. There are practical limits to both insulator dielectric constant and the insulator thickness.

Insulators thinner than about  $500\text{\AA}$ <sup>0</sup> tend to show signs of charge leakage that degrades device performance [41]. Also, if the phosphor layer becomes a virtual short when the device is turned on, the additional voltage applied above the turn-on voltage is dropped across the insulator layers, meaning that thinner insulators will see higher fields than thicker insulators. Therefore, the insulator layers must possess significant breakdown fields if they are to be useful for ACTFEL applications. High dielectric constant materials generally have fairly low breakdown fields and vice versa. In addition, most insulators that possess relative dielectric constants above about 40 tend to break down in a mode termed “propagating breakdown”. Propagating breakdown means that if a small portion of the insulator breaks down, a short circuit is formed through the insulator that heats up and grows in size, causing catastrophic device failure. The insulator breakdown mode for most of the lower relative dielectric constant materials is the so-called self-healing breakdown mode, where microscopic insulator breakdowns become open-circuited, and hence do not grow in size.

A minimum number of pinholes and defects in an insulator is important because displays with diagonals up to several inches are produced, and

pinholes and defects will certainly degrade the overall quality of the display. Furthermore, any pinholes or defects in a propagating breakdown mode insulator can lead to catastrophic failure of the display. This is the reason why propagating breakdown mode insulators are generally sandwiched between self-healing breakdown mode insulators if they are used at all in ACTFEL applications. Also good insulator adhesiveness is quite obviously necessary if an ACTFEL display is going to withstand the test of time.

The ACTFEL phosphor is a relatively closed environment when sandwiched between two insulators as in the standard and inverted device structures. This implies that charge loss or injection through the insulators can disrupt the delicate balance inherently present in the device. In addition, charge leakage through the insulators can lead to reduced device efficiency because of power loss due to this process. For this reason it is generally believed that charge leakage through the insulators is detrimental to device performance. As a result, it is desirable to keep the loss tangent,  $\tan \delta$ , of the insulator layers as small as possible.

### **1.6.3 Transparent contacts**

The light generated by the phosphor layer of an ACTFEL device must reach the viewer for a useful device. Hence, at least one of the electrical contacts needs to be a transparent conductor that possesses high transmittance in the entire visible spectrum. Also of importance is a low electrical resistance of the transparent conductor to avoid excessive resistive heating and hence wastage of power in the display. Moreover the transparent conductor must be able to withstand anneals of up to  $800^{\circ}\text{C}$  in the standard process. Several materials have been used for this purpose, but the best and by far the most

common is indium tin oxide (ITO), an alloy of approximately 90 wt.%  $\text{In}_2\text{O}_3$  and 10 wt.%  $\text{SnO}_2$ . This material is transparent to visible light because the bandgaps of both  $\text{In}_2\text{O}_3$  and  $\text{SnO}_2$  are about 3.5 eV. This material conducts due to the high density of donor impurities caused by oxygen vacancies and  $\text{Sn}^{4+}$  ions sitting on  $\text{In}^{3+}$  sites. Other materials that have been used for the transparent contact in research devices are  $\text{ZnO:Al}$ ,  $\text{ZnO:Ga}$ ,  $\text{ZnO:In}$ ,  $\text{CdO}$ , and  $\text{CdSnO}_3$ . The major problem with transparent contacts is that they are not conducive to self-healing breakdown. Self healing breakdown is not merely a function of the insulator material, but is also dictated to a large extent by the contacts. This is due to the fact that self-healing ACTFEL device behavior is also dependent on either the evaporation or melting and surface migration of the exposed contact above short circuits caused by microscopic pinholes and defects.

#### **1.6.4 Opaque contacts**

Generally, one of the electrical contacts to an ACTFEL device is an opaque conductor. Almost all standard structure ACTFEL devices are contacted on the top by an Al electrode. Aluminum is used because it adheres well to most insulators, does not migrate through the device under high electric fields, and has low resistivity. There are two main disadvantages of Al as the opaque contact to an ACTFEL device. The first is that it reflects around 90% of incident light such that background light is reflected and emerges along with the electroluminescent light. The second is that the melting point of Al is  $660^\circ\text{C}$ , meaning that it is not useful for inverted structure applications where high temperature post deposition anneals are used. For this application, a suitable refractory metal is used, usually Mo, Ta, or W [4].

## 1.6.5 Substrates

In the production of standard structure ACTFEL devices, the substrate is typically Corning 7059 phosphosilicate glass, or its equivalent, with a softening temperature about  $600^{\circ}\text{C}$ . As a result, large size display panels will withstand rapid thermal annealing (RTA) at temperatures below  $650^{\circ}\text{C}$  without warping. However, smaller sized test samples ( $\leq 2''$  square) will withstand RTA temperatures as high as  $850^{\circ}\text{C}$  for several minutes without significant warpage. For certain phosphors it has been essential to perform higher temperature anneals with the standard structure, so higher softening temperature glass substrates are used. However, the drawback of these higher temperature glass substrates is that they are many times more expensive than the Corning 7059 glass; too expensive, in fact, to produce an economical product. These higher softening temperature glass substrates only provide  $100\text{-}200^{\circ}\text{C}$  of additional annealing temperature range before they too succumb to the high temperature. For truly high temperature annealing, the inverted structure is necessary. Since the light is viewed through the top of the device in the inverted structure, opaque substrates are an option. With opaque substrates, silicon wafers are a logical choice because they are readily available and melt at  $1412^{\circ}\text{C}$ . Also, alumina ceramic substrates are often used because of their availability, economy, and extremely high melting temperature.

The final substrate type that is sometimes used for research devices with oxide phosphors is the  $\text{BaTiO}_3$  substrate [6, 42]. These substrates are pressed from powder and sintered and ground into a flat ceramic disc. Then, an oxide phosphor layer is deposited directly onto the substrate. The device is annealed at temperatures of the order of  $1000^{\circ}\text{C}$ . A transparent conductor is

deposited onto the phosphor layer and an Al contact is deposited on the backside of the substrate. The main advantage of this configuration is that it allows high temperature anneals. However, there are extreme over voltage requirements when this device structure is employed because the insulator capacitance dictates how efficiently the applied voltage is coupled to the phosphor layer and the small insulator capacitance resulting from driving the substrate results in very poor coupling. This problem with the over voltage requirement makes this structure fairly useless from an industrial perspective, at least with currently available drive electronics.

## **1.7 Properties of ACTFEL phosphor host materials**

### **1.7.1 Band structure**

The bandgap of a phosphor host material intended for ACTFEL applications is extremely critical to device performance because it is closely intertwined with carrier injection from the interfaces. A material with a smaller bandgap often has relatively shallow interface states that emit at a field too low to result in a hot enough electron distribution to efficiently impact excite the activator ions. On the other hand, a material with a bandgap that is too large often has relatively deep interface states that do not emit an appreciable number of carriers at realizable driving voltages (<300V). Also, if the bandgap of the phosphor material is too small, optical absorption of emitted photons may occur in the phosphor layer, and therefore the emitted light will never reach the viewer. In this framework, the absolute minimum and maximum for phosphor bandgap are 3.5 and 4.5 eV respectively. However, the practical minimum and maximum for the bandgap of commercially relevant phosphor materials is probably closer to 3.5 and 4.5 eV

respectively. With these limits in mind, it should be noted that bandgap values for many materials are either unknown, difficult to locate, or unreliable. Although bandgap values for many binary compounds are available and known with some degree of confidence, bandgap values of ternary compounds are often quite difficult, if not impossible, to locate.

The transition type of the bandgap and the effective masses are interrelated materials parameters that allow significant insight into the potential of a material for ACTFEL phosphor applications. The transition type of the bandgap is either direct or indirect depending on whether the conduction band minima and valence band maxima occur at the same wavevector in the first Brillouin zone. The bandgap transition type is extremely important in determining the performance of many optoelectronic devices because it strongly affects the likelihood of certain optical transitions.

### **1.7.2 Dielectric permittivity**

For efficient ACTFEL device operation, the goal is to generate a high field in the phosphor layer to initiate charge conduction and hence electroluminescence. When an external voltage ( $V_{\text{applied}}$ ) is applied to an ACTFEL device, only a fraction appears across the phosphor and the remainder drops across the insulators. The phosphor field generated due to an applied voltage below the threshold voltage of the device is given in eq. (1.5). It shows that the ideal situation for an ACTFEL device is to have  $C_p \ll C_i$ . This means that the relative dielectric constant of the phosphor layer should be low enough such that phosphor fields of a magnitude that initiate charge conduction in standard thickness ACTFEL phosphors ( $2000\text{\AA}^0 \leq t_{\text{phosphor}} \leq 2.0\mu\text{m}$ ) can be achieved well within the limits of the

available power supplies. With the current insulators used for ACTFEL applications, the practical maximum for phosphor relative dielectric constant is about 15. However, positive space charge in the phosphor layer that is generated prior to the threshold voltage may relax this limit for phosphors prone to this behavior.

### **1.7.3 Melting temperature**

The successful fabrication of an ACTFEL device critically relies on the rearrangement and ordering of the atoms composing the phosphor thin film during some stage in the processing. Numerous studies have shown that ACTFEL luminance and efficiency are closely coupled to the polycrystalline grain size of the phosphor film [43-47]. The degree of crystallinity of a phosphor material is critically important in determining the luminance and efficiency of an ACTFEL phosphor because it determines the potential for delocalized carrier transport through the phosphor [48]. Delocalized transport is critical because it allows the carrier distribution to become much hotter than if conduction occurs via hopping, such as what occurs in amorphous materials. A hotter carrier distribution results in better impact excitation efficiency, and hence brighter and more efficient light output.

To obtain the phosphor host crystallinity, necessary to generate bright and efficient ACTFEL phosphors of a repeatable color spectrum, thermal post-deposition heat treatments are typically performed. The thermal post-deposition heat treatment typically applied to ACTFEL phosphor thin-films is the rapid thermal anneal (RTA). This is an advantageous technique because the substrate temperature can be ramped up and cooled very rapidly, allowing temperatures well in excess of the substrate melting temperature to

be obtained for short periods of time. Due to the exponential dependence of the atomic diffusivity with temperature, this technique holds inherent advantages over furnace sintering from the standpoint of providing greater recrystallization at a higher throughput.

Prediction of the annealing temperature and time required to achieve polycrystalline grain growth for a hypothetical phosphor host often proves difficult. It is suggested in the literature that polycrystalline grain growth typically begins at temperatures approximately one-half of the absolute melting temperature [49]. Therefore, the melting temperature of a material is probably the best insight available into the annealing cycle required to reach the onset of polycrystalline grain growth.

This simple rule-of-thumb regarding the onset of sintering implies that potential phosphor hosts with melting temperatures above roughly 1300<sup>0</sup>C are too refractory to lead to bright and efficient ACTFEL devices on substrates that cannot withstand anneals in excess of 650<sup>0</sup>C. It is for this reason that the temperature of grain growth is perhaps the most important constraint on ACTFEL phosphors because many well known phosphors require ~1000<sup>0</sup>C post deposition anneals for bright and efficient operation. This situation can be alleviated by the deposition of ACTFEL devices onto ceramic or silicon substrates in an inverted structure, allowing for very high temperature annealing cycles ( $\leq 1200^{\circ}\text{C}$ ). However, the inverted structure is prone to unstable ACTFEL devices unless deposited essentially pinhole and defect free. The means typically employed to achieve a reduction of the temperature required to achieve polycrystalline grain growth is the addition of flux agents.



### 1.7.4 Ionicity

The important electronic properties of most semiconducting and insulating materials are governed to a large extent by defects, whether intentionally added or not. The principal element in determining the concentration of stoichiometric defects in a material is the degree of ionic bonding of a compound. Ionic materials typically have large concentrations of stoichiometric defects, especially Schottky defects, or vacant lattice sites, whereas covalently bonded materials tend to have very few imperfections of this sort [50].

Since the currently known ACTFEL phosphor hosts have an appreciable ionic bonding character and rely quite heavily on defects and impurities for effective operation, the ionicity of a potential phosphor host is an important parameter. It has long been theorized that stoichiometric defects are responsible for the space charge in ACTFEL phosphors that is so intertwined with their operation. The greater tendency for the more ionic SrS phosphor host to exhibit space charge related phenomena than ZnS lends credence to the theory that stoichiometric defects are the underlying cause of space charge in ACTFEL phosphors [51]. Furthermore, the addition of luminescent activators and coactivators of different valence than the phosphor host constituents is known to lead to an effect called self compensation in which it is energetically favorable to create additional stoichiometric defects than to further shift the Fermi level toward the band edge [52]. However, the self compensation mechanism typically acts preferentially towards creating either anion or cation vacancies depending on the energetics of formation of the given defect. Therefore, the degree of ionicity of a phosphor host gives an indication of the degree to which it should be extrinsically compensated

to avoid potentially deleterious effects of self compensation as noted by Lehmann in his study of alkaline earth sulphide phosphors [53].

It is also likely that the important interface behavior of an ACTFEL device is impacted to a certain degree by the ionicity of the phosphor host. It has long been known that the Schottky barrier height of covalent semiconductors such as Si and Ge is largely unaffected by the work function of the metal layer because the Fermi level is pinned by an abundance of interface states [54]. It is also known that the Schottky barrier height of the more ionic semiconductors such as ZnSe, ZnS and CdS is primarily dependent upon the work function of the metal because of a much lower density of interface states [55]. Furthermore, it has been experimentally confirmed that significant surface reconstruction occurs with the purely covalent elemental semiconductors and the primarily covalent compound semiconductors [56]. However, surfaces of highly ionic compounds such as alkali halides show almost abrupt termination of the lattice, with very little surface reconstruction [57]. Presumably, because of the very different surface behavior in terms of surface reconstruction and Schottky barrier interface states between ionic and covalent compounds, the ionicity of a compound should somewhat determine its ability to form the interface states that source the electronic charge in an ACTFEL device. This leads to the conclusion that the degree of ionicity roughly corresponds to the degree to which a prospective phosphor departs from the interfacial model of ACTFEL operation. In fact, the best known ACTFEL material in terms of interface injection is ZnS which is much less ionic than the other well known ACTFEL phosphor hosts.

### **1.7.5 Thermodynamic stability**

Thermodynamic stability of the constituent materials is an absolute necessity for the production of long lived, stable electronic devices of any type. The harsh environment seen by an ACTFEL phosphor host in terms of high fields and temperatures implies that thermodynamic stability is an absolute must. Furthermore materials that are near the edge of stability should be avoided for ACTFEL applications because high operating temperatures may drive such materials to spontaneously dissociate.

### **1.7.6 Moisture sensitivity**

A classic problem with many otherwise excellent phosphor host materials is their instability in the presence of moisture. Materials that are unstable in the presence of moisture are classified as either hygroscopic or moisture sensitive, or sometimes both, depending on the mechanism that leads to their moisture related instability. Hygroscopic compounds are compounds that electrostatically bind polar water molecules, thereby becoming hydrated molecules. Since hygroscopic behavior is an electrostatic interaction, the odds of a material being hygroscopic increase with increasing molecular polarity. Therefore, compounds with a high degree of ionic bonding character are much more likely to exhibit hygroscopic behavior. In addition, the high density of atomic vacancies typically present in ionic compounds allow water molecules to diffuse easily into the bulk of the material [58]. On the other hand, compounds that are deemed “moisture sensitive” are typically compounds that are easily hydrolyzed. Unfortunately, some of the best phosphor host materials for ACTFEL devices exhibit hygroscopic

behavior and moisture sensitivity, leading to increased processing cost and complication.

## **1.8 Activators**

Intentionally incorporated impurities into a wide bandgap semiconductor to obtain luminescence are known as activator. Two important parameters of an activator are its ionic radii and valency.

### **1.8.1 Ionic radius**

Several bright and efficient ACTFEL phosphors are known where ionic radii of the activator and the atom it replaces in the lattice, typically the cation, are not closely matched. However, the matching of the activator and cation ionic radii may be advantageous for several reasons. First, gross discrepancies between the ionic radii of the activator and cation lead to lattice strain induced defects, poor crystallinity and device stability problems. The defects so produced can provide non-radiative paths to the ground state for excited activator ions, and hence reduce ACTFEL device luminance and efficiency. Activators much larger than the atom that they replace in the lattice may inhibit polycrystalline grain growth because their large size may prevent ionic diffusion during annealing. In addition, these large activators may be difficult to incorporate into the lattice because they may have difficulty in diffusing into proper sites in the lattice during annealing. Activators that are much smaller than the cation which they replace are potential interstitial impurities that can lead to device stability problems. In addition, a small activator ion replacing a large cation may be induced to move in the lattice as a result of high temperature operation or the high fields typical of an

ACTFEL phosphor. With this having been said, ZnS:Tb and SrS:Cu are still the brightest known ACTFEL phosphors for their respective colours, although both show instabilities that may be linked to ionic radii mismatches.

### **1.8.2 Valency**

The valency of the activator of an ACTFEL phosphor has important implications in terms of material defect chemistry. As a result of the charge neutrality condition and the ionicity of most ACTFEL phosphor host materials, impurities that are not isovalent with the atoms of host lattice are intrinsically compensated. Self compensation in most materials with an appreciable ionic character occurs via the creation of Schottky defects, also known as vacancies. If widespread formation of Schottky defects is not desired, the valency of the activator and the cation should match. Alternatively, a non matching activator and cation valency can be extrinsically compensated through the addition of additional dopants, termed coactivators in phosphor terminology. Although valency matching is one of the classic criteria for determining a suitable phosphor host for a given activator, many of the brightest known ACTFEL phosphors violate this rule.

## **1.9 Stokes shift**

One of the main effects associated with host lattice-activator interaction is Stokes shift. Stokes shift is a measure of the shift of the emission spectrum relative to the excitation spectrum of a phosphor material. With the aid of the configurational coordinate diagram, the Stokes shift phenomenon can be explained in a simple and straightforward manner. When an activator absorbs energy, it is promoted from the ground state to

the excited state as shown in Fig1.1. This transition is represented by an arrow pointing straight up from the center of the lowest vibrational state to the point on the excited state parabola directly above it. This arrow points straight up because the transition is an electronic transition, which occurs on a much smaller timescale than an atomic transition due to the mass difference between electrons and atoms. The arrow begins at the center of the lowest vibrational state  $R_0$  because it is most likely that the activator is in the lowest vibrational state and the most probable interatomic distance for this vibrational state is  $R_0$ . The transition probability is proportional to the convolution of the probability distribution of the emitting vibrational state with the vibrational state that is emitted into. Therefore, the arrow ends at the point on the excited state parabola with an interatomic distance value  $R_0$  because the most probable interatomic distance at upper vibrational levels is near the parabola. Then, when the activator is in upper vibrational levels of its excited state, it typically relaxes to the lowest vibrational level of the excited state before returning to its ground state. As a result the emission wavelength and the absorption wavelength differ by the amount of energy lost to vibrational relaxation. This nonradiative energy loss due to vibrational relaxation is termed Stokes shift.

## 1.10 Coactivators

Coactivators are quite varied in nature and are employed for several different tasks in the improvement of ACTFEL phosphors. Generally, ACTFEL phosphor coactivators fall into three different classes according to the function that they perform; flux agents, compensators and luminescent coactivators. One coactivator can perform two or more of the functions mentioned above in certain situations. The most important class of ACTFEL

phosphor coactivators in a broad sense are flux agents. The purpose of a flux agent in a phosphor material is to improve the crystallinity of the phosphor host lattice by assisting atomic diffusion during high temperature processing. Flux agents are extremely important for ACTFEL phosphors because they provide a means of achieving crystallinity at the low processing temperatures necessary for deposition onto glass substrates. Flux agents are typically non isovalent with the constituent elements of the phosphor host and either readily diffuse into or react with the phosphor host. The most effective flux agents are non isovalent with the constituent atoms of the phosphor host because their operation relies upon their ability to generate vacancies to compensate for their presence. It is these vacancies that lead to enhanced atomic motion through the phosphor enhancing the formation of a crystalline lattice. The most effective flux agents for ACTFEL phosphors are typically Li, Na, K, Cu, Ga, F, and Cl [59-61].

The activators of many of the most important ACTFEL phosphors known today are non isovalent with the atom that they replace in the host lattice, motivating the use of compensating coactivators. When a phosphor activator is non isovalent with the atom that it replaces in the host lattice, charge compensation is accomplished via the formation of vacancies (Schottky defects) in compounds with appreciable ionic character. The electrical and optical characteristics of ACTFEL devices based on such phosphor materials suggest that these defects heavily influence device operation. As a result, performance gains may be realized by controlling the defect chemistry through the addition of compensating coactivators [62, 63]. The emission spectrum of an ACTFEL phosphor may also be modified through the addition of compensating coactivators because all activators that are not line emitters are sensitive to their immediate surroundings. As a result, when

these activators complex with a defect, rather dramatic color shifts are sometimes observed.

Another class of ACTFEL phosphor coactivators that sometimes offer performance benefits are luminescent coactivators. Luminescent coactivators are ions that emit radiation of a wavelength that is strongly absorbed by the activator, and hence, enhances its light output. The red  $\text{Eu}^{2+}$  activator is often coactivated in this manner because it strongly absorbs blue light [64]. Therefore blue emitting Ce and Cu are efficient luminescent coactivators of  $\text{Eu}^{2+}$ . Since many luminescent impurities absorb strongly in the ultraviolet (UV) region of the spectrum, a UV emitter is a good luminescent coactivator candidate for a highly PL active phosphor.

## 1.11 Killer centers

The presence of certain atoms in a phosphor can severely degrade or even eliminate its luminescent properties. These atoms, called killer centers, degrade overall phosphor performance even when present in minute quantities. Some killer centers operate by strongly absorbing visible wavelength photons from the phosphor and subsequently relaxing by emitting non visible infrared (IR) photons [65]. Other killer centers extinguish a phosphor's luminescent properties by existing as a deep level that provides a non radiative path to the ground state for the excited activator ions. The most well known killer centers in ZnS phosphors are the iron group elements:  $\text{Fe}^{2+}$ ,  $\text{Ni}^{2+}$  and  $\text{Co}^{2+}$  which strongly absorb visible light. The presence of these atoms is also likely to cause degradation of overall phosphor performance for other phosphor materials and contact with these atoms should be avoided. The killer center effect often presents processing



problems because many standard pieces of deposition equipment are fabricated from stainless steel which is rich in these iron group elements. In addition, heating elements are often constructed from nichrome wire that can emit Ni at elevated temperatures. Therefore, many processing systems need to be custom-tailored to meet the specific needs for phosphor deposition due to killer centers.

## 1.12 Sulphide phosphors

The entire ACTFEL technology is built around sulphide phosphors, almost exclusively because of the success of ZnS:Mn the prototypical ACTFEL phosphor. In addition, recent advances with SrS:Ce and SrS:Cu phosphors have determined that they are extremely important phosphors for the realization of full color ACTFEL displays. These sulphide phosphors possess two properties that thus far seem to be unique to these phosphors, excellent charge injection and polycrystallinity at low processing temperatures. The charge injection characteristics of these phosphors seem to be due to the combination of a high density of interface states at the proper energy for tunnel emission at readily attainable driving voltages. The polycrystallinity attainable in these sulphide phosphors at temperatures under 800<sup>0</sup>C is good enough to lead to bright and efficient devices, thereby leading to the conclusion that transport is delocalized and not amorphous style hopping conduction. This is remarkable considering that the melting points of ZnS and SrS are 1700<sup>0</sup>C and >2000<sup>0</sup>C respectively. In fact, this gives hope that other refractory compounds may also become polycrystalline at processing temperatures commensurate with glass substrates. The deposition of sulphides is less complicated than that of oxides and nitrides because sulphur is significantly more condensable than oxygen or nitrogen.

This allows the simple evaporation of sulphides without the addition of a gaseous species to provide lost anionic atoms.

Although ZnS and SrS phosphors have several properties that help to create bright and efficient ACTFEL devices, the sulphide family as a whole tends towards mediocrity in terms of physical and thermodynamic properties. The bulk of the binary sulphide materials are thermodynamically stable; however, their thermodynamic formation energies are less than those of the corresponding oxides. In addition, the sulphides exhibit moisture sensitivity than oxides, leading to stability problems. The melting points of binary sulphides tend to be several hundred degrees centigrade lower than the corresponding oxide, on average. This leads to a much greater chance that sulphide compounds will exhibit polycrystallinity at standard ACTFEL processing temperatures than corresponding oxide and nitride compounds. The other problem that severely limits the number of potential sulphide phosphors is that only a few of the binary sulphides possess bandgap energies that are sufficient for ACTFEL applications.

The limited number of sulphide materials of sufficient bandgap results in only some sulphide compounds that are applicable to ACTFEL fabrication. In addition, extreme moisture sensitivity of several sulphide compounds ( $\text{SiS}_2$ ,  $\text{Al}_2\text{S}_3$ , and  $\text{GeS}_2$ ) renders them and their derivatives useless as ACTFEL phosphor hosts from a stability standpoint. Of the compounds of the sulphide family, only CaS, SrS, BaS, ZnS and  $\text{Ga}_2\text{S}_3$  or the resulting ternary thiogallates exhibit properties consistent with ACTFEL applications. The main limiting factors in terms of ACTFEL application for sulphides are insufficient bandgap and moisture sensitivity. Although the number of sulphide phosphor hosts is quite limited, the sulphide phosphor hosts, CaS, SrS, and ZnS are known to be versatile phosphor hosts in terms of the

40

number of potential activators. In fact, Lehmann's pioneering work on CaS phosphors identified not less than 31 luminescent activators in CaS. The same could be expected for BaS although significantly less work has been conducted with BaS phosphor hosts.

The aforementioned issues regarding sulphide phosphors allow an examination to be made concerning the potential for new phosphors to be discovered amongst the sulphide family. With the sulphides, the limited number of potential phosphor hosts results in the conclusion that no new sulphide phosphor hosts will be discovered. However, because of the versatility of the known sulphide phosphor hosts, there remains significant research work to be done in terms of determining proper activators, and especially, coactivators for these sulphide phosphors.

## 1.13 References:

1. D.R.Vij (Ed.) Luminescence of solids, New York, Plenum Press (1998)
2. G.Destriau, *J.Chem.Phys* **33** (1936) 587.
3. T. Inoguchi, M. Takeda, Y. Kakahara, Y. Nakata, and M. Yoshida, *J.SID* **5** (1974) 84.
4. Y.A.Ono, *Electroluminescent displays*. Singapore: World scientific, (1995).
5. I.Khormaei, *High resolution electroluminescent displays using active matrix approach*, PhD thesis, Oregon State University,(1995).
6. T.Minami, T.Miyata, S.Takata and I.Fukuda, *Jpn.J.Appl.Phys*, **33**(1991)117
7. D.H.Smith, *J.Lumin.*, **23** (1981) 209
8. E.Bringuier, *J.Appl.Phys.*, **66** (1989) 1314
9. K.A.Neyts and P.De Visschere, *J.Appl.Phys.*, **68** (1990) 4163
10. J.F.Wager and P.D.Keir, *Annual Review of Material Science*, **27** (1997) 223
11. E.Bringuier, *J.Appl.Phys.*, **75** (1994) 4291
12. E.Bringuier, *Appl.Phys.Lett.*, **60** (1992) 1256
13. P.D.Keir, W.M.Ang and J.F.Wager, *J.Appl.Phys.*, **78** (1995) 4668
14. K.W.C.Yang and S.J.T.Owen, *IEEE Trans.Electron Devices*, **ED-30** (1983) 452
15. N.E.Rigby, T.D.Thompson and J.W.Allen, *J.Phys.C: Solid State Phys.*, **21** (1988) 3295
16. T.D.Thompson and J.W.Allen, *J.Crystal Growth*, **101** (1990) 981
17. S.P.Shih, P.D.Keir and J.F.Wager, *J.Appl.Phys.*, **78** (1995) 5775
18. W.E.Howard, O.Sahni and P.M.Alt, *J.Appl.Phys.*, **53** (1982) 639

19. J.M.Jarem, and V.P.Singh, IEEE Trans.Electron Devices, **ED35** (1998) 1834
20. K.A.Neyts, IEEE Trans.Electron Devices, **38** (1991) 2604
21. A.Goldenblum, A.Opera and V.Bogatu, J.Appl.Phys.,**75** (1994) 5177
22. K.A.Neyts, D.Corlatan, P.D.Visschere and J.V.Bossche, J.Appl. Phys., **75** (1994) 5339
23. N.A.Vlasenko, A.I.Beletskii, Z.L.Denisova and Y.F.Kononets, Extended abstracts of the third international conference on the science and technology of display phosphors, Huntington Beach, (1997) 77
24. S.Kobayashi, J.F.Wager and A.Abu-Dayah, Proceedings of the 6<sup>th</sup> international conference on electroluminescence, Cinco Puntos, (1992) 234
25. K.Ohmi, K.Ishitani, S.Tanaka and H.Kobayashi, Appl.Phys.Lett., **67** (1995) 944
26. J.C.Hitt, P.D.Keir, J.F.Wager and S.S.Sun, J.Appl.Phys., **83** (1998)1141
27. E.Bringuier, Philos.Mag.B, (1996)
28. M.Beale, Philos.Mag.B, **68** (1993) 573
29. W.M.Ang, S.Pennathur, L.Pham, J.F.Wager and S.M.Goodnick, J.Appl.Phys., **77** (1995) 2719
30. D.Corlatan, K.Neyts, P.D.Visschere, J.V.den Bossche and B.Maximus, J.SID, **5** (1997) 131
31. B.A.Cleary, P.D.Keir, J.C.Hitt, T.K.Plant and J.F.Wager, Extended abstracts of the third international conference on the science and technology of display phosphors, Huntington Beach, (1997) 65
32. J.B.Peery,P.D.Keir, W.M.Ang and J.F.Wager , Extended abstracts of the third international conference on the science and technology of display phosphors, Huntington Beach, (1997) 69

33. D.A.Buchanan, M.V.Fischetti and D.J.DiMaria, Phys. Rev.B:Condens. Matter, **43** (1991)1471
34. A.A.Douglas, M.S.thesis, Oregon State University (1993)
35. A.Aguilera, V.P.Singh and D.C.Morton, IEEE Trans. Electron Devices, **41** (1994)1357
36. S.Bhaskaran, V.P.Singh and D.C.Morton, IEEE Trans. Electron Devices, **42** (1995) 1756
37. J.C.Hitt, M.S.Thesis, Oregon State University, (1998)
38. J.B.Peery, M.S.Thesis, Oregon State University, (1998)
39. S.S.Sun, E.Dickey, J.Kane and P.N.Yocom, Conference record '97 IDRC (1997) 301
40. U.Troppenz, B.Huttl, U.Storz, P.Kratzert, K.O.Velthaus, S.S.Sun and R.T.Tuenge, Extended abstracts of the fourth international conference on the science and technology of display phosphors (1998) 187
41. P.D.Keir, H.Le, R.L.Thuemler, J.Hitt and J.F.Wager, Appl. Phys. Lett. **69** (1996) 2421
42. T.Minami, T.Miyata, K.Kitamura, H.Nanto, and S.Takata, Jpn.J.Appl. Phys.,**27** (1988) 876
43. A.Fuh, R.P.Gallinger, P.Schuster, J.Adolph and O.Caporaletti, Thin Solid Films,**10** (1992) 202
44. Z.K.Kun, D.Leskell, P.R.Malmberg, J.Murphy and L.J.Sienkiewicz, J.Electron.Mater., **10** (1981) 287
45. S.Takata, T.Minami and T.Miyata, Thin Solid Films, **193** (1990) 481
46. Y.Nakanishi, Y.Fukuda, Y.Matanaka and G.Shimaoka, Appl.Surf.Sci., **48**(1991) 297
47. S.Okamoto, T.Kuki and T.Suzuki, Jpn.J.Appl.Phys.,**32** (1993) 1672
48. H.Kina, Y.Tamura, Y.Yamada and Y.Maruta Jpn.J.Appl.Phys.,**36** (1997) 150

49. R.M.German, *Sintering theory and practice*, New York, John Wiley & Sons (1996)
50. C.M.Wolfe, N.Holonyak and G.E.Stillman, *Physical properties of semiconductors*, Englewood Cliffs, NJ:Prentice Hall (1989)
51. Y.Tamura and H.Kozawaguchi, *Proceedings of the 4<sup>th</sup> international conference on electroluminescence*, Berlin, Springer-Verlag (1989)
52. J.C.Philips, *Bonds and bands in semiconductors*, New York, Academic Press (1973)
53. W.Lehmann, *J.Lumin*, **5** (1972) 87
54. S.M.Sze, *Physics of semiconductor devices*, New York, John Wiley & Sons (1981)
55. R.H.Bube, *Electrons in solids*, New York, Academic Press, (1981)
56. H.Lutch, *Surfaces and interfaces of solids*, Berlin, Springer-Verlag (1995)
57. W.A.Harrison, *Electronic structure and properties of solids*, New York, Dover (1989)
58. Cerac. Inc., *Vacuum deposition chemicals & evaporation materials*, third ed. (1988)
59. T.A.Oberacker and H.W.Schock, *J.Crystal Growth*, **159** (1996) 935
60. S.Tanaka, S.Ohshio, J.Nishiura, H.Kawakami, H.Yoshiyama, and H.Kobayashi, *Appl.Phys.Lett.*, **52** (1988) 2102
61. S.S.Sun, T.Nguyen, M.S.Bowen, J.Kane, P.N.Yocom., A.Naman, K.Jones, P.H.Holloway, D.R.Evans and W.M.Dennis, *J.SID*, **6** (1998) 61
62. C.N.King, *J.SID*, **4** (1996) 153
63. M.Kawata, and H.Uchiike *IEICE Trans. Electron.*, **E80-C** (1997) 1109
64. W.Lehmann, *J.Electrochem.Soc.*, **118** (1971)
65. S.Shionoya, *Phosphor handbook*, Boca Raton, CRC Press (1999) 231

# CHAPTER TWO

## Experimental Techniques and Characterization tools

### 2.1 Introduction

Any solid or liquid object with one of its dimensions very much less than that of the other two may be called a 'thin film' [1]. Thin film devices would typically be about 5 to 50  $\mu\text{m}$  thick in contrast to bulk devices, which are about 50 to 250  $\mu\text{m}$  thick [2]. If the growth is atom by atom or molecule by molecule it is called thin film and if the growth is grain by grain it is thick film. A wide variety of microstructures and consequently properties can be obtained by simply varying the deposition conditions during the growth of the film. Thin film properties are strongly dependent on the methods of deposition, the substrate materials, the substrate temperature, the rate of deposition and the background pressure. The application and the properties of the given material determine the most suitable technique for the preparation of thin films of that material.

The thin films prepared for the studies presented in this thesis were mainly deposited using electron beam evaporation and thermal evaporation techniques. The structural, optical and electrical properties of these films, bulk and nanophosphor samples were studied using different characterisation tools.

### 2.2 Thin film deposition Techniques

Generally any thin film deposition follows the sequential steps: a source material is converted into the vapour form (atomic/molecular/ionic species) from the condensed phase (solid or liquid), which is transported to the substrate and then it is allowed to condense on the substrate surface to form



the solid film [2]. Depending on how the atoms/molecules/ions/clusters of species are created for the condensation process, the deposition techniques are broadly classified into two categories, viz. physical methods and chemical methods.

Chemical bath deposition, chemical vapour deposition, and spray pyrolysis are examples of chemical method of thin film deposition. Thermal evaporation, e beam evaporation, rf and dc sputtering and pulsed laser deposition (PLD) are examples of physical methods of thin film preparation.

The following sections discuss the methodology and experimental set-up used in various thin film deposition techniques.

### **2.2.1 Thermal evaporation by resistive heating**

Thermal evaporation is the most widely used technique for the preparation of thin films of metals, alloys, and also many compounds, as it is very simple and convenient. Here the only requirement is to have a vacuum environment in which sufficient amount of heat is given to the evaporants to attain the vapour pressure necessary for the evaporation. The evaporated material is allowed to condense on a substrate kept at a suitable temperature.

When evaporation is made in vacuum, the evaporation temperature will be considerably lowered and the formation of the oxides and incorporation of impurities in the growing layer will be reduced. Evaporation is normally done at a pressure of  $10^{-5}$  Torr. At this pressure a straight line path for most of the emitted vapour atoms is ensured for a substrate to source distance of nearly 10 to 50 cm [3]. The characteristics and quality of the deposited film will depend on the substrate temperature, rate of deposition, ambient pressure, etc. and the uniformity of the film depends on the geometry of the evaporation source and its distance from the source. The deposition by

thermal evaporation is simple, convenient and is widely used. Excellent and detailed reviews on the know-how of the thermal evaporation have been discussed by Holland [4].

### 2.2.2 Electron-Beam Evaporation Method

The evaporation technique is useful for non-refractory materials that will vapourise at a reasonable temperature, less than  $1400^{\circ}\text{C}$  for thermal sources and less than  $2200^{\circ}\text{C}$  for electron-beam sources. Typically, evaporation can produce good film stoichiometry for elements and simple compounds. Specifically, the evaporation technique has difficulty producing good films of complex phosphors like rare earth oxysulphides because of the widely components of these compounds. On the other hand, the classical II-VI compounds form excellent films by evaporation [5].

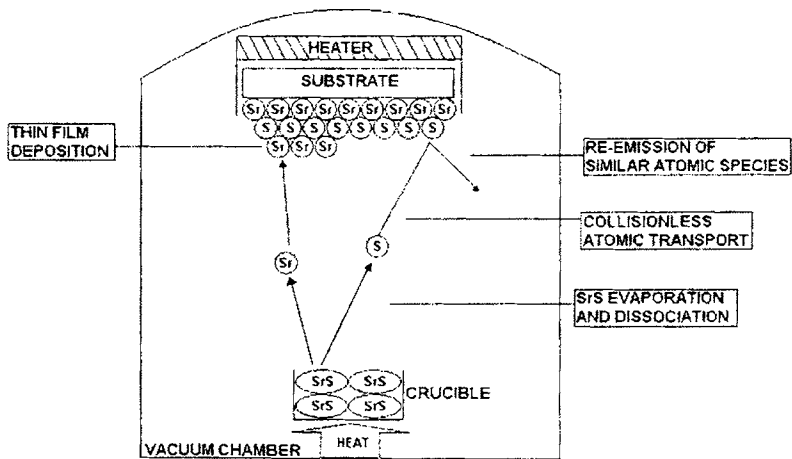


Figure 2.1 SrS evaporation kinetics

The kinetics of the evaporation, material transport and film condensation are shown in figure 2.1. The strength of the chemical bonding in these compounds are weak enough that the heat of evaporation is sufficient to largely dissociate the molecule. The individual atomic species are then transported to the substrate in a line of sight trajectory provided that the pressure level is low enough to permit collisionless transport. The atoms then recombine on the substrate to form II-VI compound. A feature of this recombination at the substrate is that it can be controlled to produce very stoichiometric films by adjusting the substrate temperature. The mechanism here is that the vapour pressure of the constituent atoms, for example Sr and S, is high enough for high substrate temperatures that neither Sr nor S atoms will adhere to other similar atoms. Thus film growth proceeds by formation of alternate layers of Sr and S atoms and stoichiometry is automatically achieved.

The simple resistive heating of an evaporation source suffers from the disadvantages of possible contamination from the support material and the limitations of input power, which make it difficult to evaporate high melting point materials.

-

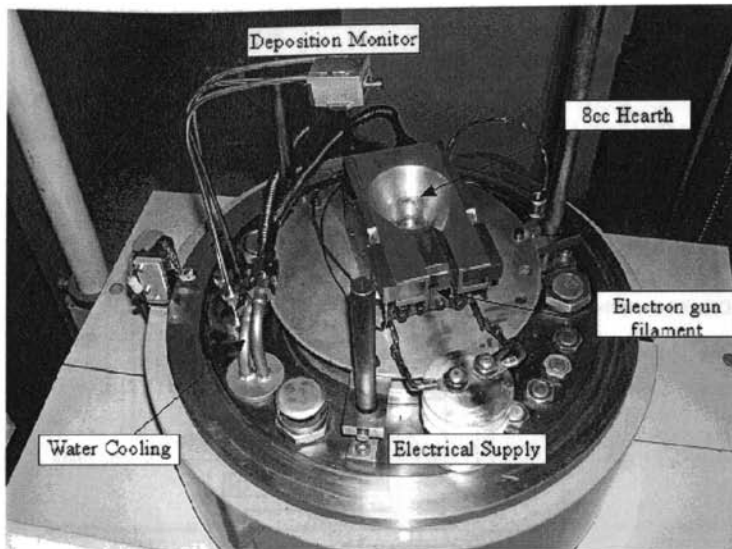


Figure 2.2 The top view of an electron beam gun fixed in a vacuum coating system

These drawbacks may be overcome by an efficient source of heating by electron bombardment of the material. In principle, this type of source is capable of evaporating any material at rates ranging from fractions of an angstrom to microns per second. Thermal decomposition and structural changes of some chemical compounds may occur because of the intense heat and energetic electron bombardment.

The electron beam gun (figure 2.2) fits in the vacuum chamber which consists of a W filament, anode, permanent magnet etc. It is operated by a high voltage power supply (3kW). When it is operated the W filament is heated by the low tension until it becomes incandescent and then emits electrons spontaneously and randomly. The anode plate then collects the electrons and forms them into a beam which is accelerated through the high voltage potential of 6kV.(figure 2.3).Magnetic fields created by a permanent magnet and the pole pieces and pole piece extensions deflect the beam

through  $270^\circ$  until it impacts on the evaporant in the crucible hearth which is at electrical ground potential.

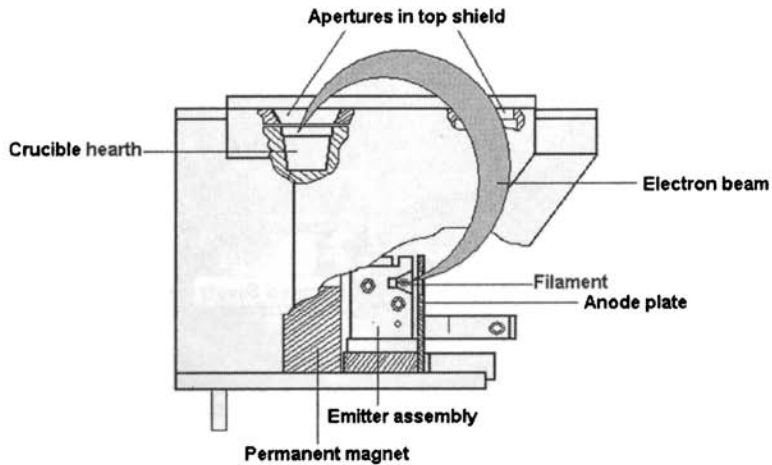


Figure 2.3 Principle of operation of electron beam gun.

A schematic diagram of the electron beam evaporation system is shown in figure 2.4

The combined force,  $F$ , on an electron in electric and magnetic fields known as Lorentz force is given by

$$F = F_E + F_B = q_e E + q_e (v \times B)$$

The second force is balanced by the centrifugal force of the electrons curving at radius  $r$ , that is

$$|q_e v \times B| = m |v^2| / r$$

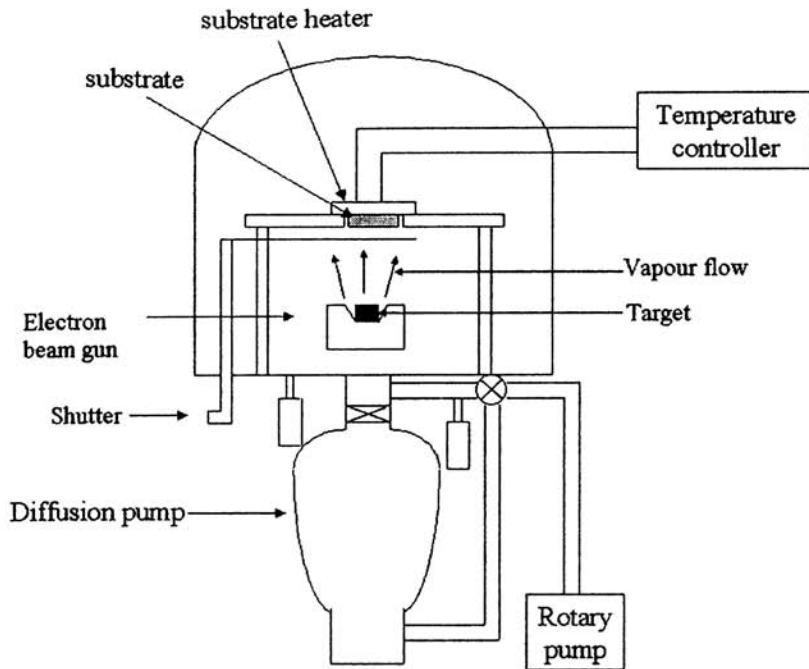


Figure 2.4 Vacuum system using electron beam evaporation

Thus the "cyclotron" or "Larmor" radius of an electron orbiting in a magnetic field is

$$r = m_e v_{\perp} / q_e |B|$$

Where  $v_{\perp}$  is the component of  $v$  perpendicular to  $B$ .

The electron beam instead of hitting a single point can be made to move in X and Y directions using a pair of horizontally and vertically deflecting sweep coils.

The source material is contained by a Cu hearth which is water-cooled to prevent its outgassing or melting. Cooling also prevents the hearth from alloying with molten source materials. Then the source material is evaporated from a crucible. A schematic representation of electron beam evaporation system is shown in figure 2.4

This evaporation technique done with narrow intense energy beam is subject to “macroparticle-spitting” problem. One mechanism of macroparticle ejection common to all vaporization methods and dominant for electron beams is the sudden evaporation of a nodule of a particular contaminant whose vapour pressure is much higher than that of the source material. The volatile contaminant nodule which ejects the macroparticle may be an inclusion in the solid source material, a gaspocket trapped within sintered material, or a slag accumulating on the surface of molten metal by reaction background gases with the metal or by precipitation of bulk contaminants upon melting the metal.

Although electron-beam evaporation is a thermal process, so that the vapour atoms leave the surface with only thermal energy of  $\sim 0.2\text{eV}$ , several kinds of non thermal energy still arrive at the film surface. One is x-rays generated by electron-beam impact on the source material. But they are not hard enough to penetrate the vacuum chamber wall or window to become a hazard to the operator [6]. The second form of non thermal energy accompanying electron-beam evaporation is positive ions generated above the source by impact of the incoming beam upon the outgoing vapour. Sometimes a gaseous source species is introduced into the evaporation chamber for the purpose of forming a compound film by reaction with the evaporating species.

## **2.3 Characterisation tools**

The optimisation of the preparation conditions is the main task in order to get device quality phosphor material. This has to be carried out on the basis of detailed study on structural, compositional, morphological, optical and electrical properties of the film and bulk phosphors obtained at different growth conditions. In the following sections the techniques used for the film characterizations are discussed briefly.

### **2.3.1 Thin film thickness**

Thickness plays an important role in the film properties unlike a bulk material. Reproducible properties are achieved only when the film thickness and the deposition parameters are kept constant. Film thickness may be measured either by in-situ monitoring of the rate of deposition or after the film deposition. The thicknesses of the thin films prepared for the work presented in this thesis were measured by a stylus profiler (Dektak 6M).

The stylus profiler takes measurements electromechanically by moving the sample beneath a diamond tipped stylus. The high precision stage of this equipment moves the sample according to a user defined scan length, speed and stylus force. The stylus is mechanically coupled to the core of a linear variable differential transformer (LVDT). The stylus moves over the sample surface. Surface variations cause the stylus to be translated vertically. Electrical signals corresponding to the stylus movement are produced as the core position of the LVDT changes. The LVDT scales an ac reference signal proportional to the position change, which in turn is conditioned and converted to a digital format through a high precision, integrating, analog-to-digital converter [7]. The film whose thickness has to be measured is



deposited by masking a small region which creates a step on the sample surface. The thickness of the sample can be measured accurately by measuring the vertical motion of the stylus over the step.

### **2.3.2 X-ray diffraction studies**

Electrical and optical properties of a substance are influenced by their crystallographic nature. X-ray diffraction (XRD) studies were carried out to understand the crystallographic properties of the phosphors prepared. A given substance always produces a characteristic x-ray diffraction pattern whether that substance is present in the pure state or as one constituent of a mixture of substances. This fact is the basis for the diffraction method of chemical analysis. The particular advantage of x-ray diffraction analysis is that it discloses the presence of a substance and not in terms of its constituent chemical elements. Diffraction analysis is useful whenever it is necessary to know the state of chemical combination of the elements involved or the particular phase in which they are present. Compared with ordinary chemical analysis the diffraction method has the advantage that it is much faster, requires only very small sample and is non destructive [8,9].

The basic law involved in the diffraction method of structural analysis is the Bragg's law. When monochromatic x-rays impinge upon the atoms in a crystal lattice, each atom acts as a source of scattering. The crystal lattice acts as series of parallel reflecting planes. The intensity of the reflected beam at certain angles will be maximum when the path difference between two reflected waves from two different planes is an integral multiple of  $\lambda$ . This condition is called Bragg's law and is given by the relation,

$$2d\sin\theta = n\lambda$$

where  $n$  is the order of diffraction,  $\lambda$  is the wavelength of the x-rays,  $d$  is the spacing between consecutive parallel planes and  $\theta$  is the glancing angle (or the complement of the angle of incidence) [10].

X-ray diffraction studies gives a whole range of information about the crystal structure, orientation, average crystalline size and stress in the films. Experimentally obtained diffraction patterns of the sample are compared with the standard powder diffraction files published by the Joint Committee on Powder Diffraction Standards (JCPDS).

The average grain size of the film can be calculated using the Scherrer's formula [8],

$$d = \frac{0.9\lambda}{\beta \cos\theta}$$

where,  $\lambda$  is the wavelength of the x-ray and  $\beta$  is the full width at half maximum intensity in radians.

The lattice parameter values for different crystallographic systems can be calculated from the following equations using the (hkl) parameters and the interplanar spacing  $d$ .

Cubic system, 
$$\frac{1}{d^2} = \frac{h^2 + k^2 + l^2}{a^2}$$

Tetragonal system, 
$$\frac{1}{d^2} = \frac{h^2 + k^2}{a^2} + \frac{l^2}{c^2}$$

Hexagonal system, 
$$\frac{1}{d^2} = \frac{4}{3} \left( \frac{h^2 + hk + k^2}{a^2} \right) + \frac{l^2}{c^2}$$

X-ray diffraction measurements of the films in the present studies were done using Rigaku automated x-ray diffractometer. The filtered copper  $K\alpha$  ( $\lambda=1.5418\text{\AA}$ ) radiation was used for recording the diffraction pattern.

### **2.3.3 Atomic Force Microscopy (AFM)**

Following the invention of the scanning tunnelling microscope (STM), a number of new scanning probe microscopes (SPM) has been developed that use the key components of the STM. One of the most important SPM is the atomic force microscope (AFM) [11,12]. In atomic force microscopy a tip, integrated to the end of a spring cantilever, is brought within the interatomic separations of a surface, such that the atoms of the tip and the surface are influenced by interatomic potentials. As the tip is rastered across the surface, it bounces up and down on the contours of the surface. By measuring the displacement of the tip (*i.e.* the deflection of the cantilever), one can theoretically map out the surface topography with atomic resolution. The first generation AFM measured cantilever deflections using a piggy-backed STM. Later instruments used more practical optical techniques. The AFM is essentially identical in concept to the scanning profilometer, except that the deflection-sensitivity and resolution are improved by several orders of magnitude. There are a large number of applications for the AFM, including biological systems, polymers, and a host of insulator and semiconductor materials.

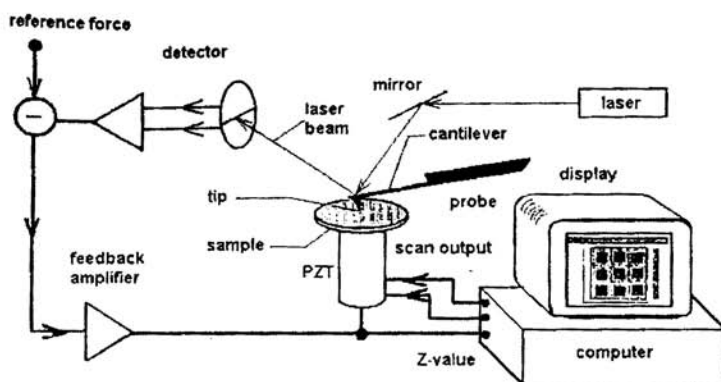


Figure 2.5 The essential elements of an AFM

An AFM images a surface in a manner analogous to the gramophone stylus sensing the grooves of gramophone disk. The essential elements of an AFM are shown in the figure 2.5. The tip is attached to a cantilever type spring. As the tip and sample interact, forces act on the tip and cause the cantilever (spring) to deflect. The cantilever position is monitored by a position detector. The output of the detector is connected to a feedback controller that regulates the force between the sample and the tip by moving the sample up or down. The sample is moved by a PZT scanning actuator. The cantilever must be soft enough to deflect a measurable amount without damaging the surface features of the sample. The amount of deflection is proportional to the force acting on the tip.

$$F_{spring} = -k \cdot \Delta Z$$

where  $F$  is the force on the sample,  $k$  is the spring constant of the cantilever, and,  $\Delta Z$  is the deflection of the cantilever.

Various modes of AFM measurements include contact mode, dynamic force mode, phase mode. Friction force microscope, magnetic force microscope, surface potential microscope, etc are scanning probe microscopes with slight variation in the working principles from that described above.

### 2.3.4 Transmission spectroscopy

Intrinsic optical absorption of a single photon across the band gap is the dominant optical absorption process in a semiconductor. When the energy of the incident photon ( $h\nu$ ) is larger than the band gap energy the excitation of electrons from the valence band to the empty states of the conduction band occurs. The light passing through the material is then absorbed and the number of electron hole pairs generated depends on the number of incident photons  $S_0(\nu)$  (per unit area, unit time and unit energy). The frequency  $\nu$  is related to the wavelength  $\lambda$  by the relation,  $\lambda = c/\nu$ , where  $c$  is the velocity of light. The photon flux  $S(x,\nu)$  decreases exponentially inside the crystal according to the relation [13],

$$S(x,\nu) = S_0(\nu) \exp(-\alpha x)$$

where, the absorption coefficient  $\alpha$ , ( $\alpha(\nu) = 4\pi k\nu/c$ ) is determined by the absorption process in semiconductors and  $k$  is the extinction coefficient.

For the parabolic band structure, the relation between the absorption coefficient ( $\alpha$ ) and the band gap of the material is given by [13],

$$\alpha = \frac{A}{h\nu} (h\nu - E_g)^r$$

where,  $r = 1/2$  for allowed direct transitions,  $r = 2$  for allowed indirect transitions,  $r = 3$  for forbidden indirect transitions and  $r = 3/2$  for forbidden direct transitions.  $A$  is the parameter which depends on the transition probability. The absorption coefficient can be deduced from the absorption or transmission spectra using the relation,

$$I = I_0 e^{-\alpha t}$$

where,  $I$  is the transmitted intensity and  $I_0$  is the incident intensity of the light and  $t$  is the thickness of the film. In the case of direct transition, from equation  $(\alpha h\nu)^2$  will show a linear dependence on the photon energy  $(h\nu)$ . In the case of direct bandgap semiconductor a plot of  $(\alpha h\nu)^2$  against  $h\nu$  will be a straight line and the intercept on energy axis at  $(\alpha h\nu)^2$  equal to zero will give the band gap energy.

The transmissions of the thin films were recorded using Hitachi uv-vis-nir 330 spectrophotometer and Jasco V500 spectrophotometer.

### **2.3.5 Diffuse reflectance spectroscopy**

The measurement of radiation reflected from a surface constitutes the area of spectroscopy known as diffuse reflectance spectroscopy (DRS). Diffuse reflectance spectrometry concerns one of the two components of reflected radiation from an irradiated sample, namely specular reflected radiation,  $R_s$  and diffusely reflected radiation,  $R_d$ . The former component is due to the reflection at the surface of single crystallites while the latter arises from the radiation penetrating into the interior of the solid and re-emerging to the surface after being scattered numerous times. These spectra can exhibit both absorbance and reflectance features due to contributions from transmission,

internal and specular reflectance components as well as scattering phenomena in the collected radiation.

Based on the optical properties of the sample, several models have been proposed to describe the diffuse reflectance phenomena. The Kubelka-Munk model put forward in 1931 is widely used and accepted in diffuse reflectance infrared spectrometry.

The intensity of the reflected light depends on the scattering coefficient  $s$  and the absorption coefficient  $k$ . The reflectance data can be converted to absorbance by Kubelka-Munk equation [14,15].

Kubelka-Munk equation is as

$$\text{Log} [(1 - r_\infty)^2 / 2 r_\infty] = \text{Log } k - \text{Log } s$$

Where  $r_\infty = R_\infty(\text{sample}) / R_\infty(\text{standard})$ . Here the standard used is MgO.  $R_\infty(\text{standard})$  is taken as unity.  $R_\infty(\text{sample})$  is the diffuse reflectance of the sample ( $R = I_{\text{san}} / I_{\text{ref}}$ ).

$$(1 - R)^2 / 2 R = k/s$$

The band gap is estimated from the plot of  $\{(k/s) \cdot h\nu\}^2$  versus  $h\nu$ , and extrapolating the graph to the X axis.

### 2.3.6 Photoluminescence (PL) measurements

Two types of luminescence spectra can be distinguished: excitation and emission. In the case of an excitation spectrum the wavelength of the

exciting light is varied and the intensity of the emitted light at a fixed emission wavelength is measured as a function of the excitation wavelength. The excitation spectrum gives information on the position of excited states just as the absorption spectrum does, except that the former reveals only the absorption bands that result in the emission of light. The observed differences between the absorption and excitation spectra can yield useful information. An emission spectrum provides information on the spectral distribution of the light emitted by a sample. The time resolved PL measurements are a powerful tool for the determination of the radiative efficiency. The radiative efficiency specifies the fraction of excited states, which de-excite by emitting photons. The PL studies give information on the effect of doping in phosphors. Luminescence decay indicates the defect density in the film sample by comparing the normalized area under the decay curve of the powder samples when non-radiative de-excitation occurs [16].

The emission and excitation spectra for the powder and thin film samples are recorded using Fluoromax -3 spectrofluorimeter. The FluoroMax-3 is a spectrofluorimeter from JY-Horiba that is applicable to fluorescent intensity measurements. The fluorimeter follows a classical configuration with a Xenon arc lamp, excitation and emission monochromators, a photomultiplier tube (PMT) for detection and a reference photodiode. The Xenon lamp supplies a wide range of excitation light but to perform high resolution fluorescence measurements discrete wavelengths of light must be employed. Wavelength selection is achieved by the optical gratings of the monochromators which diffract incident light, dispersing it into its constituent wavelength components. In addition, adjustable 'slits' form the entrance and exits of monochromators and these components further resolve light wavelengths. On the excitation monochromator the slits control the bandpass (range) of light that is incident on the sample whereas the slits of



the emission monochromator determine the intensity of the emitted fluorescence recorded by the PMT. Finally, the reference photodiode is employed to correct for variations in the emission intensity of the Xenon lamp that occur at different wavelengths. As such, the FluoroMax-3 is a serious piece of equipment capable of performing high-resolution and sensitive fluorescence measurements. Further, provision for sample temperature control and stirring mean that this fluorimeter can also be used for cell biological applications in addition to basic solution studies.

### **2.3.7 CIE color Coordinates**

In 1931, the commission Internationale de l'Eclairage (CIE) established an international standard for quantifying all visible colors, known as CIE color coordinates. The CIE has defined a system that classifies color according to the HVS (the human visual system). Using this system we can specify any color in terms of its CIE coordinates. The CIE system works by weighting the SPD (spectral power density) of an object in terms of three-color matching functions. These functions are the sensitivities of a standard observer to light of different wavelengths. The weighting is performed over the visual spectrum, from around 360nm to 830nm in set intervals. However, the illuminant, and lighting and viewing geometry are carefully defined, since these all affect the appearance of a particular color. This process produces three CIE tri-stimulus values, XYZ, which are the building blocks from which many color measurements are made.

Any color can be described as a mixture of three primary colors or "Tristimuli", typically RGB for CRT based systems (TV, computer) or XYZ (fundamental measurements). The amounts of each stimulus define the color.

The CIE coordinates are obtained by computing the three CIE tristimulus values, X, Y and Z and subsequently computing the CIE coordinates x and y from these values. The CIE tristimulus values are obtained by integrating the product of the spectrum of the light source  $P(\lambda)$ , and CIE color matching functions,  $x_\lambda(\lambda)$ ,  $y_\lambda(\lambda)$  and  $z_\lambda(\lambda)$  as shown in figure 2.6 [17].

Since the spectra are measured as discrete values, integration is replaced by sum given as,

$$X = \Delta\lambda \sum x_\lambda(\lambda) P_\lambda(\lambda)$$

$$Y = \Delta\lambda \sum y_\lambda(\lambda) P_\lambda(\lambda)$$

$$Z = \Delta\lambda \sum z_\lambda(\lambda) P_\lambda(\lambda)$$

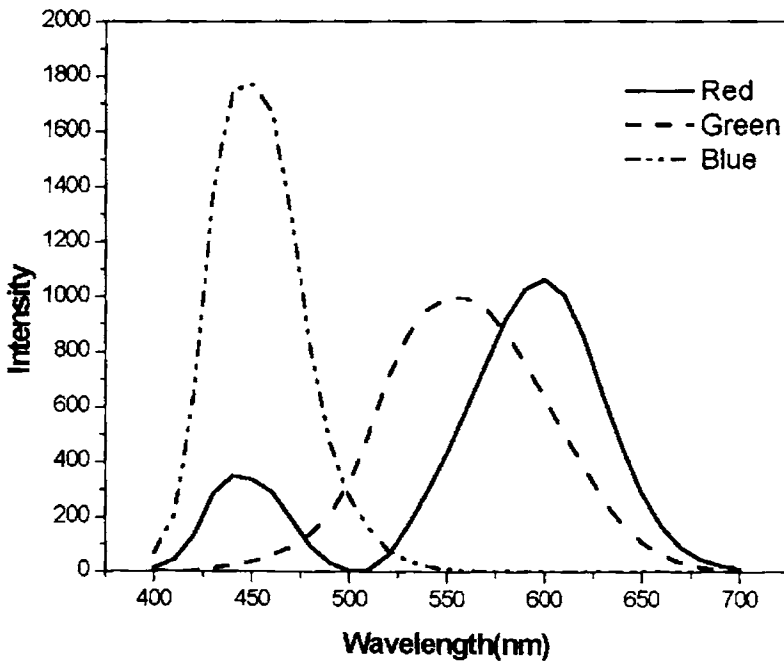


Figure 2.6. The CIE color matching function for CIE 1931 standard observer.

Where  $\Delta\lambda$  is the interval between the points. The CIE is calculated from the above values using the equations:

$$x = X/(X+Y+Z)$$

$$y = Y/(X+Y+Z)$$

$$z = Z/(X+Y+Z)$$

However, because,

$x + y + z = 1$ ; only two of the three CIE color coordinates are independent. Hence only  $x$  and  $y$  values are reported. Plotting of the CIE  $y$  color coordinates versus the CIE  $x$  color coordinate over the visual range of light leads to a horseshoe shaped diagram known as the CIE chromaticity diagram represented in figure 2.7.

The dot at the center represents white light. CIE coordinates corresponding to red, green, blue and white light is given in table 2.1. When the CIE coordinate of a color are specified, the dominant wavelength of the color is the intersection of the line connecting these CIE coordinates and those of white light with the upper arc of the diagram. Further, when the light emission from phosphors of two colors is mixed, the range of colors that it is possible to produce by mixing these colors is given by the line that ties the CIE coordinates of these two colors together [18].

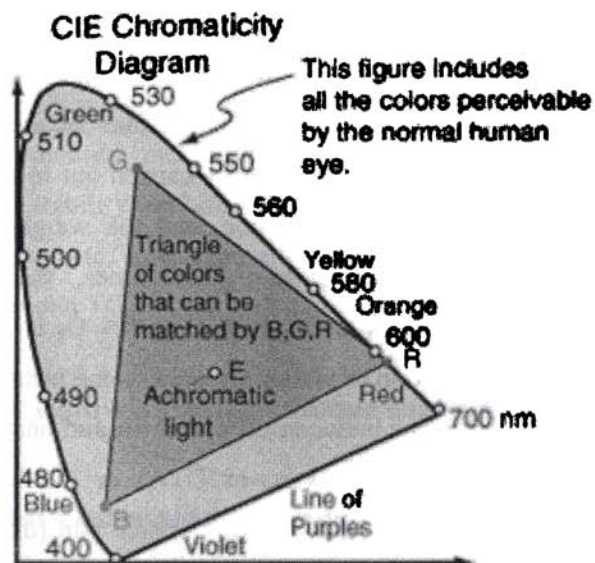


Figure 2.7 The CIE chromaticity diagram.

The CIE color coordinates are most useful for the optical characterization of phosphors as guidelines to gauge the quantity of the chromaticity available from a full color display. The CIE coordinates are thus a powerful concept, which represent an entire luminescent spectrum by two numbers.

Table 2.1. CIE coordinates for phosphors in tri chromatic system

	Red	Green	Blue	White
x	0.65	0.3	0.15	0.33
y	0.35	0.6	0.1	0.33

### 2.3.8 Thermogravimetric Analysis (TGA)

Thermogravimetric analysis (TGA) is an analytical technique used to determine a material's thermal stability and its fraction of volatile components by monitoring the weight change that occurs as the specimen is heated. The measurement is normally carried out in air or in an inert atmosphere, such as Helium or Argon, and the weight is recorded as a function of increasing temperature. Sometimes, the measurement is performed in a lean oxygen atmosphere (1 to 5% O<sub>2</sub> in N<sub>2</sub> or He) to slow down oxidation. In addition to weight changes, some instruments also record the temperature difference between the specimen and one or more reference pans (differential thermal analysis, or DTA) or the heat flow into the specimen pan compared to that of the reference pan (differential scanning calorimetry, or DSC). The latter can be used to monitor the energy released or absorbed via chemical reactions during the heating process. In the particular case of carbon nanotubes, the weight change in an air atmosphere is typically a superposition of the weight loss due to oxidation of carbon into gaseous carbon dioxide and the weight gain due to oxidation of residual metal catalyst into solid oxides.

TGA instruments can be divided into two general types: vertical and horizontal balance. Vertical balance instruments have a specimen pan hanging from the balance (TA Instruments, etc) or located above the balance on a sample stem (Netzsch). It is necessary to calibrate these instruments in order to compensate for buoyancy effects due to the variation in the density of the purge gas with temperature, as well as the type of gas. Vertical balance instruments generally do not have reference pan and are incapable of true DTA or DSC measurements (Netzsch being an exception). Horizontal

balance instruments (TA, Perkin Elmer, etc.) normally have two pans (sample and reference) and can perform DTA and DSC measurements. They are considered free from buoyancy effects, but require calibration to compensate for differential thermal expansion of balance arms. Applications of the TG/DTA instrument are compositional analysis, decomposition temperature, oil volatility measurements, flammability studies, heat of transition, thermal stability analysis, oxidative stability analysis, transition temperature detection etc. In the present study TGA was performed using Perkin Elmer, Diamond TG/DTA

### **2.3.9 Inductively Coupled Plasma- Atomic Emission Spectroscopy**

Inductively Coupled Plasma-Atomic Emission Spectroscopy (ICP-AES) is one of several techniques available in analytical atomic spectroscopy for compositional analysis. ICP-AES utilizes a plasma as the atomization and excitation source. A plasma is an electrically neutral, highly ionized gas that consists of ions, electrons, and atoms. The energy that maintains an analytical plasma is derived from an electric or magnetic field. Most analytical plasmas operate with pure argon or helium, which makes combustion impossible. Plasmas are characterized by their temperature, as well as their electron and ion densities. Analytical plasmas typically range in temperature from 600 to 8,000 K. As a comparison, the temperature of the sun's interior is millions of degrees, while its surface temperature is approximately 10,000 K.

The steps involved in determining the elemental content of an aqueous phase sample by ICPAES are: [19]

1. Sample Preparation: Some samples require special preparation steps including treatment with acids, heating, and microwave digestion.

2. Nebulization: Liquid converted to aerosol.
3. Atomization: Gas phase bonds are broken, and only atoms are present. Plasma temperature and inert chemical environment are important at this stage.
4. Desolvation/Volatization: Water is driven off, and remaining solid and liquid portions are converted to gases.
5. Excitation/Emission: Atoms gain energy from collisions and emit light of a characteristic wavelength.
6. Separation/Detection: A grating disperses light that is quantitatively measured.

The atomic spectrum emitted by a sample is used to determine its elemental composition in this instrument. The wavelength at which emission occurs identifies the element, while the intensity of the emitted radiation quantifies its concentration. Thermo Electron IRIS INTREPID II XSP DUO was used for the determination of elemental composition in the phosphors.

### **2.3.10 Electron Paramagnetic Resonance (EPR) spectroscopy**

Electron Paramagnetic Resonance (EPR) spectroscopy, often called Electron Spin resonance (ESR) spectroscopy is based on the absorption of microwave radiation by an unpaired electron when it is exposed to a strong magnetic field. Species that contain unpaired electrons (namely free radicals, odd-electron molecules, transition metal complexes, rare earth ions, etc.) can therefore be detected by EPR. Qualitative and quantitative estimation of compounds can be made by EPR. It is widely used as a non-destructive technique in determining the structure of transition metal complexes and organic free radicals.

Zavoisky discovered electron paramagnetic resonance (EPR) which is also called as electron spin resonance (ESR) in 1944 in USSR. He observed the first EPR spectrum in  $\text{CuCl}_2 \cdot 2\text{H}_2\text{O}$  in 1945. The EPR technique is an extension of Stern-Gerlach experiment.

When a sample is subjected to static magnetic field, the interaction between the magnetic moment of the electron and applied magnetic field splits the Zeeman energy levels. Application of microwave radiation perpendicular to the magnetic field causes excitation of electrons from one level to the other. The resulting absorption of the microwave is modulated to record first derivative of the absorption. Conventionally EPR spectra are recorded as first derivative rather than absorption to improve the resolution. In fact, second derivatives are also recorded when necessary.

The electron magnetic moment is coupled with the nuclei that it is associated with. Most nuclei and their isotopes have a magnetic moments characteristic of them. The electron magnetic moment interacts with the nuclear magnetic moment. This results in further splitting of Zeeman energy levels which appears as multiple lines in the spectrum.

When the system has more than one unpaired electron, the energy levels are split even in the absence of applied magnetic field due to the interaction between the electrons. It is known as the zero-field splitting. The number of splitting of the energy levels is given by  $(2S+1)$ , where  $S$  is the total spin of the electron. The nuclear hyperfine splitting is given by  $(2I+1)$  where  $I$  is the nuclear spin quantum number [20-22].

In general, EPR spectroscopy deals with the paramagnetic compounds to study the magnetic properties of the materials. EPR spectrometer generally operates at a constant frequency while magnetic field is swept. Many models



of EPR instruments are built to operate at several frequencies ranging from 250 MHz to 100 GHz. Popular models operate at 9.5 and 35 GHz called as X- and Q-band frequencies (the names X and Q are historical whose origin comes from the application of microwaves to military). At these frequencies, the energy of the radiation is 0.3 and 1.0 wavenumbers. This allows one to study the transitions of the order of  $0.00001 \text{ cm}^{-1}$  which makes this technique extremely powerful in studying weak interactions. Hyperfine couplings, intermolecular interactions like exchange coupling, etc. reveal very useful information about the structure and the magnetic properties of the molecule. The technique is very sensitive and it is possible to detect sub-micromolar quantities of paramagnetic species.

Varian E-112 spectrometer generates microwave from klystron, suitably attenuates and allows it to pass through a circulator to a reflection type cavity (figure 2.8). The change in the microwave flux in the cavity during resonance absorption is detected using a crystal detector. The microwave frequency is detected using a crystal detector. The microwave frequency is modulated with a 100 kHz field and the output from the crystal detector is phase detected and amplified, thus providing a first derivative of absorption as a function of magnetic field.

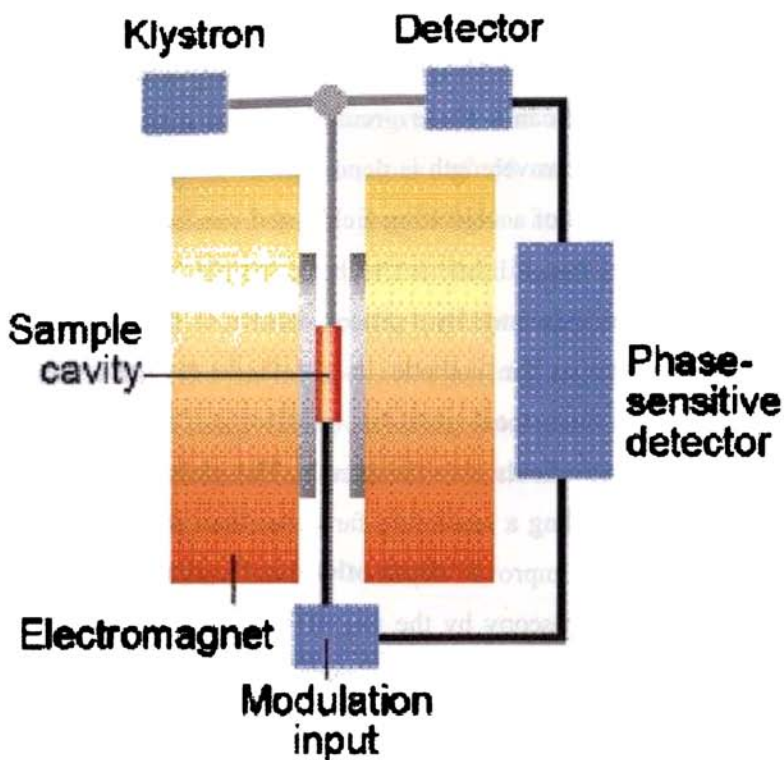


Figure 2.8 Schematic diagram of an EPR spectrometer

### 2.3.11 Transmission Electron Microscopy (TEM) .

Transmission electron microscopy (TEM) is an imaging technique whereby a beam of electrons is focused onto a specimen causing an enlarged version to appear on a fluorescent screen or layer of photographic film or to be detected by a CCD camera. The first practical transmission electron microscope was built by Albert Prebus and James Hillier at the university of Toronto in 1938 using concepts developed earlier by Max Knoll and Ernst Ruska.

Like all matter, electrons have both wave and particle properties (as theorized by Louis-Victor de Broglie), and their wave-like properties mean that a beam of electrons can in some circumstances be made to behave like a beam of radiation. The wavelength is dependent on their energy, and so can be tuned by adjustment of accelerating fields, and can be much smaller than that of light, yet they can still interact with the sample due to their electrical charge. Electrons are generated by a process known as thermionic discharge in the same manner as the cathode in a cathode ray tube, or by field emission; they are then accelerated by an electric field and focused by electrical and magnetic fields onto the sample. The electrons can be focused onto the sample providing a resolution far better than is possible with light microscopes, and with improved depth of vision. Details of a sample can be enhanced in light microscopy by the use of stains; similarly with electron microscopy, compounds of heavy metals such as osmium or lead or uranium can be used to selectively deposit heavy atoms in the sample and enhance structural detail, the dense nuclei of the heavy atoms scatter the electrons out of the optical path. The electrons that remain in the beam can be detected using a photographic film, or fluorescent screen among other technologies. So areas where electrons are scattered appear dark on the screen, or on a positive image[11].

In the most powerful diffraction contrast TEM instruments, crystal structure can also be investigated by High Resolution Transmission Electron Microscopy (HRTEM), also known as phase contrast imaging as the images are formed due to differences in phase of electron waves scattered through a thin specimen.

Resolution of the HRTEM is limited by spherical and chromatic aberration, but a new generation of aberration correctors has been able to overcome

spherical aberration. Software correction of spherical aberration has allowed the production of images with sufficient resolution to show carbon atoms in diamond separated by only 0.89 angstroms and atoms in silicon at 0.78 angstroms (78 pm) at magnifications of 50 million times. Improved resolution has also allowed the imaging of lighter atoms that scatter electrons less efficiently — lithium atoms have been imaged in lithium battery materials. The ability to determine the positions of atoms within materials has made the HRTEM an indispensable tool for nanotechnology research and development in many fields, including heterogeneous catalysis and the development of semiconductor devices for electronics and photonics.

### **2.3.12 Resistivity by two probe method**

The resistivity of the bulk sample can be determined by the two-probe method. Evaporated indium layers or high conducting silver paste is used as the electrodes on two sides of the pelletised sample. The current voltage measurements are carried out using a Keithley's source measure unit (Model SMU 236). The resistivity ( $\rho$ ) of the sample is calculated applying ohm's law, by the relation  $\rho = RA/L$ , where R is the resistance given by the slope of the current – voltage characteristic curve, A is the cross sectional area and L is the thickness of the pellet.

### **2.3.13 Luminance-Voltage (L-V) Characterization**

The driving waveform used to operate an ACTFEL device can be a sine wave, triangular wave or bipolar trapezoidal voltage waveform. The standard bipolar waveform used for most of the electrical characterization techniques consists of a 1 KHz sequence of bipolar trapezoidal pulses with rise and fall times of 5  $\mu$ s and a pulse width of 30  $\mu$ s. It is to be noted that the polarity of

the applied voltage pulse is defined with respect to the top electrode (i.e. the electrode farthest away the substrate). The voltage values should be indicated in zero-to-peak values, rather than in rms values, since luminance depends on the peak voltage value. The pulse width,  $\tau$ , is defined by the full width at the half maximum of the actual (deformed) pulse drive waveform applied to an EL device, and the rise time  $t_r$  and the fall time  $t_f$  are defined by the time period corresponding to 10%-to-90% value and 90%-to-10% value, respectively, of the actual voltage. The recommended values for practical applications are  $\tau = 40 \mu\text{s}$ ,  $t_r \leq 8 \mu\text{s}$  and  $t_f \leq 8 \mu\text{s}$  (figure 2.9).

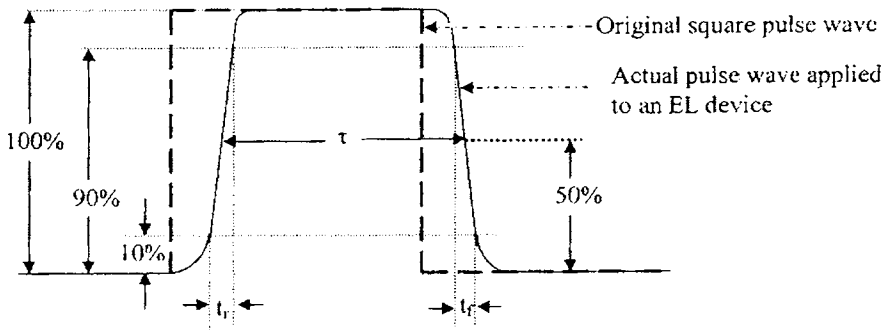


Figure 2.9. Driving waveform of an ACTFEL device

The most commonly used techniques to compare and contrast ACTFEL devices from an industrial viewpoint are measurements that explore its light output, the power required to generate that light and the color of light emitted. The optical response of an ACTFEL device to an electrical stimulus is critical in specifying the display performance.

Several important ACTFEL parameters, namely, the threshold voltage ( $V_{th}$ ) and luminance at  $V_{th} + 40$  V ( $L_{40}$ ) can be determined from luminance versus voltage (L-V) measurements. The method requires a variable ac voltage supply (typically 0-300 V) and a spectrometer to measure the luminance as a function of the applied voltage. Luminance is measured varying the amplitude of the applied waveform. Once the data is collected, plotting voltages on the x-axis and the corresponding luminances on the y-axis gives the L-V curve. A typical L-V plot is shown in figure 2.10. This gives the luminous intensity output in a direction normal to the emitting surface, and is generally reported in either foot-Lamberts (ft-L) or candelas per square meter ( $cd/m^2$ ) [ $1 \text{ ft-L} = 3.426 \text{ cd/m}^2$ ].

The threshold voltage is typically defined to be the voltage where a luminance of  $1 \text{ cd/m}^2$  is achieved. At this external voltage, the field inside the phosphor is high enough to cause electrons to excite the luminescent centers and generate light. As the voltage increases above threshold, the phosphor electric field increases proportionally, as does the electron energy distribution. Consequently, luminance sharply increases with voltage until the phosphor brightness saturates or until the phosphor layer experiences dielectric breakdown. The significance of the parameter  $L_{40}$  is that most ACTFEL displays are driven at 40 V above threshold, which is the modulation voltage. When comparing  $L_{40}$  values, it is important to consider both the threshold voltage and the frequency at which the device was driven.  $L_{40}$  increases almost linearly with both phosphor thickness (i.e.  $V_{th}$ ) and frequency. As thickness increases, there are more luminescent centers that electrons can excite; and when frequency increases, the number of passes that electrons make across the phosphor layer increases.

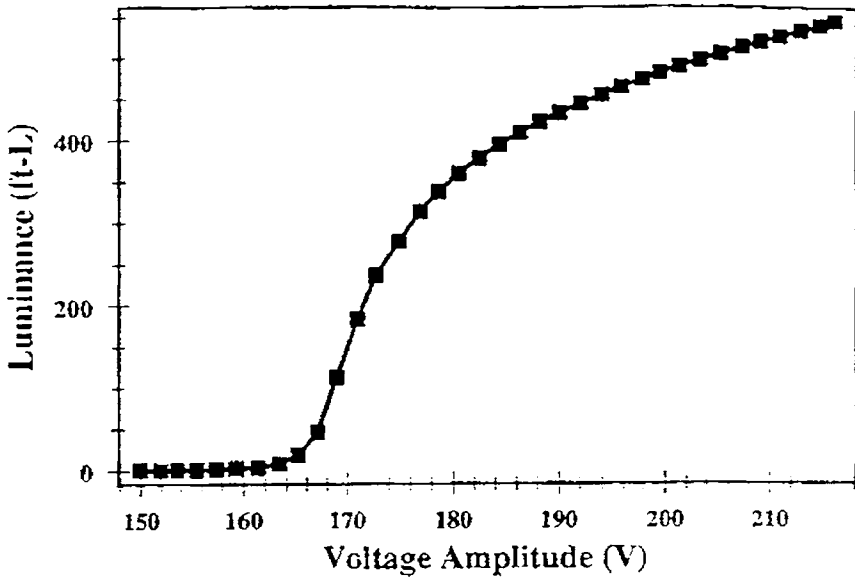


Figure 2.10. A typical luminance-voltage (L-V) curve

The L-V measurement is very sensitive to the nature of the driving waveform, driving voltage and its frequency. The measured luminance depends to some degree on the rise time, fall time and pulse width when bipolar trapezoidal waveforms are used to generate L-V data. The measured luminance at a fixed voltage increases quite noticeably with increasing frequency. This is because at higher frequencies, more pulses are applied to the ACTFEL device per unit time, hence, the luminescent impurities are excited more often. Unfortunately, there is a point of diminishing returns with increasing frequency where the luminance either saturates or decreases at a certain frequency. This effect has to do with both device heating and the de-excitation time of the luminescent impurities. Additionally, when the period of the driving waveform is of the same order as the characteristic decay time of the luminescent impurity, there may be little or no increase in

luminance with increasing frequency because many luminescent impurities may already be excited when the following pulse arrives. Essentially, the fraction of time per second that the driving waveform spends above the turn-on voltage determines the relative luminance of the device.

Besides the chemical composition, the thickness of the phosphor layer affects the observed luminance of the ACTFEL device. As the phosphor layer gets thicker (given a fixed doping concentration), a greater number of luminescent impurities are incorporated into the phosphor layer, and the carriers have a greater probability of impact excitation. Therefore, with all else being equal, ACTFEL devices with thicker phosphor layers will exhibit greater luminance than thinner devices.

The insulators affect the luminance characteristics of an ACTFEL device mainly through their effect on the voltage distribution through the device. An increase of insulator capacitance with respect to a fixed phosphor capacitance results in a greater percentage of the applied voltage being dropped across the phosphor layer, which leads to a lower threshold voltage. The two methods of increasing the insulator capacitance are to either decrease the thickness of the insulator layers or use an insulating material with larger dielectric constant.

The doping level of the luminescent impurity also is critical in determining the L-V characteristics of an ACTFEL device. At low dopant concentrations ( $\leq 1\%$  for most phosphor materials), the observed luminance increases monotonically with increasing luminescent impurity concentration. Then, an optimum luminance is achieved, and the luminance declines with increasing luminescent impurity concentration above this doping level. This decline is



due to the disruption of phosphor crystallinity and the increased number of non-radiative transition paths that result from high luminescent impurity doping levels. Furthermore, at higher luminescent impurity doping levels, hysteresis in the L-V characteristics is sometimes observed.

In the present work, the fabricated devices were electrically excited using a 1.5 KHz trapezoidal waveform generated from a pulsed signal generator (Digilog Instruments Ltd.). The bipolar pulse train driving the device had a characteristic rise and fall time of 30  $\mu$ s each and a stay time of 70  $\mu$ s. A 0.32 m monochromator (Triax-320) coupled with Hamamatsu R928 photomultiplier tube was used to record the electroluminescent output from the fabricated device.

## 2.4 References

1. L. I. Maissel and R. Glang, Handbook of Thinfilm technology Mc Graw Hill Book Company, New York (1983).
2. A.Goswami, Thin Film Fundamentals. New Age International (P) Limited, New Delhi (1996).
3. K.L. Chopra, Thin Film Phenomena, Robert E. Krieger Publishing Co. Inc., New York (1979).
4. L. Holland, Vacuum Deposition of Thin films, John Wiley & Sons Inc., New York (1956).
5. Y.A.Ono, Electroluminescent displays. Singapore: World scientific, (1995).
6. Thin-Film Deposition-principles and practice, Donald L.Smith
7. Veeco Dektak ,6M Manual (2004)
8. B.D. Cullity and S.R. Stock, Elements of X ray diffraction, Third edition, Prentice Hall, New Jersey (2001).
9. M.J.Buerger, *X-ray Crystallography*, John Wiley & Sons, NewYork (1962)
10. Charles Kittel, Introduction to Solid State Physics, Seventh edn, Wiley Eastern Limited, New Delhi (1996).
11. P. E .J. Flewit and R. K. Wild, Physical methods for material characterization, second edition, IOP publishing, London (2003).
12. D. K. Schroder, Semiconductor material and device characterization, A Wiley-intersciernce publication, second edition (1998).

13. J.Bardeen,F.J.Blatt and L.H. Hall, Proceedings of Photoconductivity Conf. (1954,Atlantic City),(Eds) R.Breckenridze, B.Russel and T.Hahn, J.Wiley and Chapman and Hall, New York (1956).
14. P. Kubelka and F.Munk, Zh.Tekh.Fiz. **12** (1931) 593.
15. P. Kubelka, J. Opt. Soc .Am, **38** (1948) 448.
16. D.R.Vij (Ed.) Luminescence of solids, New York, Plenum Press (1998).
17. F.W. Billmeyer and M.Saltzman, Principles of color technology. New York: John Wiley and Sons, second ed;(1981).
18. A.C. Hardy, Handbook of colorimetry. Cambridge, MA: The Technology Press (1936).
19. T.J.Manning and W.R.Grow, The Chemical Educator, Springer Velag, New York (1997)
20. Pake G. E., Paramagnetic Resonance, (W. A. Benjamin, 1962).
21. Wertz J.E., Bolton J.R. Electron spin resonance. - New York, McGraw-Hill Book Company (1972)
22. C. P. Slichter, Principles of Magnetic Resonance (CLAS), 3rd ed., (Springer-Verlag, 1992 and Harper & Row, 1963), p. 65.

## CHAPTER THREE

# Colour control in SrS:Cu,Cl powder phosphor

### 3.1 Abstract

Control of defect type and concentration in strontium sulphide phosphor results in a broad range of colours in the visible part of the spectrum. Photoluminescence (PL) spectra on the blue to green emitting system SrS:Cu,Cl is presented and explained on the basis of charge compensation process and coordination about the  $\text{Cu}^+$  ion. Analysis of lattice parameter, strain and grain size were carried out on the basis of x-ray diffraction (XRD) data. From the analysis of diffuse reflectance spectra (DRS) shift in band gap was observed with variation in doping concentration which is due to the presence of doping induced tail states.

### 3.2 Introduction

Luminescence in alkaline-earth sulphides has been an active area of study for more than 75 years [1]. They are of considerable interest for application in electroluminescent (EL) displays, where their performance characteristics have been largely unsurpassed by other materials. Among these binary hosts, SrS is the most widely studied sample. SrS:Ce was first investigated for use in EL displays in 1984 [2] and it is still of interest for use in colour by white devices. Highly efficient, blue-emitting EL phosphor, SrS: Cu, and it's

modifications was reported by Sun et al.[3,4]. This was a very important breakthrough in the development of EL devices, as no high- efficiency blue EL phosphor was previously known. Incorporation of alkali metal ions into SrS lattice shifts the emission of SrS: Cu from blue to green region of the visible spectrum [5]. SrS: Cu emissions have one or more broad bands and their emission colour vary from blue to green and the luminescent mechanism is poorly understood [6-13]. In the present investigation, the tuning of emission colours and intensity of the SrS: Cu, Cl phosphor by varying the dopant concentration is discussed. By manipulating the defect chemistry and crystal properties in this material the emission colour can be tuned from blue to green.

### **3.3 Experimental**

The sulfide phosphor SrS:Cu was prepared by mixing definite proportions of  $\text{CuCl}_2$  with SrS powder. For this, high purity chemicals SrS (99.99%, Alfa Aesar) and  $\text{CuCl}_2 \cdot 2\text{H}_2\text{O}$  (99.99+%, Aldrich) were used. Required proportions of these highly pure precursors were accurately weighed and thoroughly mixed in ethanol medium. This powder was then placed in an oven at  $55^\circ\text{C}$  for two hours to dry and then ground well followed by firing for one hour at 1173K in  $\text{H}_2\text{S}$  atmosphere. Samples were prepared for different doping concentrations of Cu (0.1mol% to 2mol%). The structural and optical characterizations of these samples were then carried out.

Firing of the phosphor is very important in terms of AC powder electroluminescent device performance, primarily because the crystallinity of the powder is improved; more crystalline powders provide better electron

transport properties. Additionally, luminescent impurity centers are better incorporated into the lattice and thereby activated.

The crystal structures of the synthesized phosphors were studied using a Rigaku x-ray diffractometer with Cu K $\alpha$  x-ray. The photoluminescence (PL) and photoluminescence excitation (PLE) spectra were recorded with Jobin Yvon Fluoromax-3 Fluorimeter. The optical band gaps of the samples were estimated from the diffuse reflectance spectra recorded with Jasco-V-570 uv-vis-nir spectrophotometer.

### 3.4 Results and discussion

The powder x-ray diffraction patterns of pure SrS (with and without firing) and SrS:Cu,Cl fired at 1173K for one hour are shown in figure 3.1. From this it is clear that on firing, the crystallinity of the powder increases. It also shows that the small percentage of doping doesn't affect the crystal structure of the host material. During firing at relatively high temperatures and in H<sub>2</sub>S atmosphere, the Cu<sup>2+</sup> ions are reduced by H<sub>2</sub>S into Cu<sup>+</sup> ions and diffused into the SrS lattice [14]. The Cu<sup>+</sup> ions replace Sr<sup>2+</sup> ions in the octahedral site in the host lattice.

The lattice parameter  $a$  of SrS:Cu,Cl phosphor for each Cu doping concentration is calculated from  $a = \lambda(h^2+k^2+l^2)^{1/2}/2\sin\theta$  where  $\lambda$  is the x-ray wavelength; h, k and l are the Miller indices and  $\theta$  is the Bragg angle. The change in Cu concentration produces a shift in diffraction peaks and hence a change in lattice parameter. The diffraction peaks are shifted to higher  $2\theta$  values and the lattice parameter decreases while Cu concentration is increased from 0.1mol% to 0.5mol%. This is due to the fact that size of

$\text{Cu}^+$  ion ( $0.77\text{\AA}$ ) is comparatively less than that of  $\text{Sr}^{2+}$  ion ( $1.18\text{\AA}$ ) and for lower concentrations  $\text{Cu}^+$  ion enters the SrS lattice substitutionally. Since Cu is introduced in the form of  $\text{CuCl}_2$ , Cl ( $1.81\text{\AA}$ ) replaces some  $\text{S}^{2-}$  ( $1.84\text{\AA}$ ) ions which aids in charge compensation. But for higher concentrations  $\text{Cu}^+$  ion enters into SrS lattice at off centered Sr sites [15] and hence the lattice parameter increases.

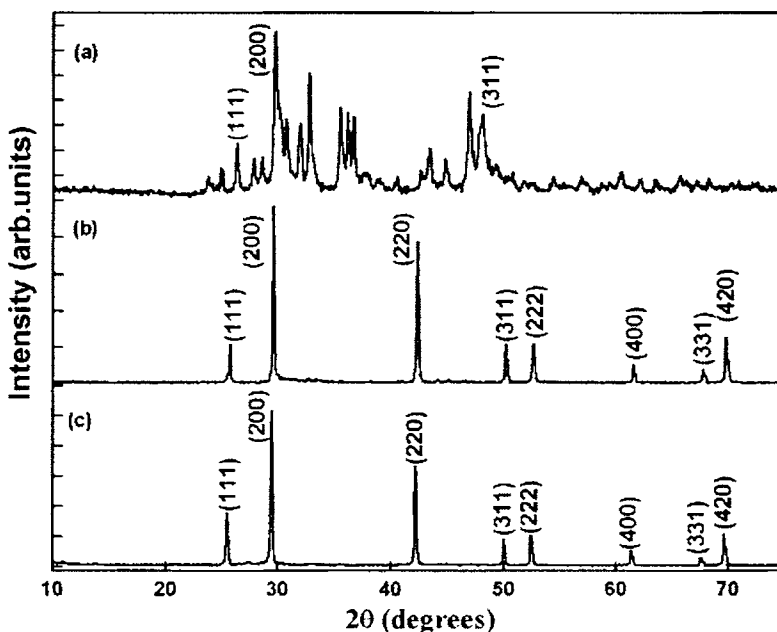


Figure 3.1. X-ray diffraction pattern of a). commercial SrS starting powder, b). Pure SrS fired at  $900^\circ\text{C}$  and c). SrS:Cu,Cl fired at  $900^\circ\text{C}$

The grain size and lattice strain of the different samples are estimated from the intercept and slope of the graph drawn between  $\sin\theta$  and  $B_r\cos\theta$  where  $B_r$  is the full width at half maximum (FWHM) in radians for a particular peak and  $\theta$  is the Bragg angle [16]. Grain size and lattice strain of of pure fired sample is found to be  $27.4\text{nm}$  and  $5.9 \times 10^{-4}$  respectively. Table I. Shows the

values of grain size, lattice strain and lattice parameter of different doped samples.

Table3.1. Grain size, lattice strain and lattice parameter of SrS:Cu,Cl phosphor for different Cu concentrations

Doping concentration (mol%)	Grain size (nm)	Lattice strain ( $\times 10^{-3}$ )	Lattice parameter (nm)
0.1	47.8	5.7	0.60618
0.2	31	2.3	0.60278
0.3	30.1	1.9	0.60277
0.5	27.2	1.6	0.60038
2	58.5	6.4	0.60287
2.5	62.5	6.9	0.60754

The diffuse reflectance spectra of various samples were recorded at room temperature with barium sulphate as reference. The ratio of absorption to scattering coefficient ( $k/s$ ) for pure SrS is calculated using Kubelka-Munk equation and the band gap is found by plotting  $h\nu$  vs.  $\{(k/s) \cdot h\nu\}^2$  as shown in figure 3.3 [17,18]. The band gap obtained from the plot was 4.23 eV. The band gap of doped samples was found to vary from 3.81 to 4.2eV. This is due to change in grain size and doping induced tail states. The band edges get perturbed by coulomb interaction with inhomogeneously distributed impurities leading to the formation of tails of states thereby reducing the bandgap [19].



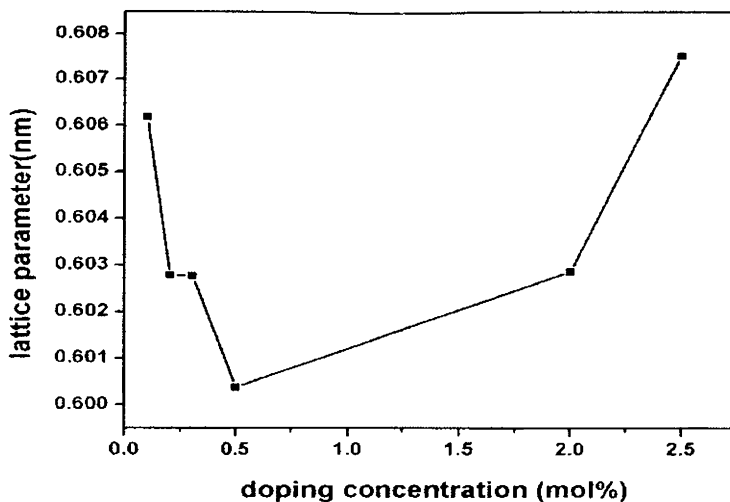


Figure 3.2 .Plot of doping concentration versus lattice parameter

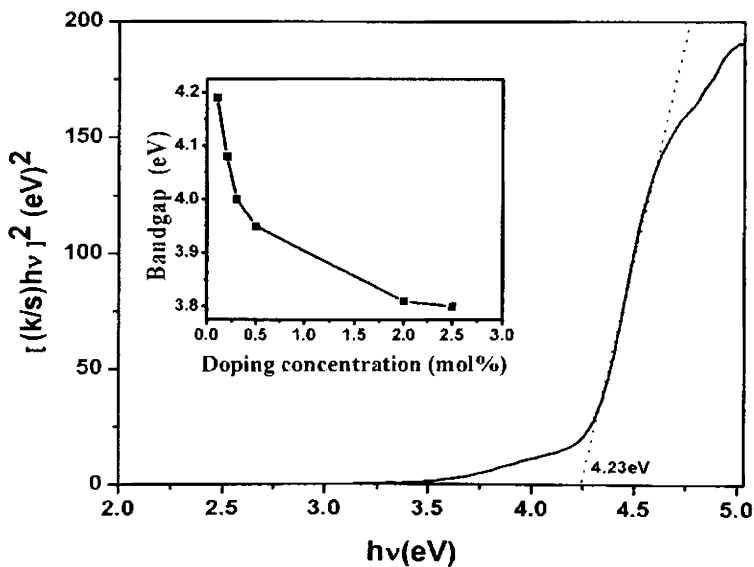


Figure 3.3 Plot of  $\{(k/s).hv\}^2$  versus energy of pure SrS fired at  $900^{\circ}\text{C}$  for one hour.

Inset shows the variation of bandgap with doping concentration

The Photoluminescence emission (PL) and Photoluminescence excitation (PLE) spectra of the prepared samples with different Cu concentrations were recorded at room temperature.

Figure 3.4 shows PL excitation spectra of SrS:Cu,Cl phosphors with different copper concentrations. Two bands at 284nm and 315nm are observed of which the L (low energy) band shifts towards higher wavelength with increasing doping concentration. There was no considerable change in the H (high energy) band with respect to the Cu concentration. These two bands can be attributed to the intracenter excitation in  $\text{Cu}^+$  ions. The emission wavelength was found to shift from 470nm to 520nm with increase in copper concentration (from 0.1mol% to 2.5 mol%) at an excitation wavelength of 310nm. The emission intensity reaches maximum for a doping concentration of 0.2mol% and decreases afterwards. This is due to concentration quenching by which a molecule quenches its own fluorescence at high concentration.

The emission-reabsorption energy transfer between ions of the same kind can result in self-absorption. Figure 3.6 shows the variation of emission wavelength and intensity with respect to Cu concentration. The change in the emission color with respect to Cu concentration can be explained as follows.

SrS:Cu Phosphor is an efficient blue emitting sulfide phosphor. Both blue and green emission in SrS:Cu powders and films has been reported. The two copper atoms in dumbbell are situated close to an  $\text{Sr}^{2+}$  vacancy in a {100} plane containing this vacancy. Thus the center is neutral with respect to the perfect SrS crystal.

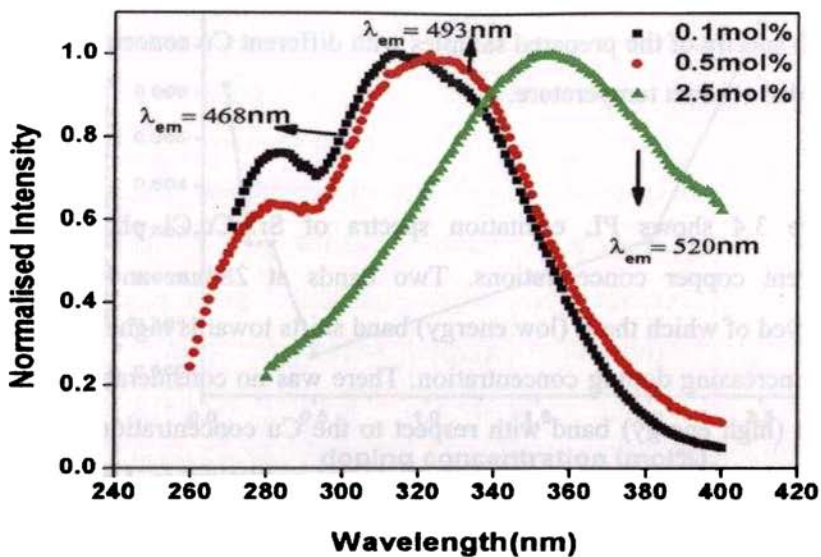


Figure 3.4. PL excitation of Cu doped SrS powder at room temperature.

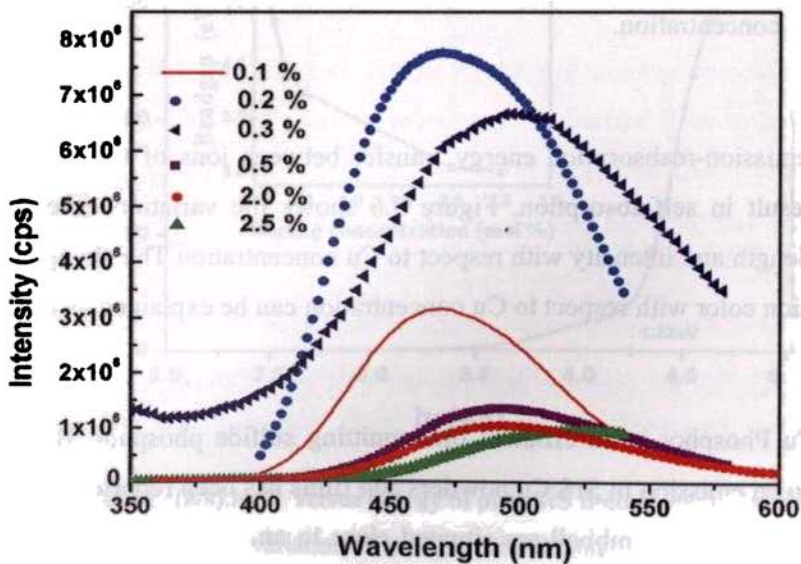


Figure 3.5. Photoluminescence spectrum of SrS:Cu,Cl phosphor for different Cu concentrations at room temperature,  $\lambda_{ex}=310\text{nm}$

Optical transitions in  $\text{Cu}^+$  ions belonging to dumbbell centers are responsible for low energy (L) band observed in the PL spectra. Such transitions are dipole allowed since the system does not have inversion symmetry. Transitions in interstitials are not inversion symmetrical give rise to high energy (H) band [15]. The energy level diagram of a free  $\text{Cu}^+$  ion and  $\text{Cu}^+$  ion in an octahedral crystal field is as shown in the figure 3.7.

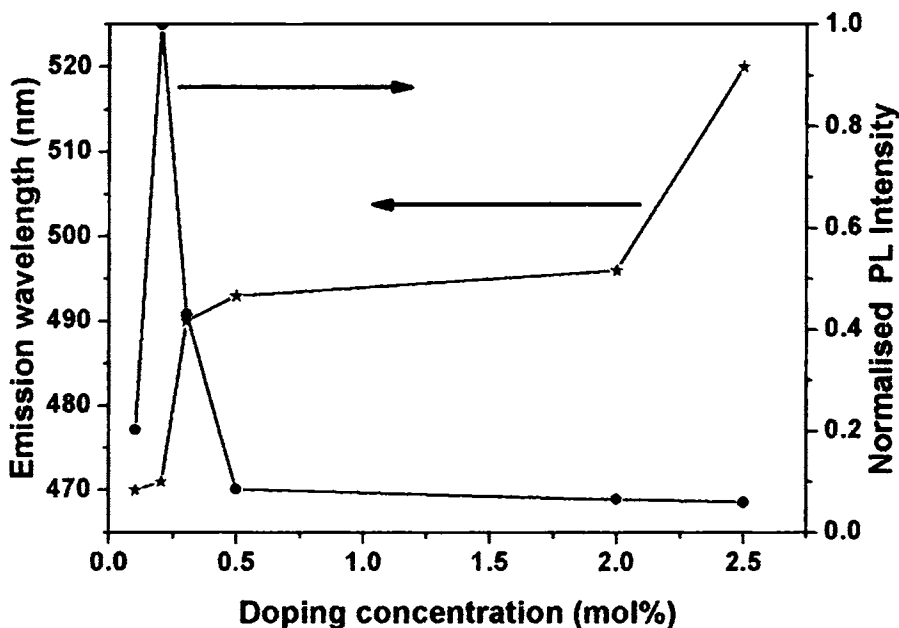


Figure 3.6. Change in peak emission wavelength and Intensity with Cu Concentration in SrS powder

In the excitation spectra of all the samples, there appear two bands (peaks at 284nm and 315nm), assigned to the transitions  $3d^{10}[^1A_{1g}]$  to  $3d^9, 4s[^1E_g, ^1T_{2g}]$  with in the isolated  $\text{Cu}^+$  ion. The  $3d^{10}[^1S_0]$  to  $3d^9, 4s[^3D_{3,2,1}; ^1D_2]$  transition in the  $\text{Cu}^+$  ion are parity and J- forbidden which are relaxed in a

perturbed crystal field. The emission process has been attributed to the transition from lowest excited state  $3d^9, 4s^1 [^3E_g]$  to ground state  $3d^{10} [^1A_{1g}]$  [20].

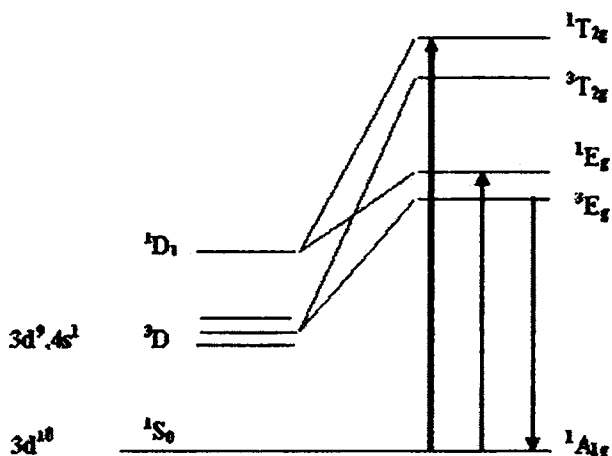


Figure 3.7 Schematic energy levels of free  $Cu^+$  ion and  $Cu^+$  ion in the crystal field with octahedral symmetry

Three emission bands were reported by Laud et al.[21] with peaks at about 471nm, 517nm and 548nm. The band at 471nm was explained as due to  $Cu^+$  ion in the interstitial site adjacent to a  $Cu^+$  ion on a lattice site, whereas the other two bands were explained as due to  $Cu^+$  ion in the substitutional (off-center) position.

The emission wavelength of the  $Cu^+$  luminescence in SrS:Cu depends on the Cu concentration, co-dopants and temperature. Yamashita et al reported 4 types of  $Cu^+$  bands in SrS:Cu at 80K [13]. Blue luminescence in SrS:Cu is produced by  $[Cu^+_{Sr}]^-$  centers with coordination number 6. The coordination number refers to the number of  $S^{2-}$  ions closest to the  $Cu^+$  ion. Such a situation arises when a  $Cu^+$  ion occupies an interstitial site adjacent to a  $Cu^+$

ion in the lattice site there by causing charge compensation without producing sulphur vacancies. Such  $[\text{Cu}^+_{\text{Sr}}]^-$  centers have inversion symmetry and so should have only low optical activity. But the Cu interstitials formed for charge compensation are not inversion symmetrical and hence give rise to blue luminescence.

Coordination number 5 implies that there are sulfur vacancies near the  $[\text{Cu}^+_{\text{Sr}}]^-$  centers, which lowers the symmetry of  $\text{Cu}^+$  center, and green luminescence is produced. Or in other words green luminescence is produced by Cu on Sr site off-center position. In order to improve the blue chromaticity of the SrS:Cu phosphor the number of  $[\text{Cu}^+_{\text{Sr}}]^-$  centers with coordination number 6 should be increased compared to the number of  $[\text{Cu}^+_{\text{Sr}}]^-$  centers with coordination number 5. Blue emission is also observed if the  $\text{Cu}^+$  ion is in an off-center tetrahedral position coordinated by four sulphur atoms [15]. Since ionic radius of  $\text{Cu}^+$  ion (0.96Å) is comparatively less than that of  $\text{Sr}^{2+}$  ion (1.18Å),  $\text{Cu}^+$  ions are less likely to replace  $\text{Sr}^{2+}$ . Hence off centered  $\text{Cu}^+$  ions are more common (usually in higher concentrations) which will give rise to green emission.

In the present study, at lower concentrations emission peak at 470nm is observed. This implies that  $\text{Cl}^-$  is incorporated into the lattice as a substitution donor on sulphur sites within the SrS:Cu lattice, thereby reducing sulphur vacancies or charge is intrinsically compensated with  $\text{Cu}^+$  ion in interstitial site adjacent to a  $\text{Cu}^+$  ion in the lattice site. The result of the incorporation of  $\text{Cl}^-$  donors is that the SrS:Cu,Cl phosphor is extrinsically compensated due to the presence of  $\text{Cl}^-$  donors, eliminating, or at least reducing the process of selfcompensation. The drastic reduction of sulphur vacancies through extrinsic compensation results in the presence of more blue-emitting six coordinated variety of  $\text{Cu}^+-\text{Cl}^-$  complexes than green

emitting  $\text{Cu}^+ - V_s$  complexes. As the concentration is increased a colour shift to green is observed. This can be attributed to the formation of copper pairs and isolated off-centered sites [13].

Table 3.2 CIE coordinates of Cu doped SrS samples.

Doping concentration of Cu (mol%)	CIE	
	x	y
0.1	0.125	0.193
0.2	0.127	0.226
0.3	0.219	0.370
0.5	0.178	0.402
2.0	0.203	0.407
2.5	0.121	0.558

The CIE coordinates of the PL emission of the SrS host and Cu doped samples are calculated. The CIE coordinate for Cu doped samples is given in the table 3.2. These coordinates can be represented inside a gamut drawn from the standard x, y values as shown in figure.3.8.

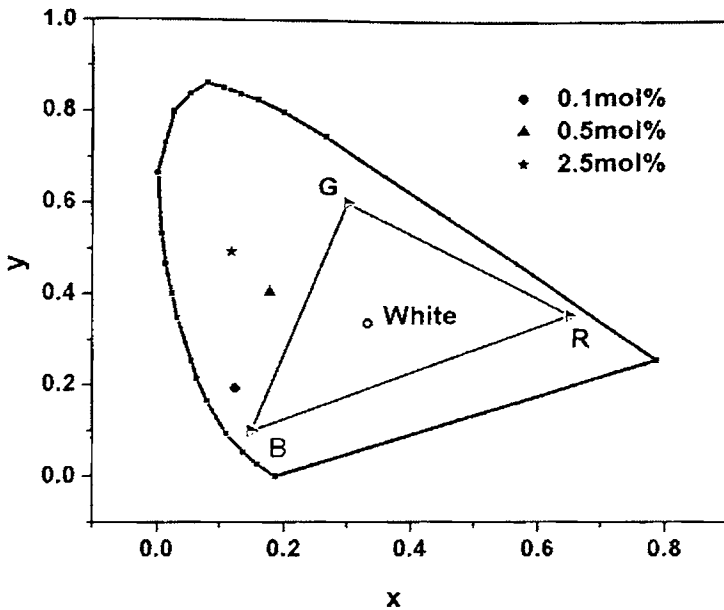


Figure 3.8 CIE chromaticity diagram. Colour coordinates of the SrS:Cu,Cl phosphor samples for different Cu concentrations

### 3.5 Conclusions

Blue and green emitting SrS:Cu,Cl phosphors have been prepared by solid state reaction between SrS and CuCl<sub>2</sub> powders. Different samples were prepared by varying the concentration of copper from 0.1mol% to 2.5mol%. The X-ray diffraction pattern of the powder samples show that all the doped and undoped samples were crystallized in the rock salt structure. The lattice parameter decreases at lower concentrations and increases at high concentrations depending upon whether Cu<sup>1</sup> ion is in the substitutional site (along with another Cu<sup>1</sup> ion in lattice site) or off-centered site.



Red shift in absorption edge was observed with increasing doping concentration. This may be due to doping induced tail states. The room temperature photoluminescence emission spectra of Cu doped samples showed blue emission at low concentrations (468nm for 0.1mol%) and shift to green (520nm for 2.5mol%) as the concentration is increased from 0.1mol% to 2.5mol% which is explained on the basis of  $\text{Cu}^+$  centers and charge compensation. Maximum intensity was obtained for sample with 0.2mol% Cu. The Photoluminescence excitation spectra of samples show peaks at 284nm and 315nm respectively, in which the 315nm peak showed red shift with increasing copper concentration. Since the spectral energy distribution in SrS:Cu,Cl system is known to be independent of excitation source, similar results are expected in the function of electroluminescent devices also.

### 3.6 References

- 1 P.Lenard, F.Schmidt and R.Tomascheck, Handbook of Experimental Physics, **23**, Akademie Verlagsges, Leipzig,1928
- 2 W.A.Barrow, R.E.Covert and C.N.King, Digest of the 1984 SID Int'l Display Symposium, (1984) 249
- 3 S.S.Sun, E.Dickey, J.Kane and P. N.Yocom, Proc.17<sup>th</sup> Int.Display Research Conf., Morreale,J.,Ed.;Society for Information Display: Santa Ana, CA, (1997) 301
- 4 Sun.S.S.Extended abstracts,4<sup>th</sup> Int. Conference on Science and Technology of Display Phosphors. Bend,OR. Society for Information Display:Santa Ana,CA 1998.
- 5 P.D.Keir, J.F.Wager, B.L Clark, A.Keszler, Appl. Phys. Lett.**75** (1999) 1398
- 6 W.Lehmann, J.Electrochem.Soc.**117** (1970) 1389
- 7 N.Yamashita, Jpn.J.Appl.Phys. **30** (1991) 3335
- 8 B.B.Laud and V.W.Kulkarni, J.Phys.Chem.Solids **39** (1978) 555
- 9 A.Vecht, M.Waite, M.H.Higton, and R.Ellis, J.Lumin. **24/25** (1981) 917
- 10 M.Avinor,A.J.Carmi and Weinberger,Chem.Phys, **35** (1967) 1978
- 11 D.Sharma and Amarsingh, Indian J.Pure.Appl.Phys **9** (1971) 810
- 12 P.S.Kanari, Indian J.Pure.Appl.Phys **9** (1971)1060
- 13 N.Yamashita, K.Ebisumori, K.Nakamura, Jpn.J. Appl. Phys. **32** (1993) 3846
- 14 Y.B.Xin, W.Tong, W.Park, M.Chaichimansour, C.J.Summers' Appl. Phys. **85** (1999) 3999.

- 15 D.Wruck, R.Boyn, M.Wienecke, F. Hennerberger, U.Tropenz, B, Hutil, W.Bohne, B.Reinhold and H.-E. Mahnke, *J.Appl.Phys*, **91** (2002) 2847
- 16 X-Ray Diffraction –a practical approach,C.Suryanarayana and M.Grant Norton,Plenum Press, New York and London.1998
- 17 P. Kubelka and F.Munk, *Zh. Tekh. Fiz* **12**(1931) 593
- 18 P.Kubelka, *J. Opt. Soc. Am* **38** (1948) 448.
- 19 J.I.Pankove, *Optical processes in semiconductors*, New York (Dover publications) (1975) 10
- 20 J.Ihanus,M.Ritala,M. Leskela, W. Park, A.E.kaloyeros, W. Harris, K.W.Barth and A. W.Topol, *J.Appl.Physics* **94** (2003)3862
- 21 B.B.Laud and V.W.Kulkarni, *J.Phys.Chem.Solids* **39** (1978) 555

-

## CHAPTER FOUR

# Effect of $\text{NH}_4\text{Cl}$ flux on the structural and luminescence properties of $\text{SrS}:\text{Cu},\text{F}$ phosphor

### 4.1 Abstract

Efficient  $\text{SrS}:\text{Cu}$  phosphor can be prepared by solid state reaction fired in  $\text{H}_2\text{S}$  atmosphere. Use of  $\text{NH}_4\text{Cl}$  as flux agent favours the crystal growth of  $\text{SrS}$ . Blue PL emission intensity became five times with the addition  $\text{NH}_4\text{Cl}$  to the  $\text{SrS}:\text{Cu}$  phosphor.

### 4.2 Introduction

The purpose of a flux in a phosphor material is to improve the crystallinity of the phosphor host lattice by assisting atomic diffusion during high temperature processing. Flux is extremely important for ACTFEL phosphors because they provide a means of achieving crystallinity at the low processing temperatures necessary for deposition on to glass substrates. Most effective flux agents are non-isovalent with the constituent elements of the phosphor host because their operation relies upon their ability to generate vacancies to compensate for their presence. These vacancies lead to enhanced atomic motion through the phosphor, enhancing the formation of a crystalline lattice. Tang et al. reported the effect of  $\text{LiCl}$  flux on red  $\text{ZnS}:\text{Sm}$  phosphors [1]. Luminous intensity of  $\text{Y}_2\text{O}_3$  was found to enhance by the addition of flux [2].  $\text{CaF}_2$  was used as flux in  $\text{SrS}:\text{Cu}$  phosphor by Yamashita

et al [3]. In this chapter the role of  $\text{NH}_4\text{Cl}$  as a flux on the structural and optical properties of SrS:Cu phosphor is presented.

### 4.3 Experimental

Starting powders of high purity, such as SrS(99.99%, Alfa Aesar) , 0.2mol% of  $\text{CuF}_2 \cdot 2\text{H}_2\text{O}$  (99.99+%, Aldrich) as activator and 5wt.% of  $\text{NH}_4\text{Cl}$  were weighed on a microbalance and then thoroughly mixed in ethanol medium. The mixed slurry was then placed in an oven at  $55^\circ\text{C}$  for two hours to dry. The powder loaded in a quartz crucible was fired at  $850^\circ\text{C}$  for 1 hour in  $\text{H}_2\text{S}$  atmosphere. After air-cooling to room temperature, the powder was structurally characterized using Rigaku X-ray diffractometer with Cu  $\text{K}\alpha$  radiation at 30kV, 20mA at a scanning rate of  $2^\circ/\text{min}$ . The photoluminescence emission and excitation spectra were recorded using Jobin Yvon Fluoromax-3 Fluorimeter. The diffuse reflectance spectrum was recorded with Jasco-V-570 uv-vis-nir spectrophotometer. Another sample without flux was also prepared and characterized in the same manner.

### 4.4 Results and discussion

Fig.4.1 shows the x-ray diffraction patterns of SrS:Cu,F phosphor with and without flux. The pattern of sample without flux contains diffraction peaks of the host as well as impurity peaks. But for the sample with flux, the impurity peaks disappear and the diffraction peaks of SrS are only visible. Addition of flux helped in lowering the crystallization temperature. The average particle size of both samples were estimated using Scherrer formula considering the line broadening of the XRD patterns ( $D=0.9\lambda/\beta\cos\theta$ , where  $\lambda$  is the wavelength of the incident x-rays,  $\beta$  is the full width at half maximum of the diffraction peaks in radians and  $\theta$  is the angle of

100

diffraction). Particle size of the sample with  $\text{NH}_4\text{Cl}$  flux (45nm) is double that of the sample prepared without flux (22nm). The lattice strains of the samples are estimated from slope of the graph drawn between  $\sin\theta$  and  $\beta\cos\theta$  [4]. The strain (0.03) for the sample with flux is far greater than that for the sample without flux (0.0018) due to the high density of defects.

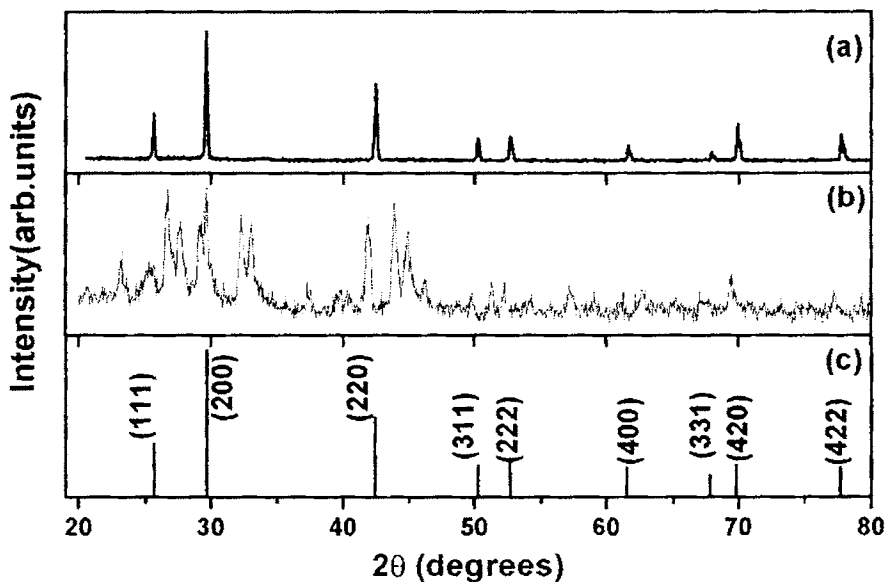


Figure 4.1. XRD patterns of (a).SrS:Cu,F phosphor with flux, (b) SrS:Cu,F phosphor without flux, (c).the peak positions and intensities for pure SrS (JCPDS 08-0489).

The absorbance spectra of the samples are shown in figure 4.2. Peaks (a) and (b) corresponds to absorption in the host lattice and  $\text{Cu}^{2+}$  intracenter absorption respectively. The absorption peak (a) of the host lattice, in the sample synthesised with flux is broadened and red shifted with respect to the sample without flux which may be due to, the presence of multiple defects (band tailing effect).

Fig.4.3 shows the PL spectra of the samples monitored at an excitation wavelength of 280nm. Emission intensity for the sample synthesised with flux is 6 times that for the sample without flux. Also the emission wavelength for the sample with flux (486nm) is red shifted with respect to that for the sample without flux (473nm) even though doping concentration is same for both the samples. This shows that  $\text{Cu}^+$  ions are more effectively incorporated into the SrS lattice for the sample prepared with flux since increase in  $\text{Cu}^+$  concentration causes a red shift in the PL emission as explained in chapter3.

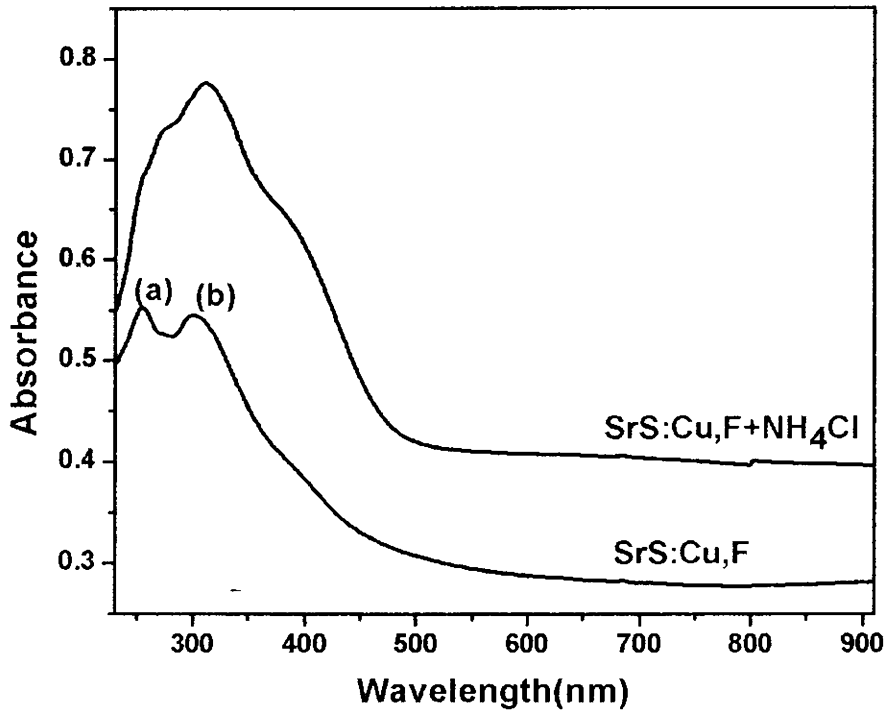


Figure 4.2. Absorbance spectra of SrS:Cu,F with and without flux

A PLE spectrum of the samples monitored at an emission wavelength of 482nm is shown in figure 4.4. Two excitation peaks are observed. Peak around 270nm is due to excitation in the host, whereas that around 320nm is due to  $\text{Cu}^+$  intracenter excitation. For the sample without flux, excitation is more in the host whereas for the sample with flux the intracenter excitation peak is dominant. This leads to the conclusion that addition of flux aided the diffusion of  $\text{Cu}^+$  ions in the host lattice to replace  $\text{Sr}^{2+}$  ions. There is shift in both peaks and broadening for the host excitation peak with the addition of flux. This is due to band tailing effect since the addition of flux causes the formation of defect states [5].

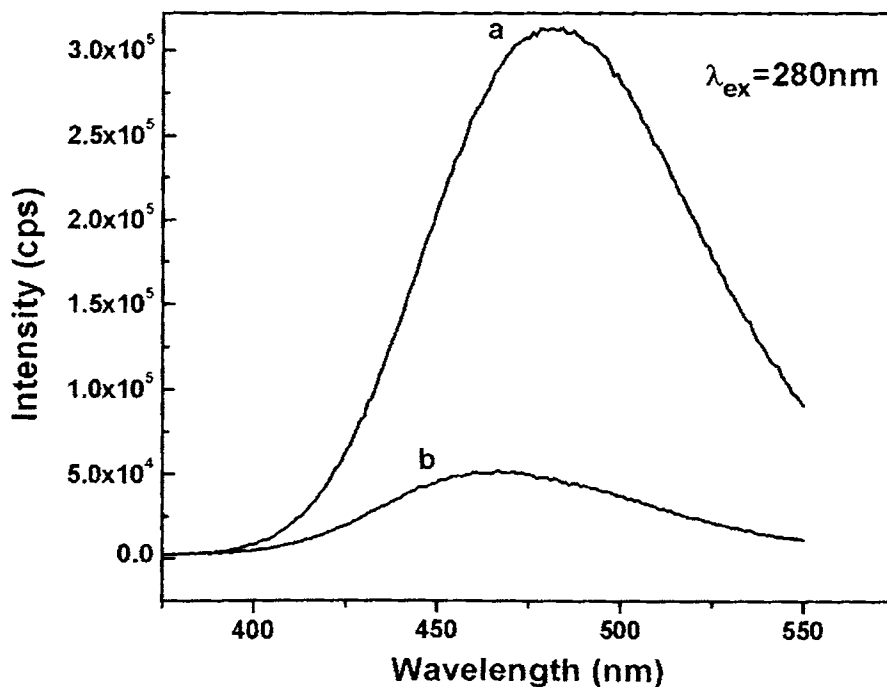


Figure 4.3: PL spectra of (a) SrS:Cu,F phosphor with  $\text{NH}_4\text{Cl}$  flux and (b) SrS:Cu,F without flux



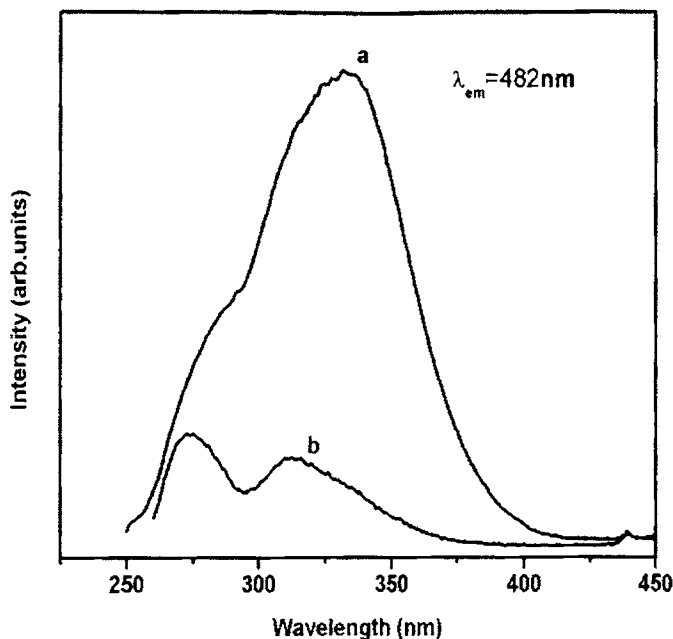


Figure 4.4: PLE spectra of (a) SrS:Cu<sub>2</sub>F prepared with NH<sub>4</sub>Cl flux and (b) SrS:Cu<sub>2</sub>F without flux

## 4.5 Conclusion

Copper doped strontium sulphide phosphors were synthesised with and without ammonium chloride as flux by solid state reaction and their structural and optical properties were compared. Addition of flux improved the crystallinity of SrS. Absorption spectra consisted of two peaks corresponding to absorption of the host lattice and Cu<sup>+</sup> intracenter absorption which were red shifted on addition of the flux. This may be due to band tailing effect. Both PL and PLE intensities enhanced to six times due to the addition of flux. Red shift in photoluminescence emission may be due to more efficient incorporation of Cu<sup>+</sup> ions on Sr<sup>2+</sup> site.

## 4.6 References

1. T.P. Tang, M.R. Yang and K.S. Chen, *Ceram.Int.* **26** (2000) 341.
2. G.Y.Hong, K.Yoo, S.J.Moon and J.S.Yoo, *J.Electrochem.Soc.* **150** (2003) H67
3. N.Yamashita, K.Ebisumori and K.Nakamura *Jpn.J.Appl.Phys.* **32** (1993)3846
4. C.Suryanarayana and M.Grant Norton, *X-Ray Diffraction—a practical approach*, Plenum Press, New York(1998)
5. J.I.Pankove, *Optical Processes in Semiconductors*, Dover publications, Inc. New York (1971)

## CHAPTER FIVE

# Luminescence properties of SrS:Dy,Cl phosphor

### 5.1 Abstract

The fundamental optical properties of dysprosium (Dy) doped strontium sulfide bulk samples for various dopant concentrations from (0.1-1.0at.%) were investigated by electron paramagnetic resonance spectroscopy (EPR), room temperature photoluminescence (PL), photoluminescence excitation (PLE) and diffuse reflectance spectroscopy (DRS). Investigations by electron paramagnetic resonance yielded the state of Dy in the sample as  $Dy^{3+}$ . An additional EPR line due to  $F^+$  centre was also observed. The PL emission spectrum consisted of several intense lines and a number of weaker ones which were identified as transitions between energy levels of  $Dy^{3+}$ . The optimum doping concentration for maximum intensity was found to be 0.25at.%. Blue shift of the band gap energy and red shift of the PLE spectrum were observed with increasing doping concentration. The former is due to Burstein-Moss (BM) effect and the latter is attributed due to the presence of band tailing. The yellow-to-blue intensity ratios(Y/B) of  $Dy^{3+}$  emission in SrS lattice for different concentrations were also evaluated.

## 5.2 Introduction

Alkaline earth sulfide phosphors have aroused much interest after the discovery of infrared stimulation and sensitized luminescence [1,2] because of their potential as host materials for device applications, such as multicolour thin film electroluminescent [3] and magneto optical devices [4,5]. Non-toxic sulfides are most commonly used as a host lattice for phosphors. Due to the wide variety of emission wavelength possible from 4f-4f transitions of rare earth ions in the visible spectrum, rare earth doped alkaline earth phosphors are widely being investigated [6]. The close match of the ionic radii of rare earth ions and cation of SrS host material, allow the rare earths to fully incorporate in these lattices. In the case of ZnS lattice it is difficult to fully incorporate the rare earth ions because of large difference in ionic radii. The electroluminescent emission spectra of the lanthanide luminescent impurity in SrS and ZnS show a difference in relative peak intensities [7,8]. This has been attributed to the differences in the branching ratio of the emitting level due to crystal field.

SrS:Dy is a promising phosphor for yellow electroluminescence. Although considerable attention has been paid to the study of PL of SrS phosphors activated with dysprosium, not much quantitative data are available relating to the influence of concentration of Dy on the PL and band gap of SrS:Dy phosphors. In this chapter, a detailed study on the dependence of doping concentration of Dy on the photoluminescence, band gap and excitation energy of SrS host matrix is presented.

## 5.3 Experimental

SrS:Dy,Cl phosphor was prepared by solid state reaction of SrS (99.9%, Alfa Aesar) with DyCl<sub>3</sub> (99.99%, Indian Rare Earths Ltd.). The mixture was fired at 900°C for 1 hour in hydrogen sulfide atmosphere. This powder was pulverized in a dry atmosphere and stored, keeping in view of the extreme purity as the main consideration in the preparation. The crystal structure of the synthesized phosphors were studied using a Rigaku x-ray diffractometer with Cu K $\alpha$  x-ray. The PL and PLE spectra were recorded with Jobin Yvon Fluoromax-3 Fluorimeter. The optical band gaps of the samples were estimated from the diffuse reflectance spectra recorded with Jasco-V-570 uv-vis-nir spectrophotometer. The nature of the luminescent impurity in the host was studied by recording the EPR spectra using Varian E-112 E-line Century series X-band EPR spectrometer. The electrical conductivity of the samples pelletized at a pressure of 2 tonnes was measured using a Keithley source measure unit (SMU 236). Silver paste was used as the electrode on either side of the pellets having a diameter of 1cm.

## 5.4 Results and discussion

### 5.4.1 EPR measurements

EPR measurements were carried out on a Varian E-112 E-line Century series X-band EPR spectrometer at room temperature for the concentrations of Dy concentration varying from 0.1at.% to 1 at.%. Tetracycloethelene (TCNE,  $g = 2.00277$ ) was used as a standard for g-factor measurements. EPR yielded site-selective information on Dy impurities in the SrS lattice. The spectrum of the powder samples showed a symmetric signal at a g value of 2.08 and

another signal at a g value 2.00587 with a line width 20 gauss close to the left of the TCNE marker. The line adjacent to the marker (Fig.5.1) is due to the  $F^+$  centre [9, 10] produced by sulfur vacancy. The symmetric signal with six lines is due to the hyperfine splitting of  $Dy^{3+}$  ( $I=5/2$ ). The relative intensity of the EPR signal corresponding to the  $Dy^{3+}$  ions increased with doping concentration.  $Dy^{3+}$  is introduced by doping  $DyCl_3$  which is incorporated as  $Dy^{3+}$  on Sr sites. To maintain charge neutrality, defect complexes like  $[Dy^{3+}_{Sr} V_{Sr}]^-$  or  $[Cl^- V_{Sr}]^-$  are possible. Chlorine ions can

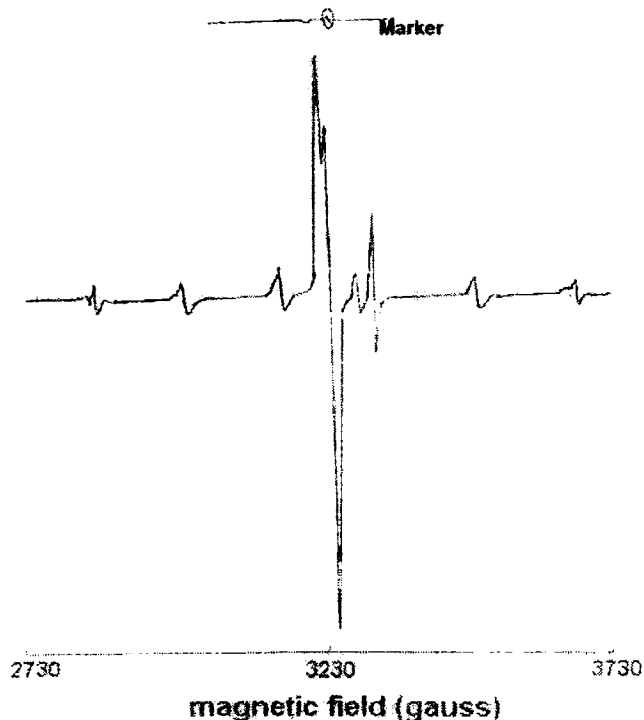


Figure5.1. EPR spectrum of SrS:Dy,Cl phosphor for 0.25 at.% of Dy doping concentration

occupy sulfur vacancies and also donate free electrons. Sulphur vacancies trap these electrons forming  $F^+$  centres. The EPR signal intensity

corresponding to the  $F^+$  center also increased with doping concentration of  $Dy^{3+}$  ions (Figure 5.2).

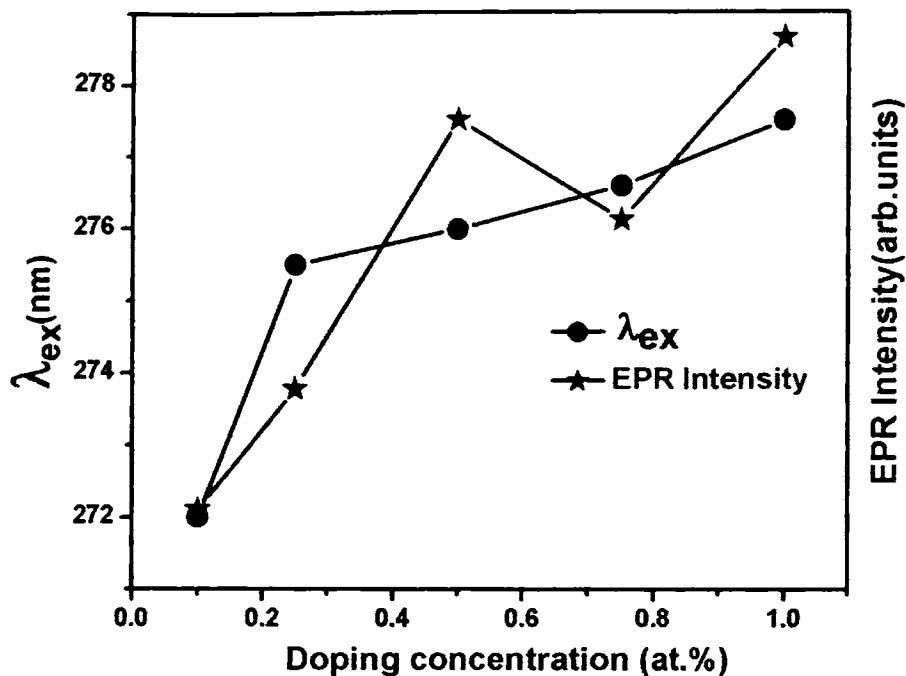


Figure 5.2. EPR intensity of  $F^+$  centre and excitation peak wavelength as a function of doping concentration

#### 5.4.2 Photoluminescence spectra of $SrS:Dy,Cl$

Photoluminescence emission spectrum of  $Dy^{3+}$  in the  $SrS$  powder under excitation of 274 nm (Fig 5.3) show characteristic lines of  $Dy^{3+}$  [11,12]. The lines at 481, 574, 664 and 756 nm correspond to  ${}^4F_{9/2} \rightarrow {}^6H_{15/2}$ ,  ${}^6H_{13/2}$ ,  ${}^6H_{11/2}$ , and  ${}^6H_{9/2}$  transitions respectively, whereas the transitions  ${}^4F_{7/2} \rightarrow {}^6H_{13/2}$ ,  ${}^6H_{11/2}$ ,  ${}^6H_{7/2}$ ,  ${}^6H_{5/2}$  and  ${}^6F_{7/2}$  lead to the emission lines at 457, 486, 580, 657 and 669 nm respectively. This reaffirms our earlier contention that the dysprosium

luminescent impurities are incorporated as  $Dy^{3+}$  state producing the typical spectra of the trivalent rare earth ion.

The PL emission from the sample was yellow with chromaticity coordinates  $x=0.40$ ,  $y=0.42$ . Elizebath et al.[11] reported two fluorescence bands at 480nm and 571nm( ${}^4F_{9/2} \rightarrow {}^6H_{15/2}$  and  ${}^6H_{13/2}$ ) with  $Dy^{3+}$  in an oxalate matrix. Kirsh and Townsend [12] reported a broad line for two allowed transitions  ${}^4F_{9/2} \rightarrow {}^6H_{15/2}$  and  ${}^4F_{7/2} \rightarrow {}^6H_{11/2}$  centered at 485nm. Also, they obtained a single broad line for  ${}^4F_{9/2} \rightarrow {}^6H_{13/2}$  and  ${}^4F_{7/2} \rightarrow {}^6H_{7/2}$  transitions centered at 580nm. In the present work all emission lines were well resolved.

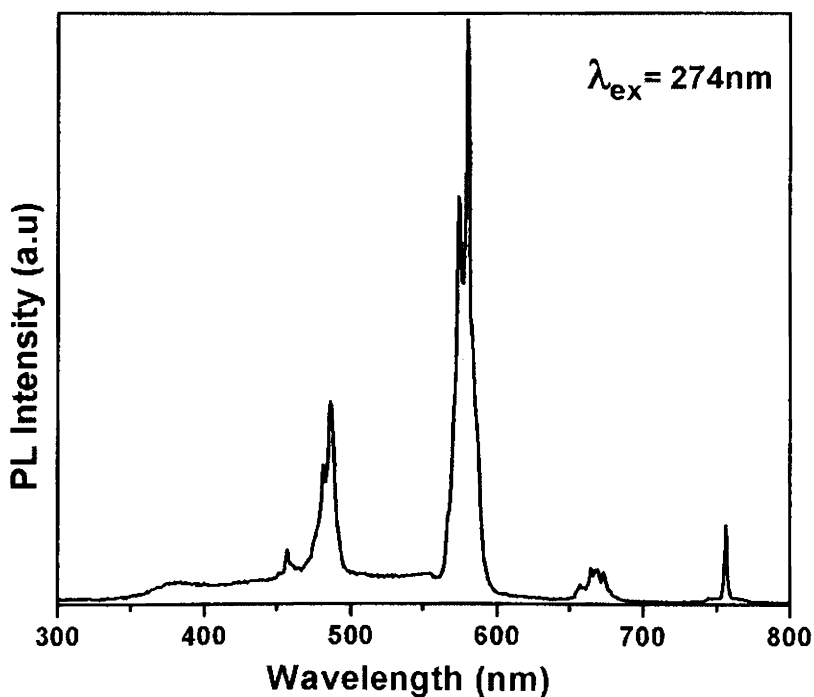


Figure 5.3.. PL spectrum of SrS:Dy,Cl phosphor with 0.25 at.% of Dy



The effect of concentration on PL intensity was also studied. Dysprosium doping concentration was varied from 0.1at.% to 1 at.%. The emission intensities increased with the doping concentration and maximum was observed for a concentration of 0.25 at.% and thereafter decreased (Fig5.4).This decrease can be attributed due to concentration quenching. This results from the nonradiative resonance multipole energy transfer between ions of the same type [13].

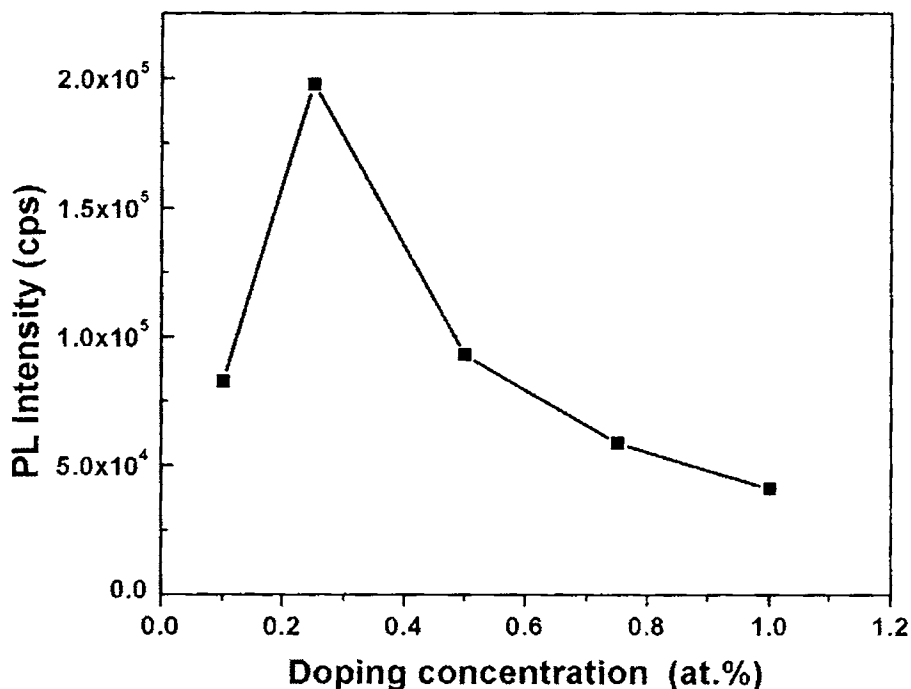


Figure 5.4. Variation of PL intensity with doping concentration of Dy in SrS:Dy,Cl phosphor

#### 5.4.3. Yellow-to-blue intensity ratio (Y/B)

As we have seen earlier the yellow band (581nm) of Dy<sup>3+</sup> emission corresponds to the hypersensitive transition  ${}^4F_{9/2} \rightarrow {}^6H_{13/2}$  and the blue band

corresponds to  ${}^4F_{9/2} \rightarrow {}^6H_{15/2}$  transition. The yellow-to-blue intensity ratio of  $Dy^{3+}$  emission depends upon the environment. When  $Dy^{3+}$  is substituted for an element with the same valency in the matrix (e.g. trivalent rare earths), the value of Y/B generally does not vary much with variation in the concentration of  $Dy^{3+}$ . When  $Dy^{3+}$  is substituted for an element with a different valency, defects will be formed, and the surrounding and local symmetry of  $Dy^{3+}$  will change with increasing concentration of  $Dy^{3+}$ . Hence the value of Y/B varies with variation in the concentration of  $Dy^{3+}$  [14]. In the present work since  $Dy^{3+}$  replaces  $Sr^{2+}$ , the value of Y/B varied with variation in doping concentration (Table 5.1). The resultant emissions from the different samples are represented in the CIE chromaticity diagram (Fig. 5.5).

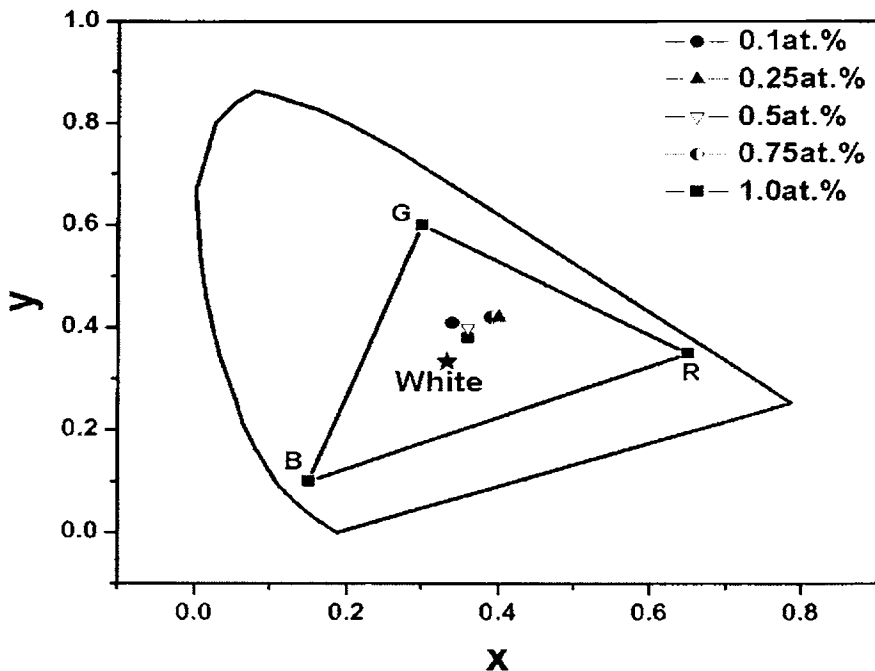


Figure 5.5. CIE chromaticity diagram of SrS:Dy phosphor for various Dy concentrations

Table.5.1.Variation of yellow-to-blue intensity ratio (Y/B) and chromaticity coordinates with Dy<sup>3+</sup> concentration in SrS

Dy <sup>3+</sup> (at.%)	Y/B	Chromaticity coordinates	
		x	y
0.1	4.9	0.34	0.41
0.25	4.2	0.4	0.42
0.5	4.1	0.36	0.4
0.75	3.6	0.39	0.42
1.0	3.1	0.36	0.38

#### 5.4.4 Photoluminescence excitation spectra

PLE and PL spectrum of undoped SrS is shown in Fig.5.6. Excitation intensity was found to be maximum at 278 nm for an emission wavelength of 381nm.The PLE spectra of the doped samples (Fig.5.7) with different concentrations of Dy were also recorded at room temperature with  $\lambda_{em}$  at 486 nm. The excitation spectra of all samples are broad centered around 275 nm which corresponds to the band to band excitation of SrS host matrix which has a band gap  $\sim$  4.3 eV. This result suggests that the Dy<sup>3+</sup> luminescent centre is excited via the energy transfer from the host matrix.

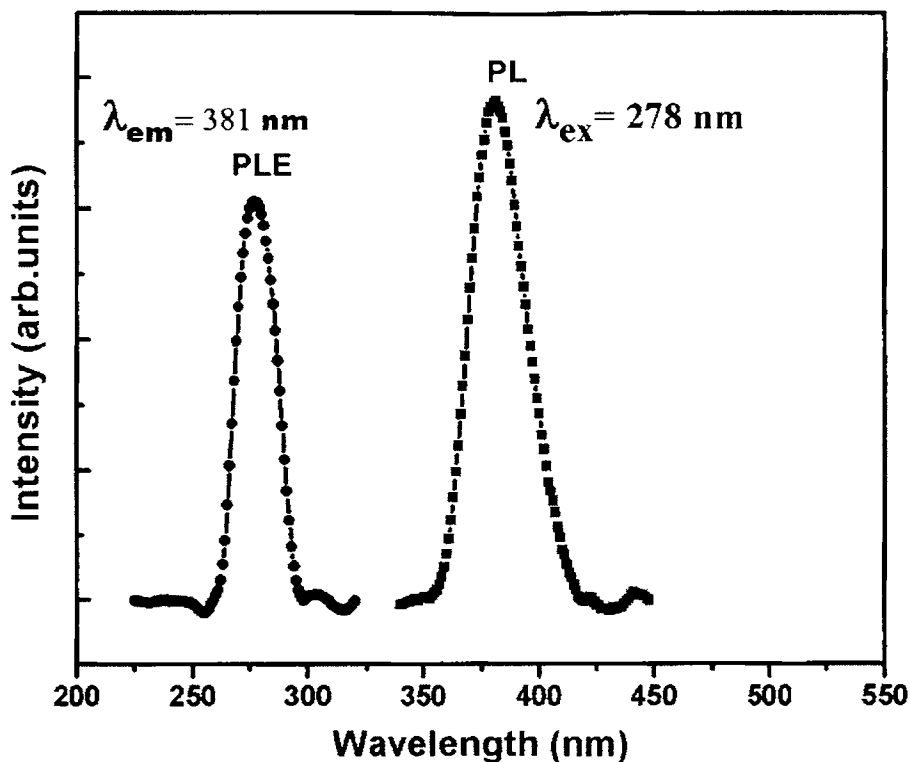


Figure 5.6. PLE and PL spectrum of pure SrS at room temperature.

On doping an additional broad excitation band is observed indicating the existence of centers where absorption starts at longer wavelengths which could be related to defect states (Figure 5.8). Doping by  $\text{DyCl}_3$  introduced many defect levels in SrS host matrix. The Cl<sup>-</sup> can form a donor level just below the conduction band, the density of which increases with the doping concentration of  $\text{Dy}^{3+}$  ions since dysprosium is introduced in the form of  $\text{DyCl}_3$ . In ZnS this level was found at 0.46 eV below the conduction band [15,16]. EPR spectrum confirms the existence of  $\text{F}^+$  centre. The absorption at 385nm may be due to sulphur vacancies since it is also seen in the photoluminescence emission of pure SrS.

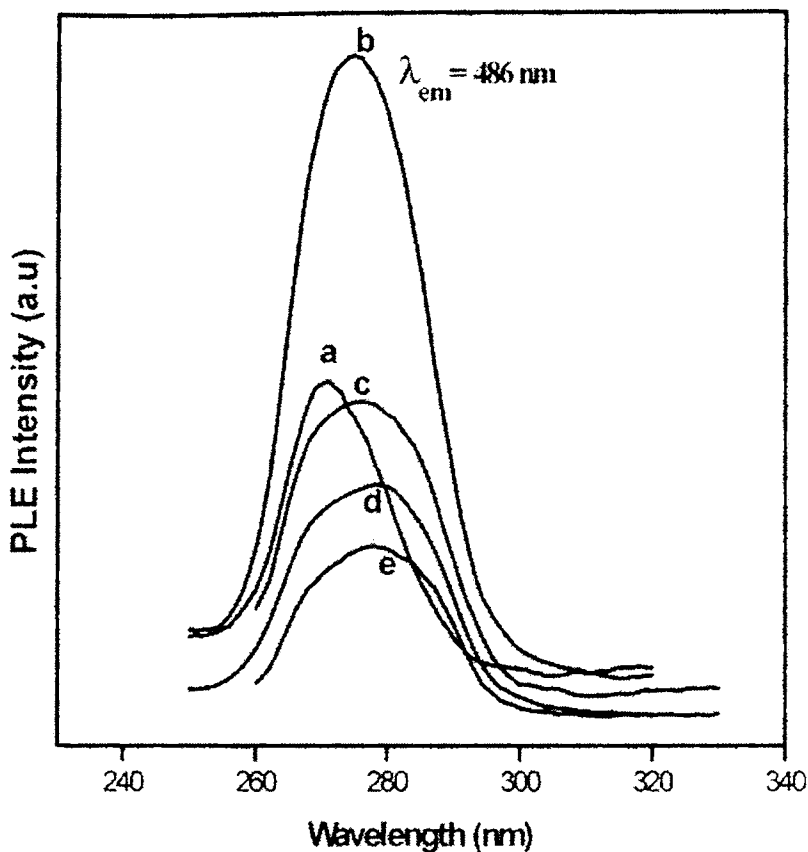


Figure 5.7. PLE spectra of SrS:Dy,Cl phosphor for various doping concentrations,  $\lambda_{em}=486\text{nm}$ : (a). 0.1 at. % (b). 0.25at.% (c). 0.5 at.% (d). 0.75 at.% (e). 1 at%.

Strontium vacancies create an impurity level above the valence band. Impurities will induce tails in the density of states [Figure 5.9] by perturbing the band edge via deformation potential, via coulomb interaction, and by forming a band of impurity states [17]. The line width of near band edge PL excitation broadened with increasing doping concentration which implies

that the impurity states produced due to doping give rise to tail states of band edges resulting in the broadening of the luminescence excitation line. These

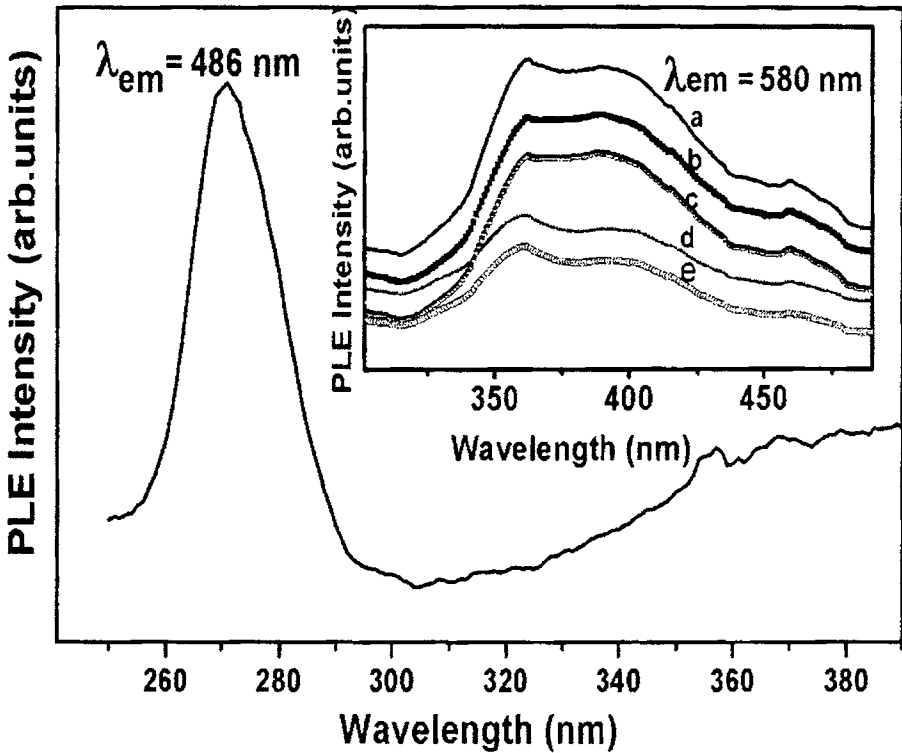


Figure 5.8. PLE spectrum of SrS, Dy:Cl for 0.1 at.% Dy concentration ( $\lambda_{em}=486\text{nm}$ ). Inset shows the PLE spectrum of SrS:Dy,Cl phosphor for various doping concentrations ( $\lambda_{em}=580 \text{ nm}$ .) (a) 0.1 at.% (b) 0.25at.% (c) 0.5 at.% (d) 0.75 at.% (e) 1 at.%.

tail band states cause the gradual red shift in ( $\lambda_{ex}$ ) peak with increase in doping concentration

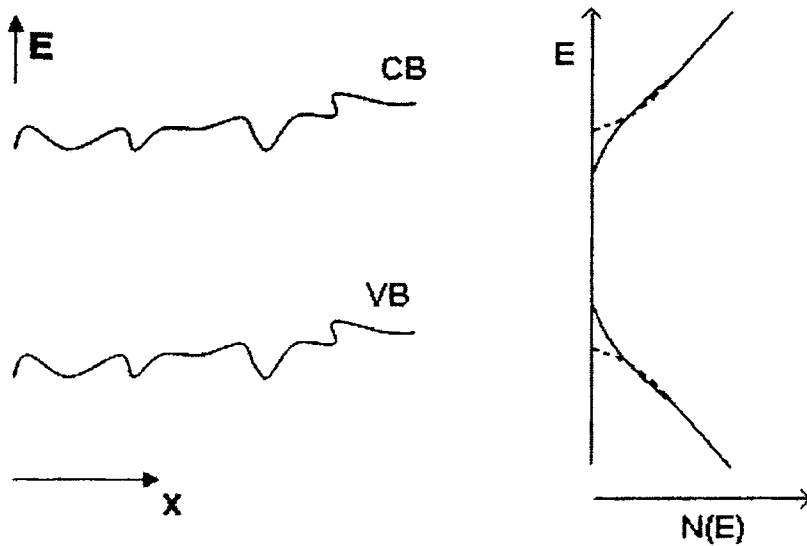


Figure 5.9 Perturbation of band edges by coulomb interaction with inhomogeneously distributed impurities (left). This leads to the formation of tails of states (right). The dashed lines show the distribution of states in the unperturbed case.

### 5.4.5 Diffuse reflectance and conductivity measurements

Figure 5.10 is the plot of  $h\nu$  vs  $\{(k/s)/h\nu\}^2$  obtained from diffuse reflectance spectra of pure SrS powder,  $k$  and  $s$  being the absorption and scattering coefficients respectively. The ratio  $k/s$  was calculated from reflectance spectra via Kubelka – Munk equation [18,19]. The band gap is found to increase with increase of  $Dy^{3+}$  doping concentration. This could be related to the Burstein Moss shift. The optical gap is defined as the minimum energy needed to excite an electron from valance band to conduction band. In pure undoped crystals the optical gap equals the energy separation between the band edges. On heavy doping ( $Dy^{3+}$  and  $Cl^-$ ) the donor electrons occupy

states at the bottom of the conduction band. Since Pauli's principle prevents states that being doubly occupied, the optical band gap is given by energy difference between states with Fermi momentum in the conduction

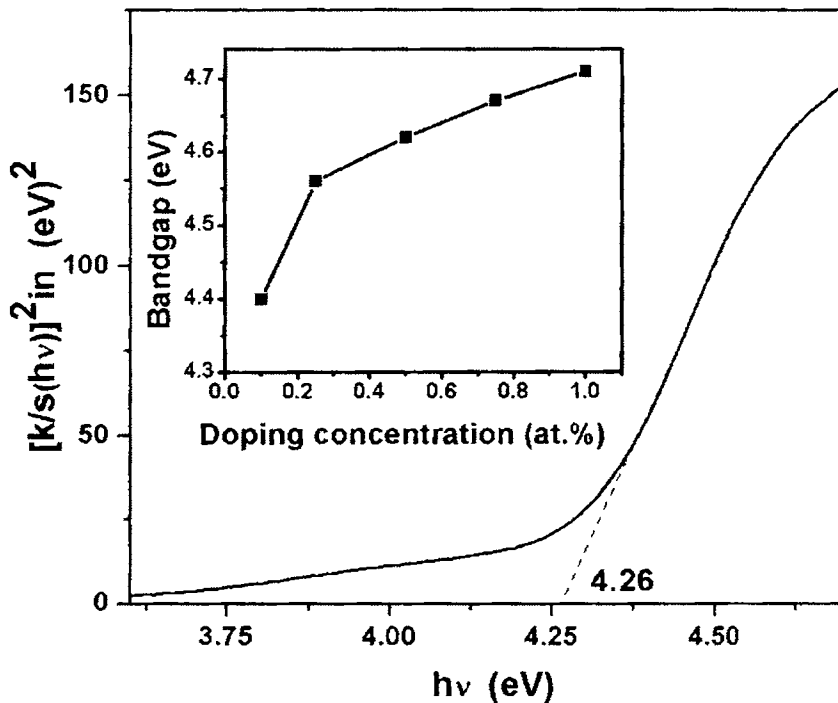


Figure 5.10. Plot of  $((k/s) hv)^2$  vs  $hv$  of undoped SrS. Inset shows variation of bandgap with doping concentration of SrS:Dy,Cl

band and valance band. This type of blocking of low energy transitions is known as Burstein- Moss effect [20,21]. The conductivity of the dysprosium doped SrS samples show an increase in conductivity (Table 5.2). This confirms that there is increase in carrier concentration on increasing the  $Dy^{3+}$  concentration and hence the BM shift.



Table 5.2. Variation of conductivity of SrS with doping concentration

Doping concentration (at.%)	Conductivity $10^{-8} (\text{Scm}^{-1})$
Pure SrS	$7.95 \times 10^{-3}$
0.1	1.78
0.25	7.2
0.5	8.2
0.75	9.5
1.0	11.2

## 5.5 Conclusion

The optical properties of dysprosium doped strontium sulphide powder phosphor for various concentrations have been investigated. Photoluminescence intensity was maximum for a doping concentration of 0.25at.%. The yellow-to-blue intensity ratio of  $\text{Dy}^{3+}$  emission varied since  $\text{Dy}^{3+}$  is nonisovalent with  $\text{Sr}^{2+}$ . Electron paramagnetic resonance spectrum consisted of two signals one due to  $\text{Dy}^{3+}$  ion and other due to  $\text{F}^+$  centre. Room temperature photoluminescence excitation spectra show a monotonic red shift with increasing doping concentration. This is due to the near band edge fluctuations caused by randomly distributed doping impurities. But absorption edges show a blue shift with increasing doping concentration which is due to the Burstein Moss shift.

## 5.6 References

1. A.Y.Cabezas and B.L.Deshazer, *Appl. phys. Lett.* **4** (1964) 37
2. J.Daslot., P.Braunlich and J.P.Fillard., *Appl. Phys. Lett.* **40** (1982) 376.
3. D.A. Davies, J.Silver, A.Vecht, P.JMarsh, and A. Rose, *J. Electrochem.Soc.* **148** (2001)H143.
4. R.N.Dubey, O.N.Awasthi, V.Singh, and M.Tiwari, *Indian J. Pure &Appl. Phys.***40** (2002a) 54.
5. R.N.Dubey, M.S.Qureshi, V.Singh, M.Tiwari, and S.J Dhoble, *Indian J .Phys.***A76** (2002b)591
6. P.D.Keir, C.Maddix, B.A.Baukol, J.F.Wager, B.L.Clark, and D.A.Keszler, *J.Appl. Phys.* **86** (1999) 6810.
7. S.Okamoto and E Nakazawa *Jpn. J. Appl. Phys.* **34** (1995) 521
8. S.Okamoto, E.Nakazawa, and Y.Tsuchiya, *Jpn. J .Appl. Phys* **28** (1989)406
9. V. Singh, M. Tiwari, T.K.GunduRao, and S.J.Dhoble, *Bull. Mater. Sci* **28**(2005)31.
10. P K Ghosh and V. Shankar, *J. Lumin.***20** (1979) 139
11. A.Elizebeth, V.Thomas, G.Jose, N.V.Unnikrishnan, C.Joseph, and M.A Ittyachan, *Cryst. Res .Technol.***39**, (2004) 105
12. Y Kirsh and P D Townsend *J. Phys. C* **20** (1987) 967
13. *Spectroscopy, Luminescence and Radiation Centers in Minerals*, A.S,Marfunin, Translated by V.V. Schiffer, Springer-Verlag,Berlin Heidelberg, New York(1979)
14. Qiang Su, Zhiwu Pei, Lisheng Chi, Hongjie Zhang, Zhongyi Zhang and Feng Zou,*J.of Alloys and Compounds*,**192**(1993)25
15. S.M.Pillai and C.P.G.Vallabhan, *Solid State Commun.* **47** (1982) 909.

16. A.J.Freeman and R.E.Watson, Phys.Rev.**127** (1962) 2058
17. J.I.Pankove, Optical Processes in Semiconductors, Dover publications, Inc.New York (1971)
18. P. Kubelka and F.Munk, Zh. Tekh. Fiz **12** (1931) 593
19. P.Kubelka, J. Opt. Soc. Am. **38** (1948) 448.
20. A.P.Roth, J.B.Webb, and D.F.Williams, Phys. Rev B. **25** (1982) 7836.
21. B.E Sernelius, K.F.Beggren, Z C Jin, I Hamberg, and C.Grangvist, Phys. Rev. B. **37** (1988) 10244.

## CHAPTER SIX

# Sensitised luminescence of SrS: Dy, Cu, Cl phosphor

### 6.1 Abstract

SrS:Dy,Cu,Cl phosphors for fixed Dy concentration and different Cu concentrations were prepared by solid state reaction method. Studies of the structural and optical properties of the samples were carried out. From the analysis of the photoluminescence measurements it was observed that, the excitation in the absorption bands of  $\text{Cu}^+$  ion leads to transfer of energy to  $\text{Dy}^{3+}$  ion thereby enhancing the intensity of its luminescence.

### 6.2 Introduction

More recently intensive research is going on in developing phosphors for use in light emitting devices such as electroluminescent (EL) devices, plasma display panels (PDP), and vacuum fluorescent displays (VFD). The increasing demand of phosphors for wide applications has created interest in the study of spectroscopic properties, defects and energy transfer processes in phosphors due to doping with different materials. Alkaline earth sulphide phosphors especially strontium sulphide is considered as a potential host for phosphor applications. SrS:Cu was first reported as a potential blue electroluminescent emitter by Kane et al. [1]. The two component SrS:Cu,Ag phosphor has been shown to exhibit an efficient blue colour, due

to the efficient energy transfer from Cu to Ag [2]. SrS:Dy based electroluminescent devices were found to give a yellow emission [3,4]. In SrS:Ce,Dy the emission intensity of Dy<sup>3+</sup> ion increases due to energy transfer from one activator to another [5]. Although considerable attention has been paid to the study of SrS phosphors activated with dysprosium or copper, very few or little quantitative data are available relating to the properties of two component SrS phosphors activated with copper and dysprosium. In this chapter the structural and luminescence properties of SrS:Cu,Dy,Cl phosphor are presented.

### 6.3 Experimental

The phosphor samples for the present study were prepared from starting materials, strontium sulphide, copper chloride (CuCl<sub>2</sub>) and dysprosium chloride (DyCl<sub>3</sub>) by solid state reaction. Required proportions of copper chloride and dysprosium chloride were mixed with strontium sulphide and 5wt. % of ammonium chloride in ethanol medium. The mixture, after drying in an oven, was fired in H<sub>2</sub>S atmosphere at 850<sup>0</sup>C for two hours. Different samples were prepared with different copper concentrations (0.01at. % to 0.2 at. %) for the same dysprosium (0.25 at.%) concentration. The structural and optical characterizations of these samples were then performed. The crystal structures of the synthesized phosphors were studied using a Rigaku X-ray diffractometer with Cu K $\alpha$  x-ray. The PL and PLE spectra were recorded with Jobin Yvon Fluoromax-3 Flourimeter. The absorption spectra of the samples were recorded with Jasco-V-570 uv-vis-nir spectrophotometer.

## 6.4 Results and discussion

The crystallinity, lattice strain and crystallite size of the samples were analyzed from the X-ray diffraction patterns. Spectra of all the samples closely matched the JCPDS file no.8-489 for cubic SrS without any traces of impurities (Figure 6.1). Copper and dysprosium enters and replaces  $\text{Sr}^{2+}$  ion in the SrS lattice as  $\text{Cu}^+$  and  $\text{Dy}^{3+}$  ions. The ionic radii of  $\text{Sr}^{2+}$ ,  $\text{Cu}^+$ , and  $\text{Dy}^{3+}$  are  $1.12\text{\AA}$ ,  $0.77\text{\AA}$  and  $1.05\text{\AA}$  respectively.

Discrepancies between the activator ion and the host cation lead to lattice strain induced defects, poor crystallinity, and device stability problems. The grain size and lattice strain of the different samples were evaluated from the graph between  $\text{Brcos}\theta$  and  $\sin\theta$  where Br is the full width at half maximum values in radians of X ray diffraction peaks and ' $\theta$ ' is the diffraction angle[6]. The lattice parameter of the samples were calculated using the formula  $a = \lambda(h^2+k^2+l^2)^{1/2}/2\sin\theta$ , where  $\lambda$  is the x-ray wavelength; h, k and l are the Miller indices and  $\theta$  is the Bragg angle. These values are tabulated in table 6.1. The strain in the SrS host lattice increase with doping concentration of Cu whereas the lattice parameter and grain size show a random variation.

The absorption spectra of  $\text{SrS}:\text{Cu}_x,\text{Dy}$  (.25at.%) for three different Cu concentrations are shown in figure 6.2. The absorption spectra of two different ions concurrently present in a crystal are simply a superposition of each of their absorption spectra.

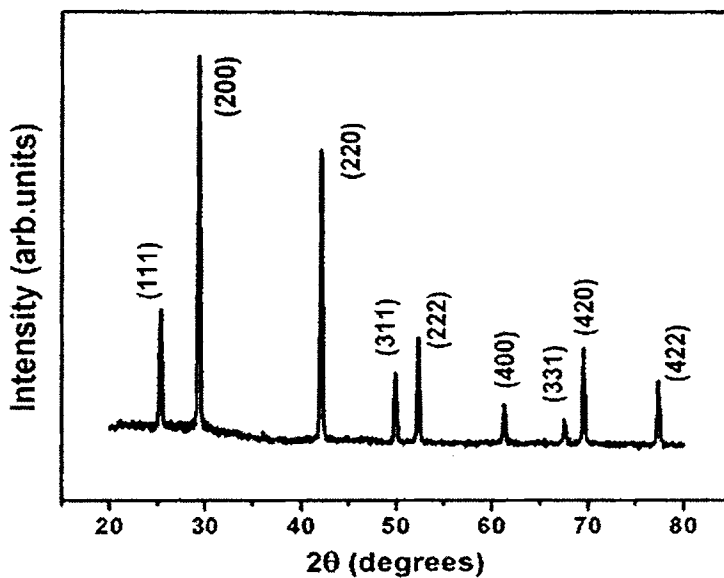


Figure 6.1. X ray diffraction pattern of SrS: Dy,Cu, Cl phosphor.

Table.6.1. Table illustrating the lattice parameter, grain size and lattice strain of different SrS:Cu,Dy,Cl samples.

Copper doping concentration (at.%) Dy = 0.25 at.%	Lattice parameter. (nm)	Grain size (nm)	Lattice strain ( $\times 10^{-3}$ )
0.01	0.6066	28.5	1.25
0.05	0.6054	29.34	1.28
0.1	0.604	26	1.95
0.15	0.6067	37.2	2.37
0.2	0.605	33.12	2.85

Three absorption peaks around 260nm, 280nm and 320nm are observed. 260nm peak corresponds to absorption in the host lattice, whereas 280nm and 320nm peaks correspond to intracenter absorption in  $\text{Cu}^-$  levels in octahedral crystal field. In the sample with least doping concentration of Cu (0.01at.%), absorption at 280nm is absent and host lattice absorption has maximum intensity. The high energy absorption in  $\text{Cu}^+$  at 280nm appears for a doping concentration of 0.05at.% and it has maximum intensity of the three absorption peaks. On increasing Cu doping further, the absorption at 320nm dominates.

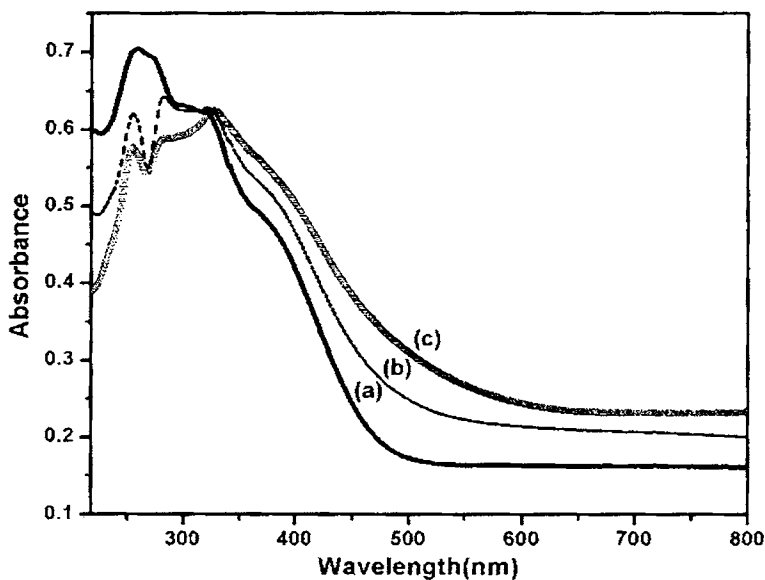
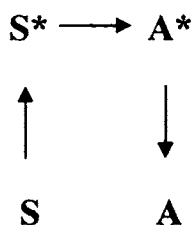


Figure 6.2. Absorption spectra of SrS: Dy, Cu, Cl phosphor samples for Dy concentration=0.25at.% and various Cu concentrations (a). 0.01at.% (b). 0.05at.% and (c). 0.2at.%

In the emission spectra of phosphor with two activators, either the position of emission lines of each of them does not change in the presence of the other, i.e. superposition of emission spectra from two ions occur, or the



luminescence spectrum intensity of one ion gain in strength at the expense of the diminishing intensity of the other.



Here S is the sensitizer (energy donor); A is the activator (energy acceptor); asterisks denote their excited states.

These changes in luminescence from one ion in the presence of the other are due to transfer of excitation energy from one to the other. Luminescence of ions excited as a result of the energy transfer from other ions excited in the absorption band is termed sensitized luminescence.

The transfer of energy from sensitizer to activator is accomplished through the following three main types of transfer - (1) emission - reabsorption, (2) resonance radiationless and (3) the nonresonance radiationless. The resonance radiationless mechanism of energy transfer is effected between interacting ions behaving like a single system. A condition necessary for this mechanism of transfer to show itself is coincidence or a close distance between energy level pairs of the ion sensitizer and the ion activator. Sensitization can be accomplished with the help of admixture ions (impurity sensitization), or with the aid of ions entering the composition of the crystal itself (lattice sensitization). Since trivalent rare earth ( $RE^{3+}$ ) activators are

devoid of intense absorption bands, impurity sensitization is of greatest importance [7].

$\text{Cu}^+$  ion have strong absorption bands in the UV region and display emission bands in the near-neighboring UV and visible region. In  $\text{SrS:Dy,Cu,Cl}$  phosphor energy transfer is by resonance radiationless mechanism where  $\text{Dy}^{3+}$  plays the role of activator and  $\text{Cu}^+$  that of sensitizer. Excitation in the absorption bands of  $\text{Cu}^+$  ions leads to transfer of energy to  $\text{Dy}^{3+}$  ion. Figure 6.3 demonstrates the sensitizing behaviour of  $\text{Cu}^+$  in  $\text{SrS:Cu,Dy,Cl}$  phosphor.

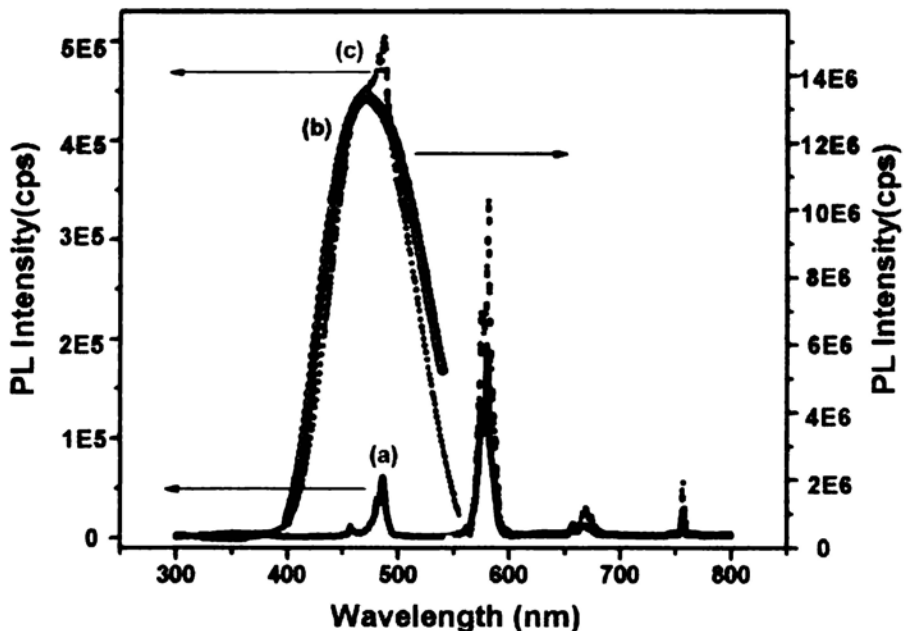


Figure 6.3. PL spectra of (a).  $\text{SrS:Dy}$  (0.25at.%), Cl phosphor,  $\lambda_{\text{ex}}=274$  nm, (b).  $\text{SrS:Cu}$  (0.2at.%), Cl phosphor,  $\lambda_{\text{ex}}=280$  nm and (c).  $\text{SrS:Dy}$  (0.25at.%),  $\text{Cu}$  (0.2at.%), Cl phosphor,  $\lambda_{\text{ex}}=280$  nm.

In figure 6.3, (a) represents the PL spectrum of SrS activated with Dy at an excitation wavelength of 274 nm.  $\text{Dy}^{3+}$  luminescent centre is excited via the energy transfer from the host matrix and the two main luminescence peaks are at 486nm and 581nm ( ${}^4\text{F}_{9/2} \rightarrow {}^6\text{H}_{15/2}$  and  ${}^6\text{H}_{13/2}$ ) [8]. The resultant of PL emission from the sample was yellow with chromaticity coordinates  $x=0.40$ ,  $y = 0.42$ . Figure 6.3.(b) is the PL spectrum of copper activated strontium sulphide phosphor. The excitation was given at 280nm which is one of the intracenter excitation ( ${}^1\text{A}_{1g} \rightarrow {}^1\text{T}_{2g}$ ) in  $\text{Cu}^+$  ion in octahedral crystal field [9]. The broad emission obtained was blue in colour peaking at 471 nm. Blue luminescence in SrS:Cu is produced by  $[\text{Cu}^+_{\text{Sr}}]^-$  centers with coordination number 6 whereas  $[\text{Cu}^+_{\text{Sr}}]^-$  centers with coordination number 5 give rise to green luminescence [10]. In SrS:Dy,Cu,Cl phosphor also excitation is through the  $\text{Cu}^+$  center at 280nm and 320nm. But the luminescence from this two component phosphor is not just a superposition of emissions from  $\text{Cu}^+$  and  $\text{Dy}^{3+}$  centers.

In the SrS:Dy,Cu,Cl two component phosphor the intensity of blue emission in  $\text{Cu}^+$  center at 471nm was  $(1/30)^{\text{th}}$  of it's value for the sample doped with same concentration of copper alone. But the intensity of emission lines at 486 nm and 581nm from  $\text{Dy}^{3+}$  became 8 times and twice respectively on codoping with copper. The resultant emission is bluish white with chromaticity coordinates  $x = 0.19$  and  $y = 0.27$ . Figure 6.4 demonstrates the resonance radiationless mechanism of energy transfer from  $\text{Cu}^+$  to  $\text{Dy}^{3+}$ . The energy transfer from  $\text{Cu}^+$  to  $\text{Dy}^{3+}$  does not proceed directly from the absorption band ( ${}^1\text{T}_{2g}$  and  ${}^1\text{E}_g$ ) of  $\text{Cu}^+$ , but there first occurs a rapid radiationless transition to  ${}^3\text{E}_g$  and only from this the energy is transferred to  ${}^4\text{F}_{9/2}$  of  $\text{Dy}^{3+}$ .

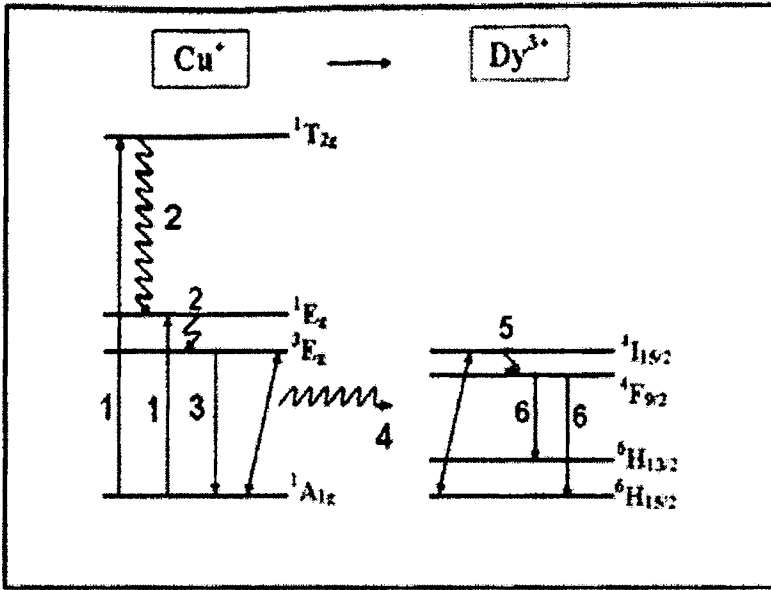


Figure 6.4. Resonance radiationless transfer of energy from  $\text{Cu}^+$  to  $\text{Dy}^{3+}$ . 1 denotes excitation in  $\text{Cu}^+$  absorption bands; 2- radiationless transitions in  $\text{Cu}^+$  ion; 3-normal  $\text{Cu}^+$  ion luminescence; 4-energy transfer from  $\text{Cu}^+$  to  $\text{Dy}^{3+}$ ; 5-radiationless transition in  $\text{Dy}^{3+}$  ion; and 6-sensitized luminescence of  $\text{Dy}^{3+}$

Photoluminescence excitation spectra of three samples are shown in figure 6.5 for comparison. Spectrum (a) peaking at 274nm is the PLE spectrum of Dy doped sample. It corresponds to near band edge absorption in host lattice. Spectrum (b) demonstrates the excitation in  $\text{SrS:Dy,Cu,Cl}$  sensitised phosphor and (c) that in copper doped  $\text{SrS}$ . The two bands located at 284nm and 320nm in (c) are due to the transitions  $^1A_{1g} \rightarrow ^1T_{2g}$  and  $^1A_{1g} \rightarrow ^1E_g$  in  $\text{Cu}^+$  [11]. In (c) these bands undergo a slight shift towards lower energy.

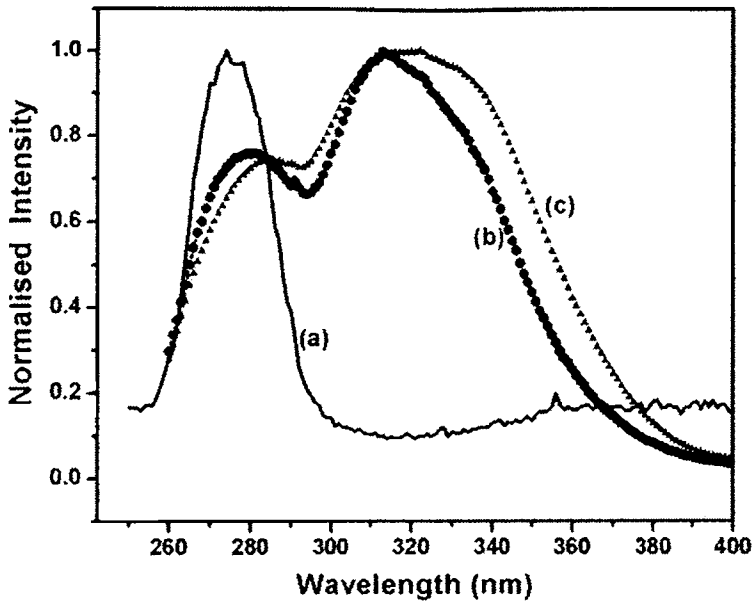


Figure 6.5. PLE spectra of (a). SrS:Dy (0.25at.%),Cl phosphor,  $\lambda_{em}=486$  nm  
 (b). SrS:Dy (0.25at.%), Cu(0.2at.%), Cl phosphor,  $\lambda_{em}=486$  nm. ,(c). SrS:Cu  
 (0.2at.%),Cl phosphor,  $\lambda_{em} = 471$  nm.

This may be due to the presence of additional impurity ( $Dy^{3+}$ ) which change the crystal field and hence the separation between  ${}^1A_{1g}$ ,  ${}^1T_{2g}$  and  ${}^1E_g$  levels of  $Cu^+$ .

The photoluminescence from SrS:Dy,Cu,Cl phosphor for various concentrations of Cu (0.01at.%,0.05at.%,0.1at.%,0.15at.% and 0.2at.%) keeping the concentration of Dy at 0.25at.% were also studied. One broad blue emission at 471nm due to  $Cu^+$  and another blue emission at 486nm due to  $Dy^{3+}$  were observed. The yellow emission line was at 581nm with a shoulder peak at 574 nm. The resultant emission was found to vary from bluish white to white which is demonstrated by CIE chromaticity

diagram(Fig.6.6). For 0.01at.% doping of Cu the luminescence of the sensitised phosphor was white with chromaticity coordinates  $x = 0.37$  and  $y = 0.37$ .

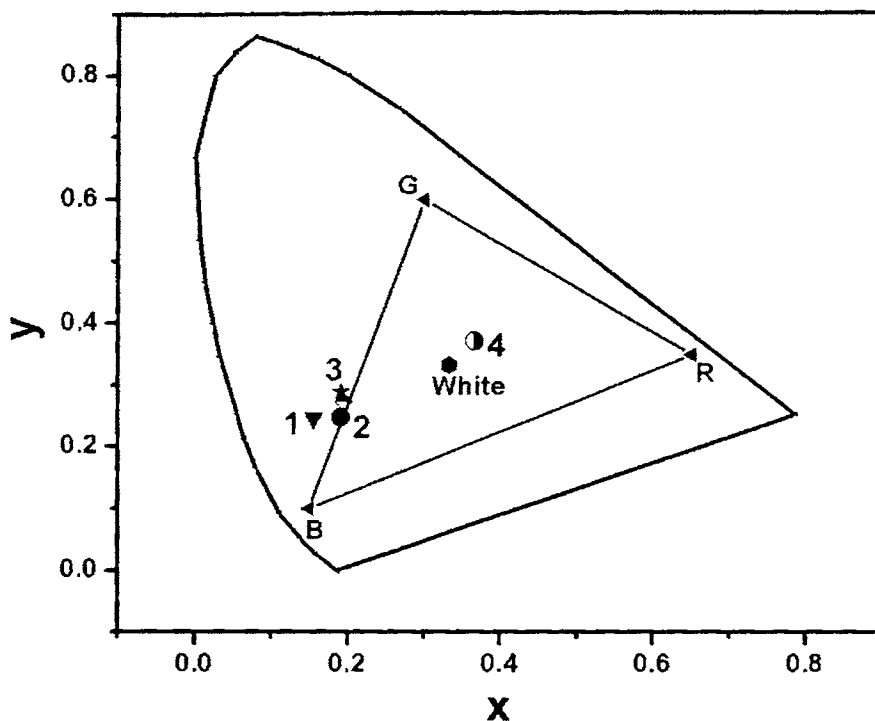


Figure 6.6.CIE chromaticity diagram for SrS:Dy,Cu,Cl sensitised phosphor samples with Dy concentration 0.25at.% and various Cu concentrations.

(1). 0.05at.%, (2). 0.1at. %, (3). 0.15at. % and 0.2at. % and (4). 0.01at. %.

## 6.5 Conclusion

A model is proposed demonstrating the sensitizing behaviour of  $\text{Cu}^+$  ion in SrS:Dy,Cu,Cl phosphor. Energy is transferred from  $^3E_g$  of  $\text{Cu}^+$  to  $^4F_{9/2}$  of  $\text{Dy}^{3+}$ . Resultant emission colour from the samples vary with the variation in doping concentration of Cu.

## 6.6 References

1. J.Kane, W.Harty, M.Ling, P.N.Yocom, SID'85 Digest, SID, Santa Ana 1985, 163
2. W.Park, T.C.Jones and C.J.Summers; *Appl.Phys.Lett.* **74** (1999)1785
3. S.Okamoto, E.Nakazawa and Y.Tsuchiya; *Jpn.J.Appl.Phys.* **28** (1989)406
4. P.D.Keir, C.Maddix, B.A.Baukol, J.F.Wager, B.L.Clark and D.A.Keszler; *J.Appl.Phys.* **86**(1999)6810
5. V.Singh, M.Tiwari, T.K.Gundu Rao and S.J.Dhoble; *Bull.Mater.Sci.* **28**(2005)31
6. X-Ray Diffraction – a practical approach, C.Suryanarayana and M.Grant Norton, Plenum Press, New York and London (1998).
7. Spectroscopy, Luminescence and Radiation Centers in Minerals, A.S.Marfunin, translated by V.V.Schiffer, Springer-Verlag, Berlin Heidelberg, New York (1979)
8. E.I.Anila and M.K.Jayaraj, *Mater.Res.Bull.*(communicated)
9. J.Ihanus, M.Ritala, M.Leskela, W.Park, A.E.kaloyeros, W. Harris, K.W.Barth, A.W.Topol, *J.Appl.Phys.* **94** (2003) 3862
10. P.D.Keir, J.F.Wager, B.L.Clark, D.Li and D.A.Keszler, *J.Appl.phys.* **75** (1999)1398
11. N.Yamashita, *Jpn.J.Appl.Phys.*, **30** (1991) 3335

## CHAPTER SEVEN

# Low temperature fabrication of SrS:Cu,F ACTFEL device by electron beam evaporation

### 7.1 Abstract

The deposition of highly stoichiometric SrS:Cu,F films and fabrication of a multilayer ACTFEL device based on it is presented. The device exhibited bluish white EL emission with chromaticity coordinates  $x = 0.25$ ,  $y = 0.27$  and low threshold voltage.

### 7.2 Introduction

To replicate full colour performance of a cathode ray tube, efficient EL active red, green and blue phosphors having specific emission colour must be available. The prospects for production of a full-colour EL display have brightened considerably following the discovery and efficient operation of the blue emitting phosphor SrS:Cu and its modifications[1]. For SrS based EL devices the phosphor layer is deposited at substrate temperatures 400<sup>0</sup>C-600<sup>0</sup>C and sulphur co evaporation to realize stoichiometric films[2,3]. For the films deposited at low temperatures post deposition annealing should be performed at high temperatures in the range 650<sup>0</sup>C-850<sup>0</sup>C[4-8].

We report a new method of deposition of SrS:Cu,F films at a substrate temperature 380<sup>0</sup>C without sulphur co evaporation and post deposition annealing. This was carried out via EB/thermal multi-source evaporation.



## 7.3 Experimental

Strontium sulphide pellets for evaporation were prepared by pressing the mixed powder of SrS, polyvinyl alcohol (PVA) and 5wt. % of  $\text{NH}_4\text{Cl}$ , by applying a pressure of 4 tonnes. This pellet was sintered at a ramp rate of  $3^\circ\text{C}/\text{minute}$  to  $850^\circ\text{C}$  and then holding the temperature at  $850^\circ\text{C}$  for two hours. The source material for activator was 99.9% pure  $\text{CuF}_2$  which was evaporated from an alumina crucible heated with a tungsten wire heater. The sintered SrS pellets were electron beam evaporated while  $\text{CuF}_2$  was thermally evaporated yielding SrS:Cu,F film. Before opening the shutter the chamber was purged with thermally evaporated sulphur from the crucible containing the activator.

Figure 7.1 shows the structure of EL device fabricated. The substrate used was glass coated with indium tin oxide (ITO) and aluminium titanium oxide (ATO) supplied by Planar. The Zinc sulphide buffer layers each of thickness  $\sim 150$  nm were deposited by EB evaporation at a substrate temperature of  $150^\circ\text{C}$ . The  $\text{Y}_2\text{O}_3$  top insulating layer was also grown by EB evaporation at  $200^\circ\text{C}$  with a thickness  $\sim 200$ nm. The thickness of the phosphor layer was  $\sim 700$  nm. The chamber vacuum prior to evaporation was  $5 \times 10^{-6}$  mbar and the temperature of the glass substrate was  $380^\circ\text{C}$ . The crystallinity of the films were analysed by x-ray diffraction (XRD) using a Rigaku x-ray diffractometer with  $\text{Cu K}\alpha$  x-ray. The PL and PLE spectra were recorded with Jobin Yvon Fluoromax-3 Fluorimeter. The optical band gap of pure SrS was estimated from the transmission spectra recorded with Jasco-V-570 uv-vis-nir spectrophotometer. The surface roughness of the samples were estimated by atomic force microscopy (AFM). Inductively coupled plasma-atomic emission spectroscopy (ICP-AES) was performed to determine the

chemical composition of pure SrS powder. A 0.32 m monochromator (Triax-320) coupled with Hamamatsu R928 photomultiplier tube was used to record the electroluminescent output from the fabricated device. Thickness of the samples were measured by using stylus thickness profiler.

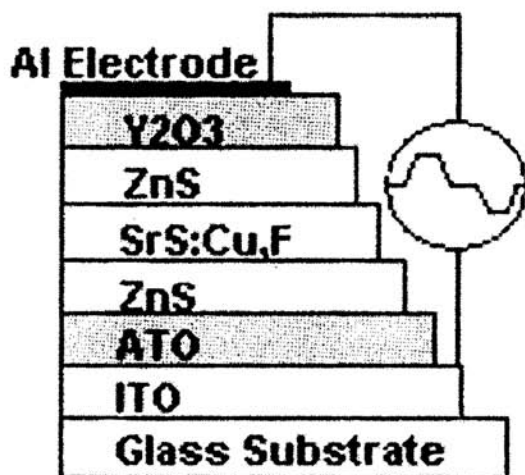


Figure 7.1: Structure of the SrS:Cu,F multilayer ACTFEL device

## 7.4 Results and discussion

X-ray diffraction patterns of SrS:Cu,F thin film and the device are shown in figure 7.2. Polycrystalline film of SrS:Cu,F with reflections matching with JCPDS file no.8-489 for cubic SrS was obtained. In the x-ray diffraction pattern of the device only reflections from ITO and SrS were observed. No reflection was observed for ZnS possibly because it may be too thin and intensity may be weak. To confirm this a 600nm thick film of ZnS was electron beam evaporated on a glass substrate at 150°C. The x-ray diffraction pattern of this film shows the growth of ZnS in cubic phase (figure 7.3).

Similarly a 500nm thick film of  $Y_2O_3$  was electron beam evaporated on glass substrate at  $200^{\circ}C$  and it was found to be amorphous from XRD analysis. No diffraction peaks were observed for ATO also as in the substrate since this layer was amorphous.

Because of the high field nature of the thin film EL device ,it is desirable to have a smooth interface between the various film layers. Any asperity will lead to a high field region that may lead to localized breakdown of the device structure. Therefore it is preferable to have either a fine grained insulating layer morphology or even better an amorphous structure. The amorphous structure leads to better device stability by eliminating possible grain boundary diffusion paths for ions or moisture.

Figure 7.4 is the typical AFM images of SrS:Cu,F thin film with a thickness of 700nm. Large grain size is necessary to permit the electric field to accelerate electrons to high energies before they are scattered at grain boundaries [9]. From the AFM images the samples were observed to contain a continuous network of flat areas with a root mean square (rms) surface roughness  $< 10nm$ , having heights exceeding 100nm in many places.

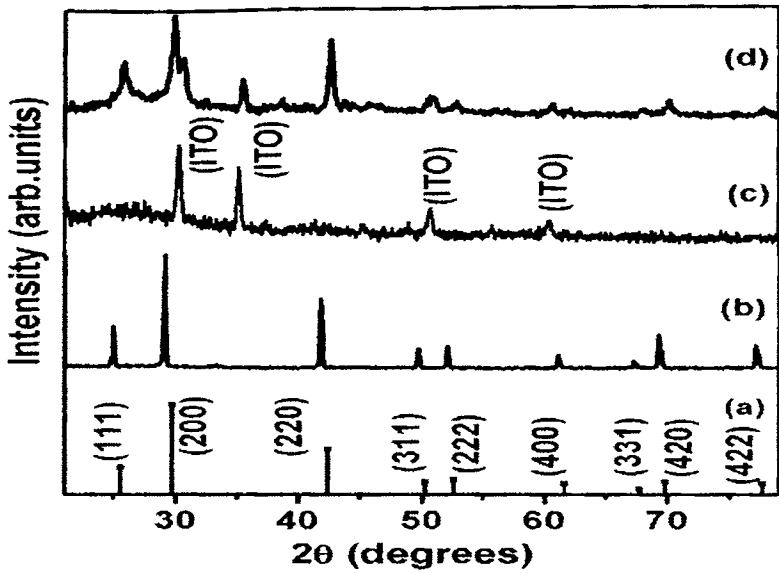


Figure 7.2 (a). Plot of JCPDS data of pure SrS and x-ray diffraction patterns of (b). SrS:Cu,F thin film, (c). glass/ITO/ATO substrate and (d). SrS:Cu,F multilayer device.

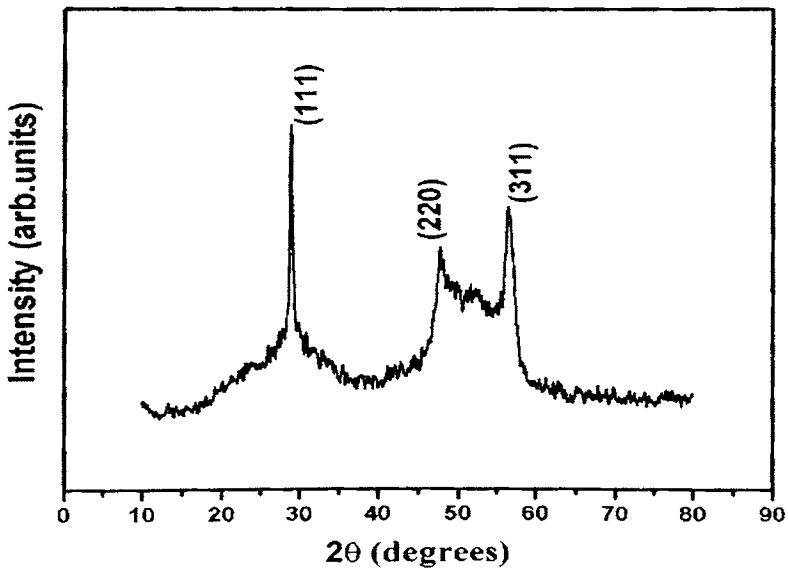


Figure 7.3. X-ray diffraction pattern of ZnS film on glass substrate deposited at 150°C

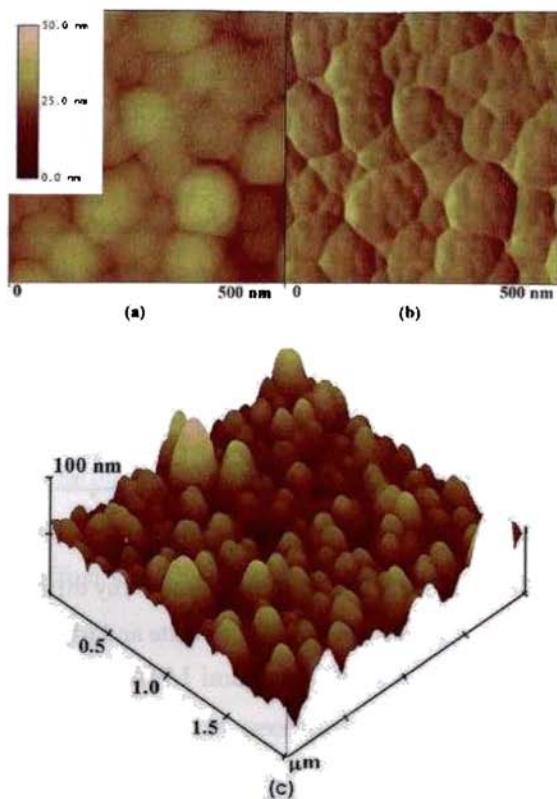


Figure 7.4. AFM images of SrS:Cu,F thin film, (a). top view, (b). lateral view and (c). three dimensional AFM image

To evaluate the band gap of SrS, pure SrS was coated on a glass substrate at a substrate temperature  $380^{\circ}\text{C}$  after purging the chamber with sulphur. Crystalline growth was confirmed by XRD. Figure 7.5 shows the transmission of undoped SrS thin film which exhibited a transmission  $>85\%$  in the visible region. The absorption coefficient  $\alpha$  was evaluated using the measured value of thickness 't' using the relation  $I = I_0 e^{-\alpha t}$ . The optical absorption coefficient ' $\alpha$ ' near the absorption edge is given by  $\alpha \propto A (h\nu - E_{\text{op}})^{1/2} / h\nu$ . The direct band gap of SrS thin film was estimated by plotting  $(\alpha h\nu)^2$  vs.  $h\nu$  and extrapolating the linear portion near the onset of

absorption edge to the energy axis. A typical  $(\alpha h\nu)^2$  vs.  $h\nu$  plot of SrS film is shown in the inset of figure 7.5

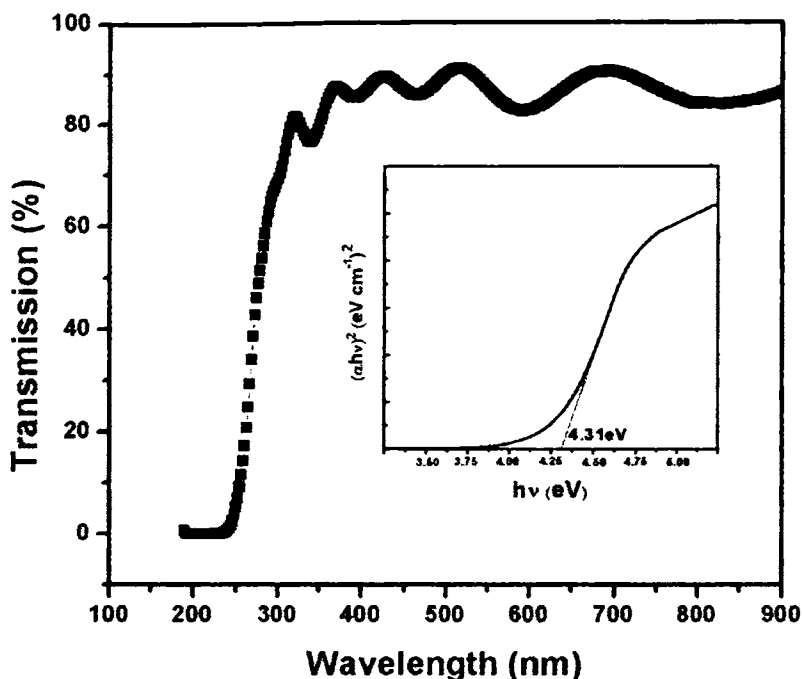


Figure 7.5. Transmission spectrum of undoped SrS .Inset shows the  $(\alpha h\nu)^2$  vs.  $h\nu$  plot of SrS film.

SrS:Cu,F thin film was deposited on glass substrate at  $380^{\circ}\text{C}$  by electron beam evaporation after purging the chamber with sulphur. X ray diffraction (figure 7.2) and photoluminescence measurements of the film were (figure 7.6) recorded. The PL spectrum of SrS:Cu,F thin film had to bands one main band centered at 535nm and another weak but broad band peaked at 435nm. The emission at 535nm is due to the  $3d^9 4s^1 (^3E_g) \rightarrow 3d^{10} (^1A_{1g})$  [10] transition of the  $\text{Cu}^+$  isolated ions in octahedral symmetry environment. The  $3d^{10} \rightarrow 3d^9 4s^1$  electronic transitions are parity- and J-forbidden in the free  $\text{Cu}^+$  ion. In SrS lattice, the selection rules forbidding the transitions are relaxed

by several factors. The first factor is electron-lattice interactions which make this transition partially allowed. The second factor is the off-center position of Cu<sup>+</sup> ions which relaxes the forbidding selection rules of the inversion symmetry by lowering the symmetry of Cu<sup>+</sup> centers. The off-center position of Cu<sup>+</sup> ions refers to the shift of Cu<sup>+</sup> ions substituting for Sr in SrS lattice from the exact Sr position. This is possible because ionic radius of Cu<sup>+</sup> ions (0.77Å<sup>0</sup>) [10] is significantly smaller than Sr<sup>2+</sup> ions (1.18Å<sup>0</sup>) and has space available to be loosely bound on the cation site. The broad emission band at 435nm can be ascribed to donor acceptor recombination.

The photoluminescence excitation spectrum of SrS:Cu,F thin film monitored at an emission wavelength 535nm, contained a broad band peaked at 320nm which is ascribed to <sup>1</sup>A<sub>1g</sub> → <sup>1</sup>E<sub>g</sub> transition in Cu<sup>+</sup> centers.

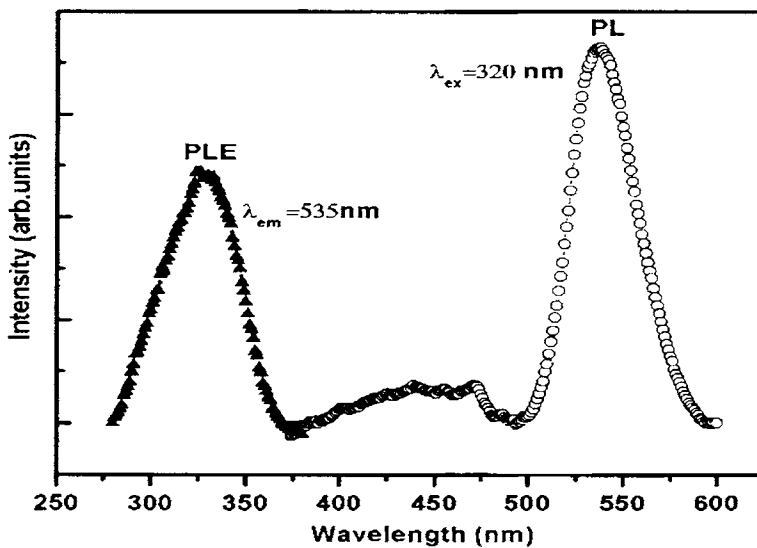


Figure 7.6. The photoluminescence spectrum of SrS:Cu,F thin film deposited at 380<sup>0</sup>C on glass substrate

The photoluminescence and electroluminescence spectra of SrS,Cu ACTFEL device are shown in figure 7.7. PL emission from the device structure under excitation with 320nm consisted of two main peaks, one at 380 nm and other at 434 nm. The less intense broad emission at 435nm observed in SrS:Cu,F thin film appeared as two resolved peaks in the device at 380nm and 435nm. Li et al. reported a PL emission peak at 440 nm for SrS:Cu film which was assigned to donor acceptor recombination [11]. The peak at 380nm was also present in the host SrS which is thought to be due to sulphur vacancies (Fig.7.8). From the AES analysis sulphur to strontium ratio of the SrS powder was found to be 0.78.

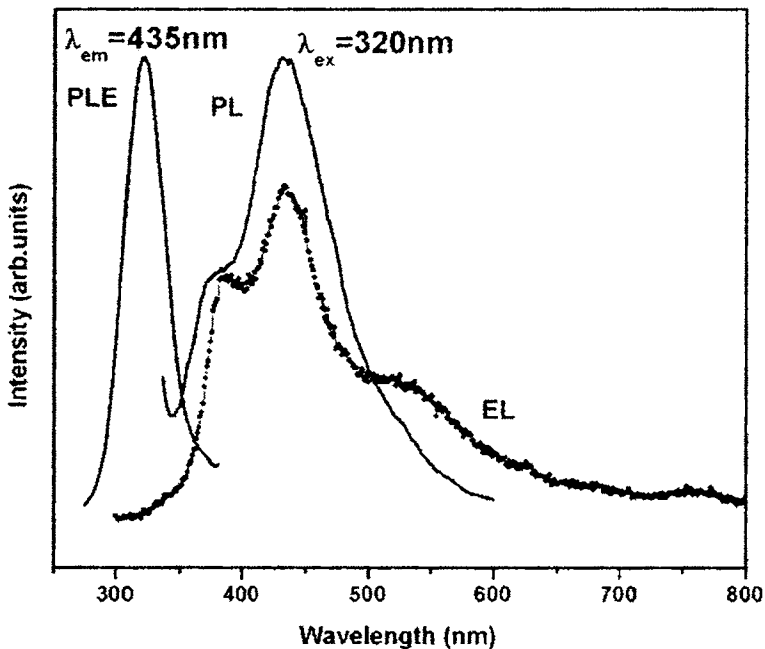


Figure 7.7. Photoluminescence and electroluminescence spectra of SrS:Cu,F multilayer device



Electroluminescence spectrum consisted of an additional broad emission centered at 535nm. This arises due to aggregated copper pairs or  $[\text{Cu}^+_{\text{Sr}}]^-$  centers with coordination number 5 [12,13].

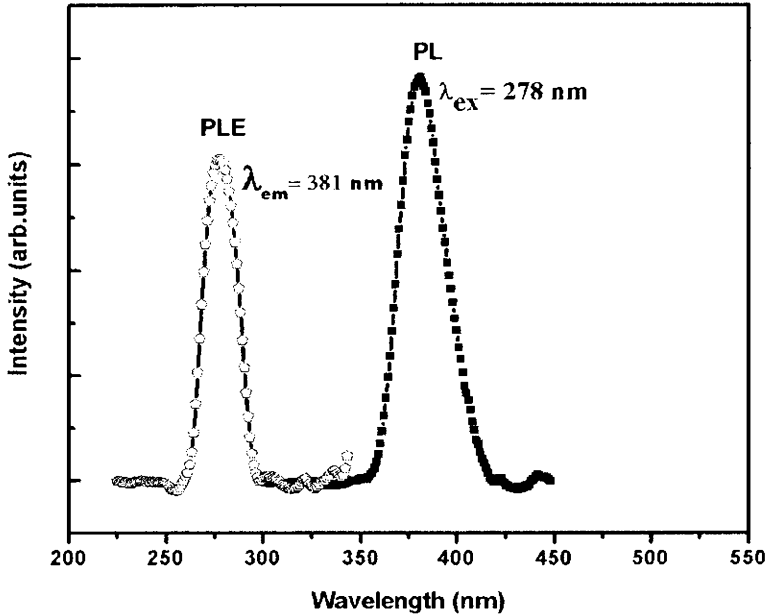


Figure 7.8. PLE and PL spectra of pure SrS at room temperature.

The luminescence mechanism in the device can be explained using the model shown in figure 7.9. Cu enters the SrS lattice as an acceptor that is single negatively charged in equilibrium.

Sulphur vacancies which are double donors are formed at 1.09eV below the conduction band. Excitation in the device takes place via  $^1A_{1g} \rightarrow ^1E_g$  transition in  $\text{Cu}^+$  centers. The low energy emission band at 535nm is due to transition

in  $\text{Cu}^+$  levels whereas the other two emission bands (380nm and 435nm) are from the sulphur vacancies to  $[\text{Cu}_{\text{Sr}}]^-$  and valence band. It has been suggested that a recombination process similar to the well known ZnS:Cu mechanism could also be valid for the copper doped alkaline earth sulphides [14,15]. All the layers were coated in vacuum. This might have aided the formation of more sulphur vacancies in the film thereby enhancing the intensity of high energy bands in the device than in the SrS:Cu,F thin film.

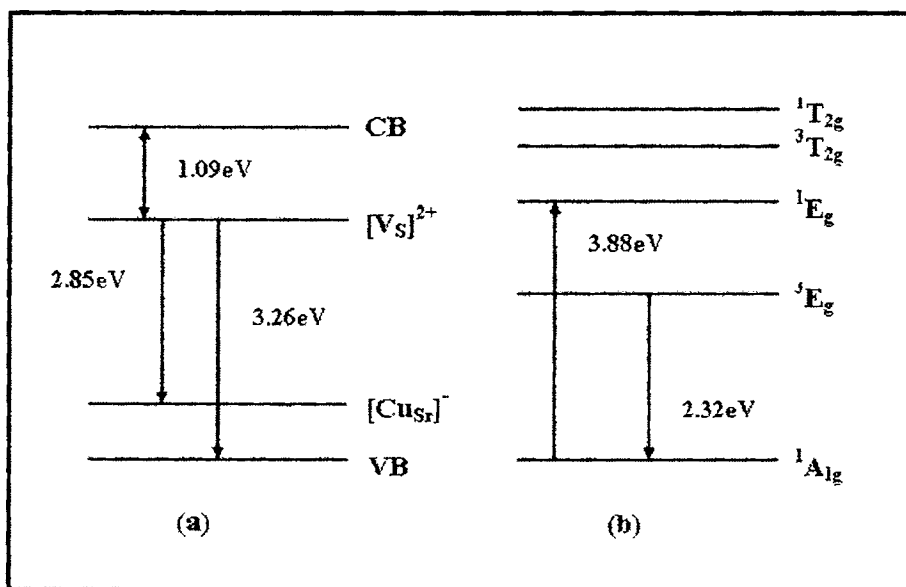


Figure 7.9. Schematic energy levels of (a) Cu doped SrS and (b)  $\text{Cu}^+$  ion in the crystal field with octahedral symmetry.

The device gave a blue PL emission with CIE coordinates  $x=0.18$  and  $y=0.17$  at an excitation wavelength of 320nm where as the EL emission was bluish white with CIE coordinates  $x=0.25$  and  $y=0.27$  [Fig.7.10]. This is due

to the additional broad emission centered at 535 nm in the EL spectrum. There are reports of whitish blue EL emission from SrS:Cu thin film electroluminescent devices [16].

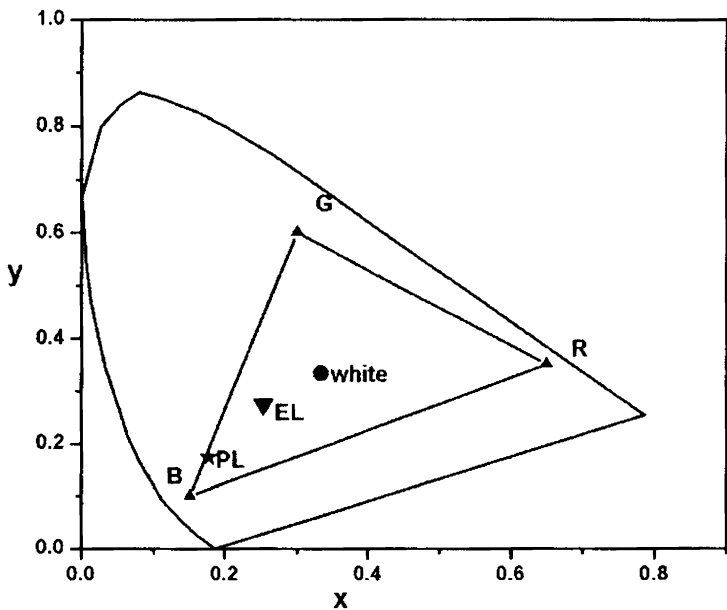


Figure 7.10. CIE chromaticity diagram showing the colour coordinates of PL and EL in SrS:Cu,F multilayer device

To observe electroluminescence the device was driven by a bipolar trapezoidal voltage of 1.2 kHz. The brightness- voltage characteristics of the device is shown in figure 7.11

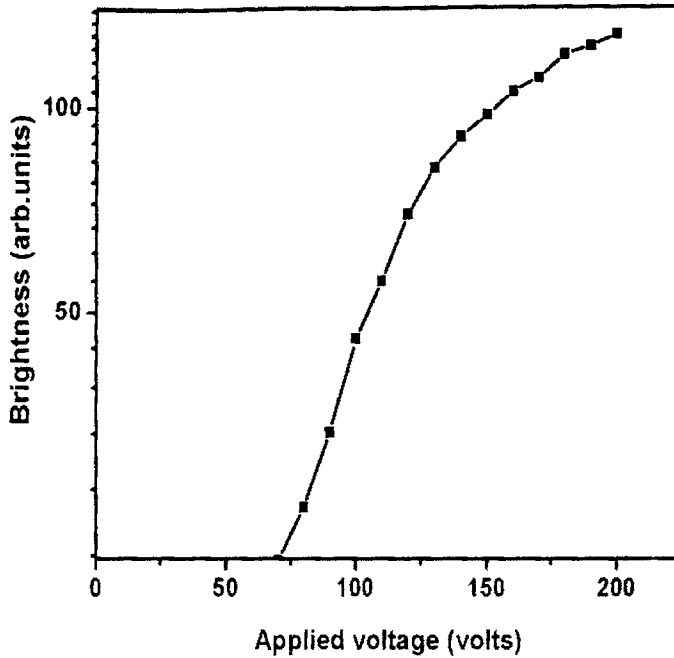


Figure 7.11. Brightness-Voltage characteristics of the SrS:Cu,F multilayer device.

## 7.5 Conclusion

We have demonstrated that high quality SrS:Cu,F films can be conveniently deposited on glass substrate without post-annealing and sulphur coevaporation. A device with ZnS buffer layer was fabricated by this method. PL emission of the device was blue whereas EL emission yellowish white in colour. This is due to the presence of an additional emission band at 535nm in EL spectrum. A possible model for the emission mechanism in the device is suggested.

## 7.6 References

1. S.S.Sun, E.Dickey, J.Kane and P. N.Yocom, Proc.17<sup>th</sup> Int.Display Research Conf., Morreale, J.,Ed.; Society for Information Display: Santa Ana, CA,1997.p301
2. S.Tanaka, S.Ohshio, J.Nishiura, H.Kawakami, H.Yoshiyama and H.Kobayashi; Appl.Phys.Lett. **52** (1988)2102
3. S.Okamoto and E.Nakazawa; Jpn J.Appl.Phys. **34** (1995)521
4. T.Morishita, H.Matsuyama, M.Matsui and M.Wakihara; Jpn.J. Appl.Phys. **38** (1999)6732
5. P.D.Keir, C.Maddix, B.A.Baukol and J.F.Wager; J.Appl.Phys. **86** (1999)6810
6. K.Neyts, Y.Meuret, G.Stuyven, D Visschere and S.Moehnke; J.Appl.Phys. **88** (2000)2906
7. D.Poleman,D.Wauters,R.L.Van Meirhaeghe,F.Cardon:Thin solid films,**350** (1999)67
8. W.Tong, Y.B.Xin, W.Park and C.J.Summers; Appl..Phys.Lett. **74** (1999) 1379
9. Y.B.Xin, W.Tong, W.Park, M.Chaichimansour and C.J.Summers: J.Appl.Phys.**85** (1999)3999
10. N.Yamashita, Jpn.J.Appl.Phys. **30** (1991)3335
11. Wei-Min Li, M.Ritala and M.Leskela; J.Appl.Phys.**86** (1999)5017
12. D.Wruck, R.Boyn, M.Wienecke, F. Hennerberger, U.Tropenz, B, Huttill, W.Bohne, B. Reinhold, H. -E. Mahnke, J.Appl.Phys, **91** (2002) 2847
13. N.Yamashita, K.Ebisumori, K.Nakamura, Jpn.J.Appl.Phys.**32** (1993) 3846
14. W.Lehmann, J.Electrochem. Soc.**117** (1970)1389

15. Y.Nakanishi, Natsume, Y.Fukuda, G.Shimaoka, H.Tatsuoka,  
H.Kuwabara and E.Nakazawa, J.Cryst.Growth **101** (1990)462
16. K.Ohmi, K.Yamabe, H.Fukada, T.Fujiwara, S.Tanaka and  
H.Kobayashi; Appl.Phys.Lett.**73** (1998)1889

# CHAPTER EIGHT

This chapter is divided into two parts: first part is an introduction to nanotechnology and the second part includes the work on Cu doped SrS nanophosphor.

## PART A

### Introduction to nanotechnologies and nanomaterials

#### 8.1 Introduction

*Nanoscience* is the study of phenomena and manipulation of materials at atomic, molecular and macromolecular scales, where properties differ significantly from those at a larger scale [1]. *Nanotechnologies* are the design, characterisation, production and application of structures, devices and systems by controlling shape and size at nanometer scale [1]. The plural was used since nanotechnology comprises a wide range of tools, techniques and applications. The size range that holds so much interest is typically from 100nm down to the atomic level (approximately 0.2 nm), because it is in this range (particularly at the lower end) that materials can have different or enhanced properties compared with the same materials at a larger size. The conceptual underpinnings of nanotechnologies were first laid out in 1959 by the physicist Richard Feynman, in his lecture ‘There’s plenty of room at the bottom’ (Feynman 1959). Feynman explored the possibility of manipulating material at the scale of individual atoms and molecules, imagining the whole

of the Encyclopedia Britannica written on the head of a pin and foreseeing the increasing ability to examine and control matter at the nanoscale.

Nanoparticles are larger than individual atoms and molecules but are smaller than bulk solid. There are two major phenomena that are responsible for these differences. First is the high dispersity of nanocrystalline systems. As the size of a crystal is reduced, the number of atoms at the surface of the crystal compared to the number of atoms in the crystal itself, increases. For example, a 4 nm diameter CdS nanoparticle has about 1500 atoms, of which about a third are on the surface. Properties, which are usually determined by the molecular structure of the bulk lattice, now become increasingly dominated by the defect structure of the surface.

The second phenomenon occurs noticeably only in metals and semiconductors. It is called size quantisation and arises because the size of a nanoparticle is comparable to the de Broglie wavelength of its charge carriers (*i.e.* electrons and holes). Due to the spatial confinement of the charge carriers, the edge of the valance and conduction bands split into discrete, quantized, electronic levels. These electronic levels are similar to those in atoms and molecules.

The spacing of the electronic levels and the bandgap increases with decreasing particle size. This is because the electron hole pairs are now much closer together and the Coulombic interaction between them can no longer be neglected giving an overall higher kinetic energy. This increase in bandgap can be observed experimentally by the blue-shift in the absorption spectrum or sometimes even visually by the colour of the samples. A larger bandgap means that more energy is required to excite an



electron from the valance band to the conduction band and hence light of a higher frequency and lower wavelength would be absorbed.

The increase in molar absorption coefficient shows that the oscillator strength also increases as particle size decreases. This is due to the strong overlapping of the wave functions of confined charge carriers. Experiments carried out in the past have found the absorption spectrum to be potential dependent, with decreasing wavelengths as applied potential decreases. This change is fully reversible before the threshold potential.

Due to the two unique phenomenon which occurs in nanoparticles, their properties (electrical, optical, chemical, mechanical, magnetic, *etc.*) can be selectively controlled by engineering the size, morphology, and composition of the particles. These new substances will have enhanced or entirely different properties from their parent materials. For instance, a relatively inert metal or metal oxide may become a highly effective catalyst when manufactured as nanoparticles; opaque particles may become transparent when composed of nanoparticles, or vice versa; conductors may become insulators, and insulators may change to conductors; nanophase materials may have many times the strength of the bulk material. Nanoparticles can comprise a range of different morphologies including nanotubes, nanowires, nanofibres, nanodots and a range of spherical or aggregated dendritic forms. These materials have seen application in a wide range of industries including electronics, pharmaceuticals, chemical-mechanical polishing, catalysis, and it is likely that the next few years will see a dramatic increase in the industrial generation and use of nanoparticles.

## 8.2 Exciton Bohr radius

An exciton is the term used to describe the electron-hole pair created when an electron leaves the valence band and enters the conduction band. Excitons have a natural physical separation between the electron and the hole that varies from substance to substance; this average distance is called the exciton Bohr radius. In a large semiconductor crystal, the exciton Bohr radius is small compared to the crystal, and the exciton is free to wander throughout the crystal. In a quantum dot, the exciton Bohr radius is on the order of the physical dimension of the dot or smaller, and the exciton is confined. This second set of conditions is called quantum confinement, which is synonymous with having discrete, rather than continuous energy levels.

## 8.3 Quantum confinement

In a nanostructured semiconductor, the quantum confinement occurs when electrons or holes in the material are trapped in one or more of the three dimensions within nanometer size regime. If the confinement occurs in one dimension only (say in the z-direction), it is assumed that the carriers like electrons and holes have free motion in other two x and y directions. This assumption is valid because size of the material in x and y directions is very large compared to the size in z-direction. Such a structure would be two dimensional (quantum well) and the carriers confined in one dimension will have two degrees of freedom. If the confinement is in two directions (say y and z), the electrons have free motion in x-direction. Such a structure would be one dimensional (quantum wire) and the carriers confined in two dimensions will have only one degree of freedom. Confinement in all the

three directions (i.e. x, y and z) will result in no free motion of electrons or holes in any direction. Such a structure would be 'zero dimensional' (quantum dot) and the carriers confined in all the three dimensions will have no degree of freedom. The inherent size dependent properties of these nanostructured materials will be result of two basic mechanisms: free energy variation due to free motion of carrier like electron and quantized energies due to quantum confinement. The total energy of electrons (or holes) will be the sum of allowed energies associated with the motion of these carriers along the confined direction and the kinetic energy due to free motion in the remaining unconfined directions.

In a bulk material the carriers can exist in nearly continuous band but in quantum dot structures due to the confinement of charges in all the three directions the carriers are restricted to a specific set of completely quantised energy states [2]. The effect of confinement on the resulting energy state of the system can be obtained by solving for the eigen energies of the Schrödinger wave equation, for the carriers in a confined space [2].

Different energy state equation can be obtained by depending upon the confinement regimes. Depending upon the ratio between the nano crystal radius,  $a$  and the bulk exciton radius  $a_B$ , three different confinement regimes can occur [3].

- (1) strong confinement regime
- (2) weak confinement regime
- (3) intermediate stage

The strong and weak states are determined by the degree of coupling between the electron and hole in the exciton.

### (1) Strong confinement regime:

When the quantum dot radius  $a_0$  is smaller than the excitonic bohr radius  $a_B$  it corresponds to the strong confinement state.

$$\text{ie; } a_0 \ll a_B$$

Which means that as the degree of confinement is increased in a smaller dot the exciton can no longer exist and therefore an electron and and hole can be treated as an independent particle [4]. And in this situation the coulomb effects are small compared with the quantization of the kinetic energy of the carriers (confinement energies). When these conditions are present the carriers are said to be strongly confined and the electron and hole wave functions are uncorrelated. Therefore the approach of solving the energy states in a strong confinement regime is similar to that in a weak confinement regime but the only exception is that in the case of strong confinement the electron and hole have independent Bessel function, and therefore the resulting energy shift expression can be written as

$$\nabla E_{nl} = \frac{\hbar^2 \alpha_{nl}^2}{2\mu^* a_0^2} + E_g$$

where  $\mu^*$  gives the effective reduced mass as  $\frac{1}{\mu^*} = \frac{1}{m_e^*} + \frac{1}{m_h^*}$  and

$\alpha_{nl}$  is the n zeroes of the spherical Bessel function of the order  $l$ .

## (2) Weak confinement regime :

When the quantum dot radius,  $a_0$  is few times greater than the excitonic bohr radius,  $a_B$  this corresponds to the weak confinement regime

$$\text{ie; } a_0 \gg a_B$$

which means that coulomb interaction energy is on the order of the electron and hole sublevel separations and it has to be taken into account. here the electron and hole motions are strongly correlated via coulomb interaction and the nano crystal energy spectra are determined by the quantization of the motion of the exciton center of mass [4]. Expression for energy quantization in a spherical 0D structure is

$$\nabla E_{nl} = \frac{\hbar^2 \alpha_{nl}^2}{2m^* a_0^2} + E_g - \frac{Ry^*}{n^2}$$

where  $m^*$  gives the effective exciton mass given by  $m^* = m_c^* + m_h^*$

this equation gives the shift in energy that occurs when a bulk solid exciton is confined in 3D in the range of 3-10 times the exciton bohr radius. ie; a blue shift in energy results as the size of the crystal decreases.

## (4) Intermediate stage

In the intermediate stage energy structures of nanocrystals are determined by a complex interplay between quantum confinement and the coulomb electron hole interaction. Due to the relatively large exciton bohr radius II-IV nanocrystals are convenient systems for the studies of the strong weak and

intermediate regimes [3]. the coulomb interaction scales with the nano radius as  $a^{-1}$  where as the confinement energies are proportional to  $a^{-2}$  therefore in the strong confinement regime the coulomb term in the Hamiltonian can be ignored which leads to a problem of independent quantization of electron and hole energies.

Effective mass approximation [EMA] has proven to be a powerful tool for describing energy structures in semiconductors, but it fails in the limit of very small nano crystals [3].

## **8.4 Nanophosphors**

Since nanomaterials possess unique chemical, physical, and mechanical properties, they can be used for a wide variety of applications. The resolution of a display device depends greatly on the size of the pixel which are made of phosphors. By synthesizing nanocrystalline phosphors the resolution of display devices can be greatly enhanced and the manufacturing cost can be significantly reduced. Nanocrystalline zinc selenide, Zinc sulphide, cadmium sulphide and lead telluride are candidates for improving the resolution of monitors. Also flat panel displays constructed out of nanomaterials possess much higher brightness and contrast than the conventional ones owing to their enhanced electrical and magnetic properties.

## PART B

# Synthesis and characterization of SrS:Cu nanophosphor

### 8.5 Abstract

**Abstract.** Strontium sulphide doped with copper has been regarded as one of the most promising inorganic material for the blue-green colour phosphor. A wet chemical precipitation method with post annealing is presented for the synthesis of copper doped SrS nanoparticles. XRD studies revealed the phase purity of SrS particles with rocksalt structure. TEM images showed the formation of nanoparticles with an average size of 7nm. Green photoluminescence emission (PL) at 535 nm was observed for an excitation wavelength of 356nm, intensity of which was fairly greater than that of coarser phosphor particles synthesized by solid state reaction. Low temperature PL showed a red shift with decreasing temperature which is due to aggregated copper centers. Luminescent decay at room temperature was found to be faster than the reported values of corresponding transition in thin film samples. Blue shift in the absorption edge was observed for the nanophosphor with respect to the bulk due to reduction in particle size.

### 8.6 Introduction

The development of nanophosphors is an area which has gained much attention during recent years. The structural, electronic and optical properties can be tuned by controlling the sizes of the nanoparticles [5-7].

Semiconductor nanostructured materials are currently considered to have technological applications in optoelectronic devices such as photodiodes, light emitting displays and electroluminescent devices [8-10]. Chemical synthesis of nanoparticles is a rapidly growing research area with a great potential to make technologically advanced and useful materials. By incorporating an impurity in a quantum confined structure, the dominant recombination route can be transferred from the surface states to the impurity states. If the impurity induced transition can be localized as in the case of transition metals or the rare earth elements, the radiative efficiency of the impurity induced emission increases significantly. Spectroscopic properties of defects in alkaline earth sulphides have been broadly studied by Pandey et al. [11]. Out of these, SrS:Cu bulk phosphors are one of the most studied luminescent materials [12,13]. SrS:Cu has been shown to have high potential as a blue thin film electroluminescent (TFEL) phosphor material. Preparation and characterization of zinc sulphide based nanophosphors and their application in electroluminescence has been reported recently [14-19]. The preparation of SrS:Ce nano particles by reverse micelle method by Kusakari et al. is the only report on luminescent alkaline earth nanophosphor [20]. In this work we report the synthesis of Cu doped SrS nanophosphor by a simple wet chemical method. The enhanced photoluminescence observed in this phosphor will improve the efficiency of electroluminescence.

## **8.7 Experimental**

20ml of 1M SrCl<sub>2</sub>.6H<sub>2</sub>O (99%, Loba Chemie) solution was mixed with 20ml of 0.2M CuCl<sub>2</sub>(99%, CDH) solution. 20ml of 0.125 mM polyvinyl pyrrolidone (PVP) was added to the above solution to control the reaction rate. The solution was stirred well and 20ml of 1M sodium sulphide (58%, CDH) solution was added dropwise with stirring. The filtered powder was then



placed in an oven at 55<sup>0</sup> C for two hours to dry. It was then fired in H<sub>2</sub>S atmosphere in a programmable furnace at 800<sup>0</sup> C for 1 hour resulting in the nanophosphor. SrS:Cu bulk was prepared by mixing CuCl<sub>2</sub> with SrS powder. For this, high purity chemicals SrS (99.9%, Cerac) and CuCl<sub>2</sub>.2H<sub>2</sub>O (99.99+%, Aldrich) were used. Required proportions of these highly pure precursors were accurately weighed and thoroughly mixed in ethanol medium. The dried powder was then fired for one hour at 900<sup>0</sup>C in H<sub>2</sub>S atmosphere. During firing at relatively high temperatures and in H<sub>2</sub>S atmosphere, the Cu<sup>2+</sup> ions are reduced by H<sub>2</sub>S into Cu<sup>+</sup> ions and diffused into the SrS lattice. The Cu<sup>+</sup> ions replace Sr<sup>2+</sup> ions at the octahedral site in the host lattice [21].

The crystal structure of the synthesized bulk phosphor and nanophosphor was studied using a Rigaku X-ray diffractometer with CuK $\alpha$  X-ray. The nanostructures of SrS:Cu nanoparticles were analyzed by high resolution transmission electron microscopy (JEM-3000F, JEOL). Inductively coupled plasma (ICP) (ICP-1000IV, Shimadzu) analysis was performed to determine the chemical composition of the samples. The photoluminescence (PL) and photoluminescence excitation (PLE) spectra of the samples were recorded using Spex-Fluoromax-3 Fluorimeter with 150W xenon lamp. The optical band gaps of the samples were estimated from the diffuse reflectance spectra recorded with Jasco-V-570 uv-vis-nir spectrophotometer. Low temperature PL emission spectra were recorded using ocean optics USB 2000 spectrometer, exciting the sample with He-Cd laser (325nm). The third harmonic of Nd-YAG laser (355nm) with pulse width 9ns was used as an excitation source for the decay measurement. The decay of 535nm emission was monitored with a photomultiplier tube having 5ns rise time and 100MHz storage oscilloscope.

## 8.8 Results and Discussion

### 8.8.1 SrS:Cu nano and bulk phosphor

Figure 8.1(a) shows the TEM images of the SrS:Cu nanoparticles synthesized by the chemical precipitation method. The nanoparticles exhibited nearly uniform size with spherical shape having a diameter of approximately 7 nm. Figure 8.1(b) shows selective area electron diffraction (SAED) patterns, confirming the crystalline SrS with rocksalt structure. The high resolution TEM shown in Figure 8.1(c), crystalline planes of nanoparticles clearly represent a 'd' spacing of  $3.007 \text{ \AA}$  demonstrating the growth of the particles in (200) plane.

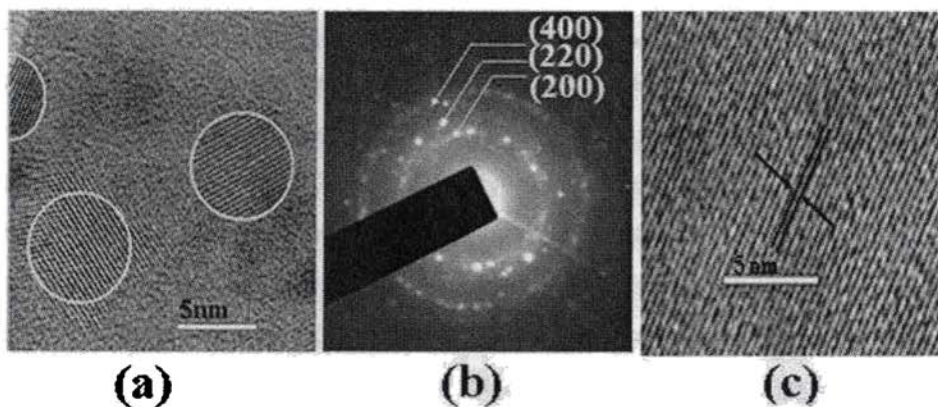


Figure 8.1. TEM images of SrS:Cu nanoparticles (a) shows particles with a diameter  $\sim 7 \text{ nm}$ , (b) SAED pattern showing diffraction rings corresponding to (200), (220) and (400) plane, (c) HRTEM corresponding to (200) plane with a d spacing of  $3.007 \text{ \AA}$

Eventhough the Cu concentration in the precursor solution was 0.2at.%, ICP analysis showed the Cu concentration as 2.68at.% in the SrS:Cu nanoparticles. To compare the emission characteristics of these nanophosphors with coarser particles, same dopant concentration (2.68at.%) was used in the preparation of SrS:Cu by solid state reaction. The structural,

photoluminescence and absorption characteristics of the bulk and nanophosphor were investigated.

XRD spectra of both samples matched the JCPDS file no.8-489 for cubic SrS without any traces of impurities as shown in figure 8.2. The diffraction lines of cubic phase of SrS have also been depicted for comparison. The average size of the particles in the samples were estimated using Scherrer formula considering the line broadening of the XRD patterns ( $D=0.9\lambda/\beta\cos\theta$  where  $\beta$  is the full width at half maximum of the diffraction peaks and  $\theta$  is the angle of diffraction). The size of SrS:Cu nanoparticles obtained from XRD pattern was 12nm and that of their coarser counter part was 55nm.

Figure 8.3 shows the optical absorption spectra of bulk and nanophosphor. Quantum confinement effect is evident from these spectra. Two absorption peaks are observed in both cases in which the peak below 300nm corresponds to the absorption in the SrS host lattice and that around 400nm corresponds to the absorption in  $\text{Cu}^+$  centers. The absorption maximum in the host lattice for the nanophosphor particles is at 253nm (4.9eV), and that of the phosphor particles prepared by solid state reaction is at 266nm (4.6eV). These peaks show a blue shift with respect to the band gap energy of the bulk SrS (4.2eV).

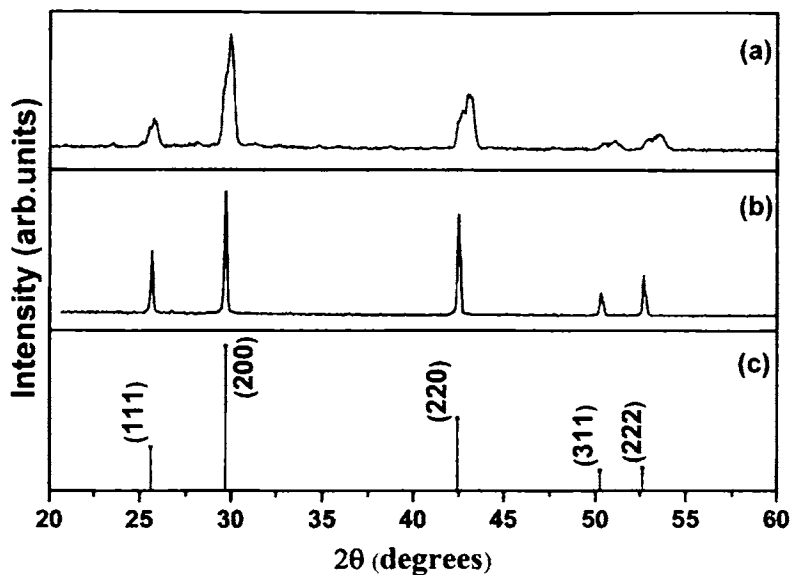


Figure 8.2. XRD patterns of (a) SrS:Cu nanoparticles prepared by chemical method (b). SrS:Cu phosphor prepared by solid state reaction and (c). plot of JCPDS data of pure SrS

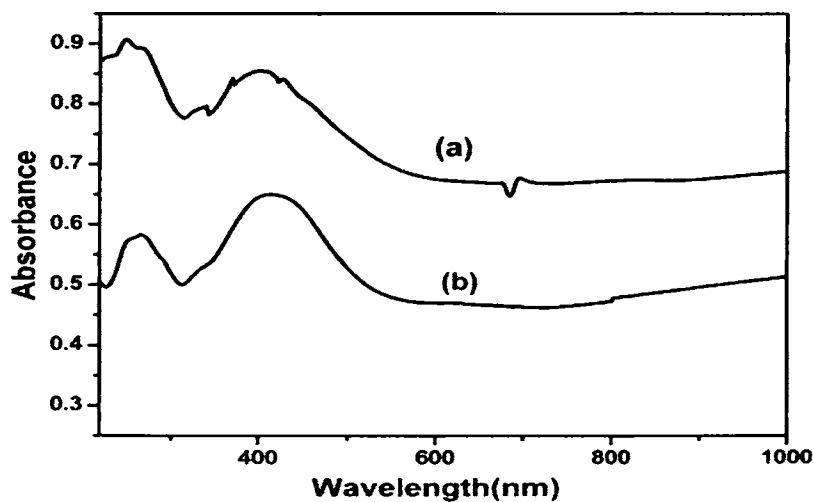


Figure 8.3. The optical absorption spectra of (a). SrS:Cu nanoparticles and (b). SrS:Cu phosphor prepared by solid state reaction

Photoluminescence emission spectra of both samples at an excitation wavelength of 356nm are shown in figure 8.4. Strong green emission at 531nm was observed in both cases with the integral intensity of SrS:Cu nanoparticles being 1.7 times of their coarser counterparts. Also the spectral bandwidth of  $\text{Cu}^+$  green emission in nanophosphor is much wider than its value in the coarser sample. This increased bandwidth was reflected in the improved external efficiency. The emission process has been attributed to the transition between perturbed energy levels of  $\text{Cu}^+$  ion ( ${}^3\text{E}_g$  to  ${}^1\text{A}_{1g}$ ) in octahedral crystal field [22]. The emission wavelength of the  $\text{Cu}^+$  luminescence in SrS:Cu depends on the Cu concentration, co-dopants and temperature [23]. Blue luminescence in SrS:Cu is produced by  $[\text{Cu}^+_{\text{Sr}}]^-$  centers with coordination number 6. Such a situation arises when a  $\text{Cu}^+$  ion occupies an interstitial site adjacent to a  $\text{Cu}^+$  ion in the lattice site there by causing charge compensation without producing sulphur vacancies. The coordination number refers to the number of  $\text{S}^{2-}$  ions closest to the  $\text{Cu}^+$  ion. Coordination number 5 implies that there are sulfur vacancies near the  $[\text{Cu}^+_{\text{Sr}}]^-$  center, which lowers the symmetry of  $\text{Cu}^+$  center, resulting in green luminescence. In other words green luminescence is produced by Cu on Sr site off-center position.

Photoluminescence excitation spectra (PLE) of the two samples monitored at an emission wavelength of 535nm are shown in figure 8.5. The excitation wavelength is at 356nm in both cases which is due to the transition in the split levels of  $\text{Cu}^+$  ion in octahedral crystal field. Intensity and line width of SrS:Cu nanocrystals is fairly greater than SrS:Cu phosphor prepared by solid state reaction.

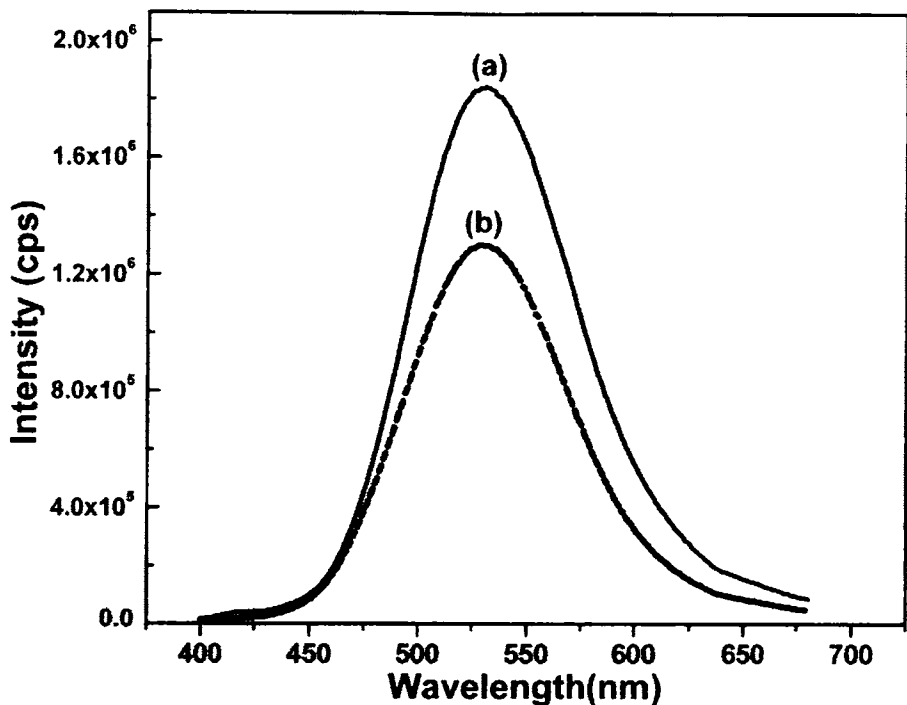


Figure 8.4. PL spectra of (a) SrS:Cu nanocrystals and (b) SrS:Cu phosphor synthesized by solid state reaction with  $\lambda_{ex}=356\text{nm}$

The impurity capture rate for a fixed number of impurities in a doped nanocrystal varies as  $1/R^3$ ,  $R$  being the radius of the particle [24]. Thus as the size of the quantum dot decreases, the impurity related capture rate increases sharply resulting in enhanced luminescence. This increase is a consequence of the enhanced overlap of the s-p host electron-wave function with the d-f electron wave function of the impurity [25]. Thus reduction in crystal size prevents both radiative and nonradiative relaxation through unwanted competitive channels such as surface states and other impurities.

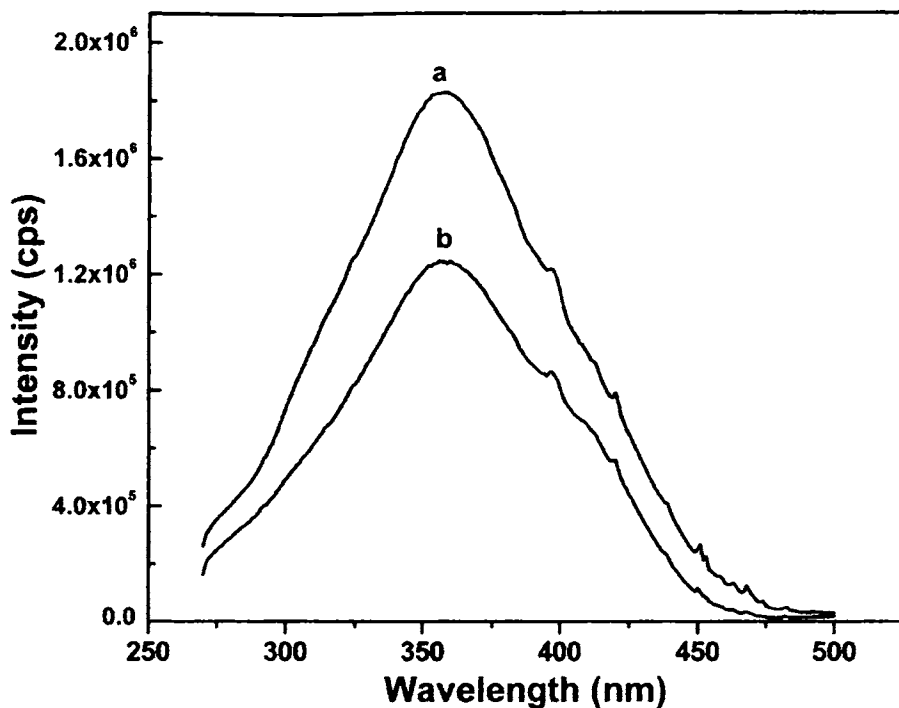


Figure 8.5. PLE spectra of (a) SrS:Cu nanoparticles and (b) SrS:Cu phosphor prepared by solid state reaction with  $\lambda_{\text{exc}}=535\text{nm}$

Figure 8.6 shows the low temperature PL spectra of green emitting SrS: Cu nanophosphor for a temperature scan of 12K to 300K. A small red shift of about 4nm was observed on decreasing the temperature. Green luminescence was observed in SrS: Cu bulk phosphor at higher Cu concentrations and lower temperatures [26, 27] due to the formation of off centered  $\text{Cu}^+$  centers.

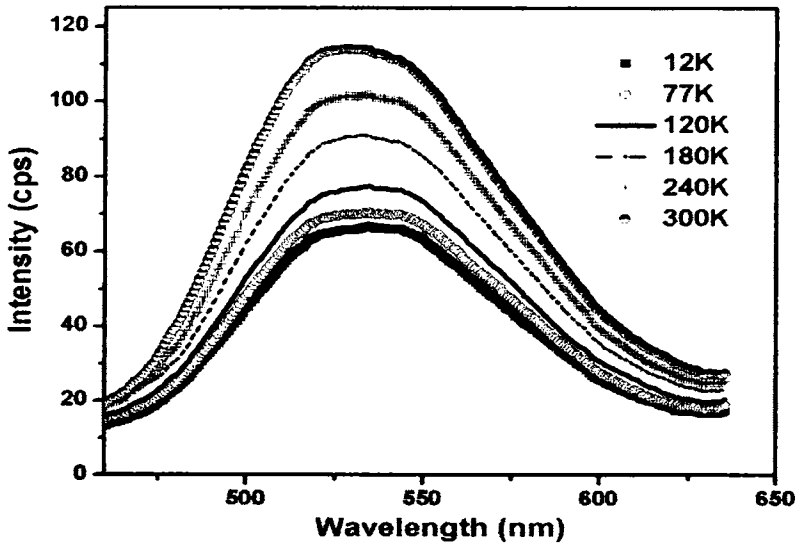


Figure 8.6. Temperature dependence of the PL spectra of SrS:Cu nanophosphor ( $\lambda_{\text{ex}}=325\text{nm}$ )

Further shift to longer wavelengths results from the formation of aggregated  $\text{Cu}^+$  centers [12].

Room temperature decay spectrum of SrS:Cu nanophosphor at 531nm when excited at 355nm is shown in figure 8.7. Two different decays are present with decay times 23ns and 1.1 $\mu\text{s}$  which are appreciably smaller than that reported for thin film [27]



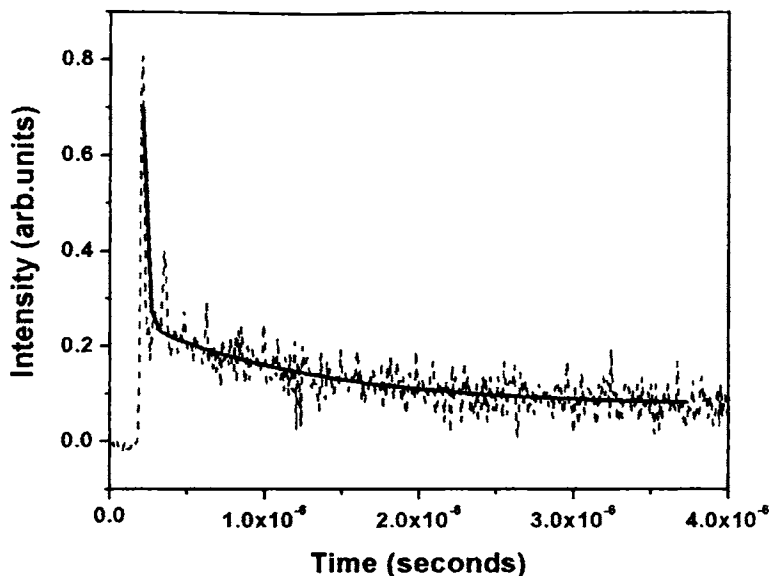


Figure 8.7. The decay time of the light emission from nanocrystalline SrS:Cu. Solid line is the fitted curve.

### 8.8.2 Effect of firing temperature on the properties of SrS:Cu nanophosphor

XRD patterns of SrS:Cu nanoparticles for different firing temperatures is shown in figure 8.8. Eventhough diffraction peaks in different planes were obtained for the samples fired at 750<sup>0</sup>C some impurity peaks were also observed which disappears for the samples fired at 800<sup>0</sup> C. Maximum broadening of the lines was observed for the sample fired at 800<sup>0</sup> C indicating least size for the particles.

Figure 8.9 shows the absorbance spectrum of the SrS:Cu nanoparticles. Blue shift in the absorption edge is observed with reduction in particle size.

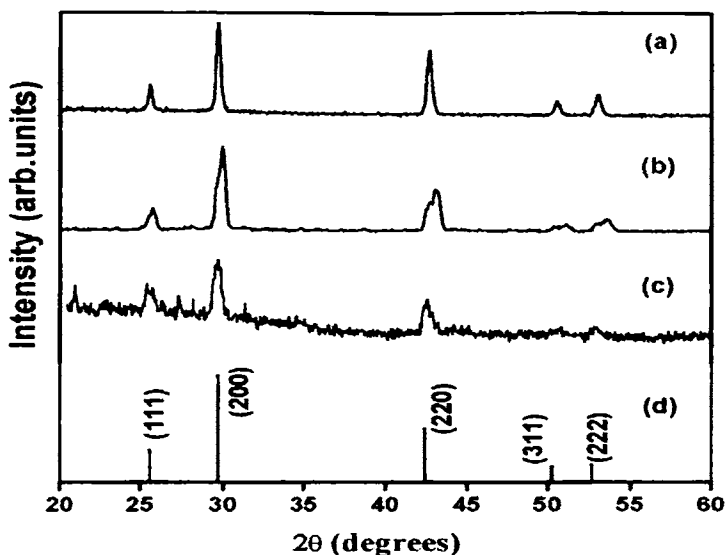


Figure 8.8. XRD patterns of SrS:Cu nanoparticles obtained for different firing temperatures, (a). 850<sup>0</sup> C (22nm), (b). 800<sup>0</sup> C (12nm), (c) 750<sup>0</sup> C (21nm) and (d). JCPDS data of SrS.

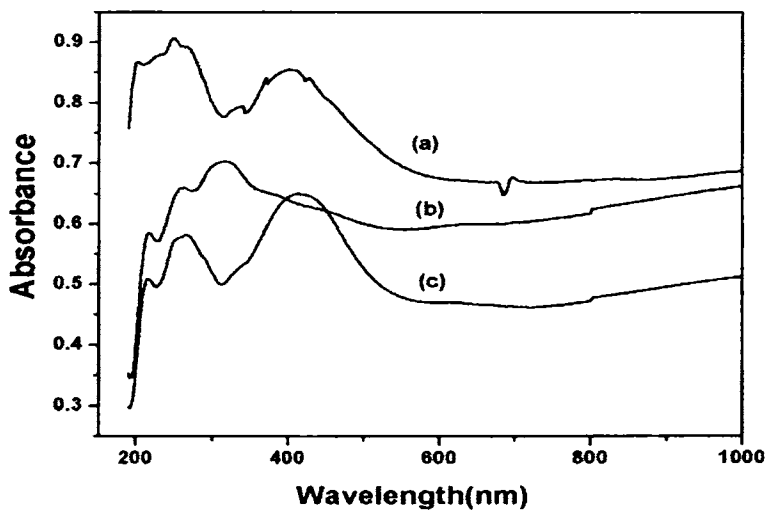


Figure 8.9. Absorbance spectrum of SrS:Cu nanoparticles obtained for different firing temperatures (a). 800<sup>0</sup> C , (b). 750<sup>0</sup> C (c). 850<sup>0</sup> C

Photoluminescence spectra of all the samples show a green emission at 535nm at an excitation wavelength of 356nm and the intensity is found to be a maximum for the sample fired at 800<sup>0</sup>C (figure 8.10). This is due to the fact that reduction in crystal size prevents both radiative and nonradiative relaxation through unwanted competitive channels such as surface states and other impurities. The intensity of the sample fired at 850<sup>0</sup>C is lower than that fired at 800<sup>0</sup>C due to an increase in crystal size. But for the sample fired at 750<sup>0</sup>C the emission intensity is not in agreement with size effects. This may be due to the lack of crystallinity which is clear from the XRD.

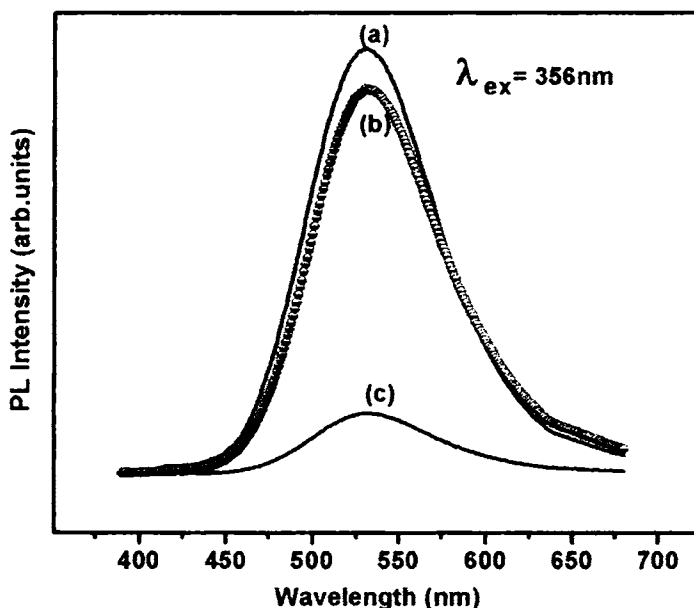


Figure 8.10. PL spectrum of SrS:Cu nanoparticles prepared by wet chemical method for different firing temperatures.(a). 800<sup>0</sup>C, (b). 850<sup>0</sup>C, (c). 750<sup>0</sup>C

The variation in intensity and linewidth of the photoluminescence excitation spectra of the samples are similar to that of PL spectra as shown in figure 8.11. The photoluminescence excitation is found to be at 356nm for an emission wavelength of 535nm.

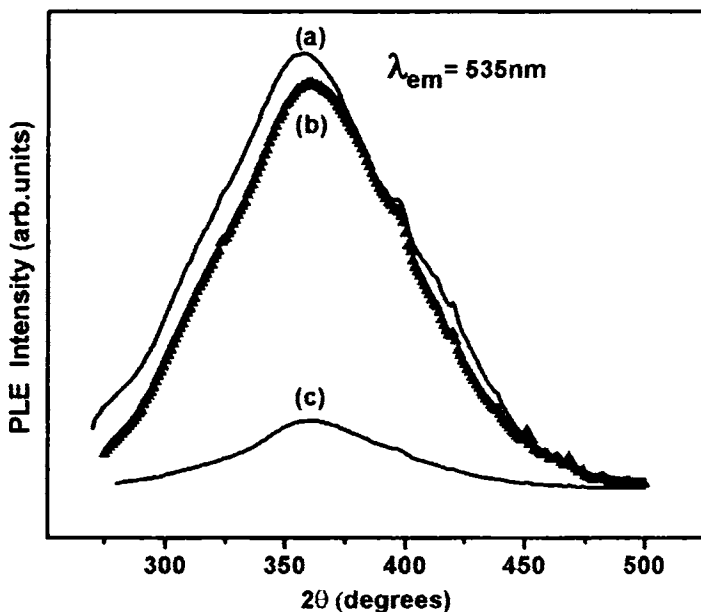


Figure 8.11. PLE spectrum of SrS:Cu nanoparticles prepared by wet chemical method for different firing temperatures. (a).800<sup>o</sup> C, (b).850<sup>o</sup> C, (c).750<sup>o</sup> C

Figure 8.12 shows the TGA result for the as-synthesised SrS:Cu nanoparticles. The weight loss observed in region 'a' is due to evaporation of residual water adsorbed to the surface of the particles. The PVP bonding at the surface desorbs in region 'b'. Region c shows the desorption of some other impurities which are not identified which are present in the sample fired at 700<sup>o</sup>C.

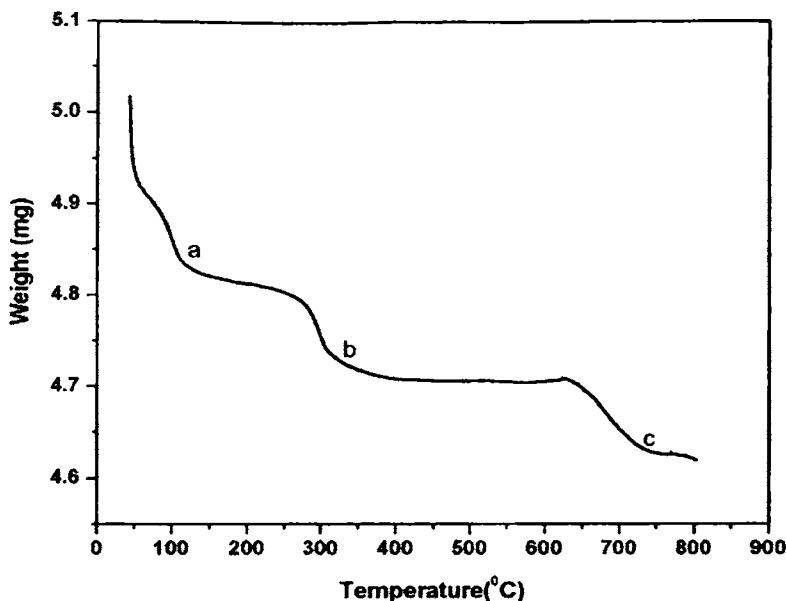


Figure 8.12 TGA curve of SrS:Cu nanoparticles at a heating rate of 20<sup>o</sup>C/min under a nitrogen flow

## 8.9 Conclusion

Copper doped strontium sulphide nanoparticles were prepared by wet chemical precipitation method followed by annealing at different temperatures. From the XRD patterns, the sample fired at 800<sup>o</sup>C was found to have least size and from the analysis by TEM, the size of the sample was found to be ~7 nm. Variation in band gap, intensity and line width of photoluminescence emission and excitation and decay time of the samples were found to be in agreement with size effects. The emission at 535nm originates from off- centered copper sites and copper pairs which red shifted at low temperature due to the formation of more aggregated centers. Since the spectral energy distribution in SrS: Cu system is known to be independent of excitation source, the results can be reproduced in the function of electroluminescent devices.

## 8.10 References

1. The Royal Society/ Royal Academy of Engineering report (2004)
2. S. V. Gaponenko, Optical properties of semiconductor nano crystals, Cambridge Studies in Modern Optics
3. K.E.Gonsalves, S P Rangarajan and J Wang ,edited by Harisingh Nalwa, Nanostructured Materials and Nanotechnology, Academic Press (2002)
4. Tracie J. Bukowsk and Joseph H. Simmons, Critical Review in Solid state and Materials Science, **27** (2002) 119
5. R.W.Cahn.Nature **348** (1990) 389
6. R.Dagani,Chem.Eng.News.**72** (1992) 18
7. H.Gleiter,Nanostruct.Mater.**6** (1995) 3
8. J.P.Kuczynski.J.Am.Chem.Soc.**108** (1986) 2513
9. Y.Wans and N.Herron.J.Phys.Chem.**95** (1991) 525
10. K.Manzoor,S.R.Vadera,N.Kumar and T R N Kutty, Appl.Phy.Lett. **84** (2004) 284
11. R.Pandey and S.Sivaraman, J.Phys.Chem.Solids. **52** (1991) 211
12. N Yamashita,K Ebisumori and KNakamura.Jpn. J.Appl.Phys. **32** (1993) 3846
13. B B Laud, V. W Kulkarni, Physica Scripta.**22** (1980) 415
14. S.J.Xu, S.J.Chua, B.Liu, L̄.M.Gan, C.H.chew and G.O.Xu, Appl.Phys. Lett.**73** (1998) 478
15. K.Manzoor, S.R.Vadera, N.Kumar and T.R.N.Kutty, Mater. Chem. Phys.**82** (2003) 718
16. Denzler D, Olschewski M and Sattler K, J.Appl.Phys. **84** (1998) 2841

17. A.A.Khosrav, M.Kundu, L.Jatwa, S.K.Deshpande, V.A.Bhgawat, M.Shastri, and S.K.Kulkarni, *Appl.Phys.Lett.* **67** (1995) 2705
18. M.Wang, L.Sun, X.Fu, C.Liao and C.Yan *Solid State Commun.***115** (2000) 493
19. D.Son,D.R.Jung, J.Kim, T.Moon, C.Kim and B.Park, *Appl.Phys.Lett.* **90** (2007)101910
20. Y. Kusakari, S. Ishizaki and M. Kobayashi, *Mater. Res. Soc.Symp. Proc.***829** (2005) B10.2
21. Y.B.Xin,W.Tong,W.Park, M.Chaichimansour, C.J.Summers, *J. Appl. Phys.***85** (1999) 3999
22. J. Ihanus, M. Ritala, M. Leskela, W. Park, A.E.kaloyeros, W Harris, K.W.Barth, A. W.Topol, *J.Appl.Phys.*, **94** (2003) 3862
23. N.Yamashita, *Jpn.J.Appl.Phys.*,**30** (1991) 3335
24. R.N.Bhargava, D.Gallagher and T.Welker, *J.Lumin.* **60** (1994)275
25. R.N.Bhargava, *J.Lumin.***70** (1996) 85
26. D.Wruck, R.Boyn, M.Wienecke, F.Henneberger, U.Troppenz, B.Huttl, W. Bohne,B.Reinhold and H.E.Mahnke *J.Appl.Phys.***91** (2002) 2847
27. W.M.Li, M.Ritala, M.Leskela, L.Niinisto, E.Soininen, S S Sun, W.Tong and C.J Summers *J.Appl.Phys.***86** (1999) 5017

# CHAPTER NINE

## Summary

### 9.1 Summary

Thin film electroluminescence possesses excellent visual characteristics in comparison with other flat panel display technologies. Volume production of monochrome EL display panels started in 1983 and they have gained a wide market place acceptance [1]. Now they are available from Sharp, Planar, Luxell etc. Research efforts are going on to improve the luminance, enhance resolution, lower the power consumption and reduce the cost.

Simplification drive circuit can bring down cost. Improvements in device structures and deposition conditions are also important. Lower temperature processes with good crystallinity and continuous processes without breaking vacuum are necessary for better thin film qualities. Since an EL display is a capacitive device, a large current is necessary in driving. Therefore power consumption reduction in the electrodes and drive circuit system is effective to low- power driving. Employment of resonating circuits using inductances has made it possible to realize low power consumption display panels [2].

The first commercial multicolour thin film EL display was based on ZnS:Mn phosphor which was a patterned colour filter device structure [3]. Multilayered phosphor structures have been proposed to obtain higher luminance [4,5].



This thesis has focused on the synthesis and analysis of some important phosphors (nano, bulk and thin film) for display applications. ACTFEL device with SrS:Cu as active layer was also fabricated.

Three bulk phosphors: SrS:Cu,Cl; SrS:Dy,Cl; and SrS:Dy,Cu,Cl were synthesized and their structural, optical and electrical properties were investigated. Special emphasis was given to, the analysis of the role of defects and charge compensating centers, on the structural changes of the host and hence the luminance. A new model describing the sensitizing behaviour of Cu in SrS:Dy,Cu,Cl two component phosphor was introduced. It was also found that addition of NH<sub>4</sub>Cl as flux in SrS:Cu caused tremendous improvement in the structural and luminescence properties.

A novel technique for ACTFEL phosphor deposition at low temperature was introduced. Polycrystalline films of SrS:Cu,F were synthesized at low temperature by concomitant evaporation of host and dopant by electron beam evaporation and thermal evaporation methods.

Copper doped strontium sulphide nanophosphor was synthesized for the first time. Improvement in the luminescence properties was observed in the nanophosphor with respect to its bulk counterpart.

## References

1. M.Takeda, Y.Kanatani, H.Kishishita and H.Uede, Proc.SPIE 386, Advances in Display TechnologyIII (1983) 34
2. C.N.King, 1994 SID Seminar Lecture Notes, Vol1(1994) M-9
3. J.Haaranen, R.Tornqvist, J.Koponen, T.Pitkanen, M.Surma-aho, W.Barrow and C.Laakso, Digest of 1992 SID International Symposium (1992) 348
4. R.H.Mauch, K.O.Velthaus, B.Huttl and H.W.Schock, Digest of 1993 SID International Symposium (1993) 769
5. S.Tanaka, K.Ohmi, K.Fujimoto, H.Kobayashi, T.Nire, A.Matsuno and A.Miyakoshi, Eurodisplay' 93 (1993) 237